ANTENNA-COUPLED INFRARED AND MILLIMETER-WAVE DETECTORS: FABRICATION, MEASUREMENT AND OPTIMIZATION

by

CHARLES F. MIDDLETON IV
B.S. Brigham Young University, 2001
M.S. University of Central Florida, 2002

A dissertation submitted in partial fulfillment of the requirements
for the degree of Doctor of Philosophy
in the College of Optics and Photonics
at the University of Central Florida
Orlando, Florida

Summer Term
2006

Major Professor: Glenn D. Boreman

ABSTRACT

Antenna-coupled detectors provide uncooled, cost-effective solutions for infrared and millimeter-wave imaging. This work describes the design, fabrication, measurement, and optimization of several types of antenna-coupled detectors for LWIR (8 - 12 μm) and 94 GHz radiation. Two types of millimeter-wave antenna-coupled detectors were fabricated and tested: a slot antenna coupled to a bolometer, and a patch antenna coupled to a SiC Schottky diode. Electromagnetic modeling of the antennas helped guide the design of antennas with better impedance matching to the detectors. Schottky diodes are discussed as detectors for millimeter-wave and infrared radiation, with the goal of increasing the cutoff frequency to allow infrared detection. The magnitude of response of antenna-coupled bolometric detectors to infrared radiation is affected by the thermal-conduction properties of the sensor structure. Two fabrication processes were developed to improve the thermal isolation of the antenna-coupled bolometer from its substrate. The first process creates a membrane beneath the device. Measured results show a factor of 100 increase in responsivity over an identical device without a membrane. The second process thermally isolates the device from its substrate by suspending the metallic

structure in air. Several factors for optimization of infrared antenna-coupled detectors are investigated. The complex dielectric function of the metal from which the antenna is constructed can affect the performance of the device. The use of a ground plane and dielectric standoff layer beneath the antenna can increase the sensor responsivity. Dielectric material properties and thicknesses are considered, and incorporated in device simulations. Finally, a potential fabrication process is presented for via connections from the antenna-coupled detector through a ground plane to bond pads to mitigate the effect of bias lines on antenna behavior.

For Kimberly and Ruby

ACKNOWLEDGMENTS

None of us got where we are solely by pulling ourselves up by our bootstraps.

-Thurgood Marshall

The universe is wider than our views of it.

- Henry David Thoreau

I wish to thank Dr. Glenn Boreman for providing an atmosphere in which this research could be conducted. His support and guidance were unparagoned, and one couldn't ask for a better advisor. I am also indebted to my advisory committee: Dr. Brian Lail, Dr. Aravinda Kar, and Dr. James Harvey for their great advice and wisdom.

One of the privileges of undertaking this work has been the close association with members of the Infrared Systems Lab, both past and present. Their advice, skill and insight have been extraordinary, and I am grateful for their friendship. I especially thank Javier Gonzalez, whose dissertation work I continued; Chris

Middlebrook, who offered invaluable discussion and perspective; and Guy Zummo, who has helped me and the rest of the lab overcome countless technical obstacles (if he can't fix it, it ain't broke).

My family has also been a great source of support and encouragement. My cousin, Amy Middleton, and my sister, Becky Middleton, provided sage advice on font selection. My parents deserve my deep gratitude for all they have taught me. Most of all I thank my wife, Kimberly, for her love, faith, and cheerfulness.

TABLE OF CONTENTS

LIST OF FIGURES

LIST OF TABLES

LIST OF ACRONYMS / ABBREVIATIONS

Al	aluminum
Al_2O_3	aluminum oxide (alumina)
Ar	argon
Au	gold
BCB	benzocyclobutene (Cyclotene)
Bi	bismuth
BOE	buffered oxide etch
$C_6H_8O_7$	citric acid
CF_4	carbon tetrafluoride
CHF_3	trifluoromethane
Cr	chromium
DC	direct current
DI water	de-ionized water
He	helium
E-beam	electron beam
H_2O	water
H_2O_2	hydrogen peroxide

HCl	hydrochloric acid
HF	hydrofluoric acid
HFSS	high frequency simulation software
HMDS	hexamethyldisilazane
HP_3O_4	phosphoric acid
InGaAs	indium gallium arsenide
InP	indium phosphide
IPA	isopropyl alcohol (isopropanol)
IR	infrared
LPCVD	low-pressure chemical vapor deposition
LWIR	long wave infrared
MMW	millimeter wave
MSE	mean squared error
N_2O	nitrous oxide
NEP	noise-equivalent power
NETD	noise-equivalent temperature difference
O_2	oxygen
PECVD	plasma-enhanced chemical vapor deposition
PMMA	polymethyl methacrylate

PMGI	polymethylglutarimide
RF	radio frequency
RIE	reactive-ion etching
rpm	revolutions per minute
sccm	standard cubic centimeters per minute
SEM	scanning electron microscope
SF_4	sulfur tetrafluoride
Si	silicon
Si_3N_4	silicon nitride
SiO	silicon monoxide
SiO_2	silicon dioxide
SNR	signal-to-noise ratio
TEAH	tetraethylammonium hydroxide
TMAH	tetramethylammonium hydroxide
VSWR	voltage standing wave ratio
W	tungsten
ZrO_2	zirconium dioxide (zirconia)

CHAPTER 1

INTRODUCTION

1.1 Bolometers for Uncooled Detection

A bolometer is a thermal detection device that takes advantage of the temperature dependence of a material's electrical resistance [1]. A constant bias current is sent through the bolometer so that when it sees a change in temperature, the corresponding change in resistance is observed as a voltage signal. Bolometers have been used for thermal detection since their invention in 1881 [2].

Since a bolometer's signal depends on a change in temperature, sensitivity is enhanced when the device is cryogenically cooled [3]. However, this adds to the cost and weight of the device and limits its use in many applications. Uncooled bolometers are now commonly used in focal plane arrays, as advances in materials and thermal isolation techniques have increased the sensitivity of these devices [4]. The bolometers used in this dissertation are uncooled, lithographically structured pieces of metal.

1.2 Antennas for Infrared and Millimeter-wave Detection

By decreasing the thermal mass of the bolometer, one can increase the response speed of the device. But a smaller bolometer has a smaller capacity to collect radiation, and the device sensitivity decreases. The capture area of the bolometer can be increased by coupling it to an antenna. The printed-circuit antennas used in this work allow the bolometer size to be on the order of 500 nm square, with thermal time constants of several MHz [5]. Coupling an antenna to the bolometer allows one to take advantage of the spectral, polarization, and array properties of antennas as well [6].

The coupling of lithographic antennas to infrared and millimeter-wave detectors has been investigated for use with various types of detectors [7-10]. The antennas used in this dissertation were adapted from RF designs and chosen based on the desired performance [11]. For infrared detectors, the square spiral antenna was used exclusively.

1.3 Device Characterization and Figures of Merit

Several figures of merit have been used to compare the performance of various infrared and millimeter-wave detectors. With most devices, a voltage signal and noise figure can be directly measured, as well as the incident power level. From these three quantities, one can calculate the relevant figure of merit. The important figures of merit are responsivity, NEP, and D* for infrared detectors; and NEP and NETD for millimeter-wave detectors.

Voltage responsivity is found by dividing the received signal by the incident power, with units of Volts per Watt. To calculate responsivity, one must know the effective area of the detector. In most cases, the detector is much smaller than a wavelength, and a deconvolution algorithm must be applied to determine the effective area [12]. While this shows the sensitivity of a detector to incident radiation (higher responsivity equals better detector), it neglects the noise of the device. The signal-to-noise ratio (SNR) includes the device noise but neglects the incident power. Noise-equivalent power (NEP) is therefore a more useful metric

for a detector. This is a measure of the incident power required to obtain unity SNR [13]. NEP is obtained from measured quantities as follows:

$$NEP = \frac{\phi_{device}}{v_{signal} / v_{noise}} \tag{1.1}$$

Here ϕ_{device} is the power incident on the detector, v_{signal} is the measured voltage signal, and v_{noise} is the measured noise figure. Since NEP is a quantity that is smaller for a better detector, which is unusual for a performance index, detectivity was proposed as a figure of merit [14], where

$$D = \frac{1}{NEP} \tag{1.2}$$

The area of the device and the measurement system bandwidth are not included in NEP or detectivity, so to give a more realistic comparison between different sizes of detector and different measurement systems, normalized detectivity (D*) is used. It has units of cm √Hz / Watt and is given by:

$$D^* = \frac{\sqrt{A_{device}\,\Delta f}}{NEP} \tag{1.3}$$

For millimeter-wave detectors, NEP is commonly used to compare sensitivity. Another important figure of merit is NETD, or noise-equivalent temperature difference. This represents the difference in relative temperature between two objects that results in unity SNR, and its units are either Kelvin or degrees Celsius. NETD is obtained from NEP for millimeter-wave devices by

$$NETD = \frac{NEP\sqrt{\Delta f}}{k\,B} \tag{1.4}$$

Here k is Boltzmann's constant and B is the bandwidth of the antenna. For infrared detectors, NETD can also be obtained from blackbody measurements. In this case, the blackbody temperature is used rather than the incident radiation power:

$$NETD = \frac{T}{v_{signal} \big/ v_{noise}} \tag{1.5}$$

CHAPTER 2

FABRICATION TECHNIQUES

2.1 Electron-Beam Lithography

2.1.1 Overview of Capabilities

All devices in this dissertation were fabricated using either electron beam or optical lithography. Given the dimensions of most of the devices, the limitations of the available optical lithography equipment, and the need to frequently change mask layouts and device dimensions, most of the fabrication has involved e-beam rather than optical lithography. E-beam lithography was done initially with a converted JEOL SEM using a dual-interferometer laser stage and RAITH software, with a 30 kV accelerating voltage. In 2004 a Leica EBPG 5000+ system was purchased, which can operate at 20, 50, and 100 kV. Most of our processes have been designed to work at 50 kV.

Processes have been developed with the goal of fabricating devices with critical dimensions of no less than 300 nm. Most processes involve a bi-layer of resist for

a lift-off process following metal deposition. In this section I explain the necessary steps to prepare a design for e-beam writing. I then give detailed process parameters for sample preparation, exposure, development, and resist removal for PMMA, PMMA/copolymer bi-layers, ZEP 520A, ZEP 520A/PMGI bi-layers, and ZEP 520A/PMMA bi-layers. I also give process details for a spin-on dielectric, BCB. For more information on the physics of both e-beam and optical lithography, see [15-17].

2.1.2 Pattern File Preparation for Electron-Beam Lithography

This discussion applies to files for use with the Leica EBPG 5000+ system. Figure 2-1 shows a flow chart for pattern file preparation. Device design patterns may be prepared in a variety of formats, but they must be converted to GDSII format, the long-standing de facto standard for integrated circuit layout data. Several software packages can be used to draw pattern files: CleWin, AutoCAD, and L-Edit are a few examples. I prefer to use L-Edit, a mask layout editor by Tanner

Research, Inc. With this software I am able to draw pattern files with elaborate layer and hierarchical structures and then export the files into GDSII format. When creating a pattern file, separate layer assignments are used for patterns that will be exposed using a different beam current or resolution, or for patterns that will be exposed during different process steps.

If alignment is necessary for any process step, appropriate alignment markers must be included in the pattern file from the beginning. A standard alignment procedure requires four square-shaped markers with known size and spacing, used in what is known as a "keystone" alignment. It is best to decide how many alignment steps will be required, and then add the corresponding number of sets of alignment markers to the layer that will be exposed first. When the e-beam uses an alignment marker, it exposes the resist around that marker; if a successive step includes metal deposition on the exposed areas of the wafer, the exposed marker will no longer be useable. So each alignment step requires its own set of alignment markers. These are typically 20 x 20 μm squares of gold. Other marker dimensions and materials are possible, but there may be difficulties associated with them.

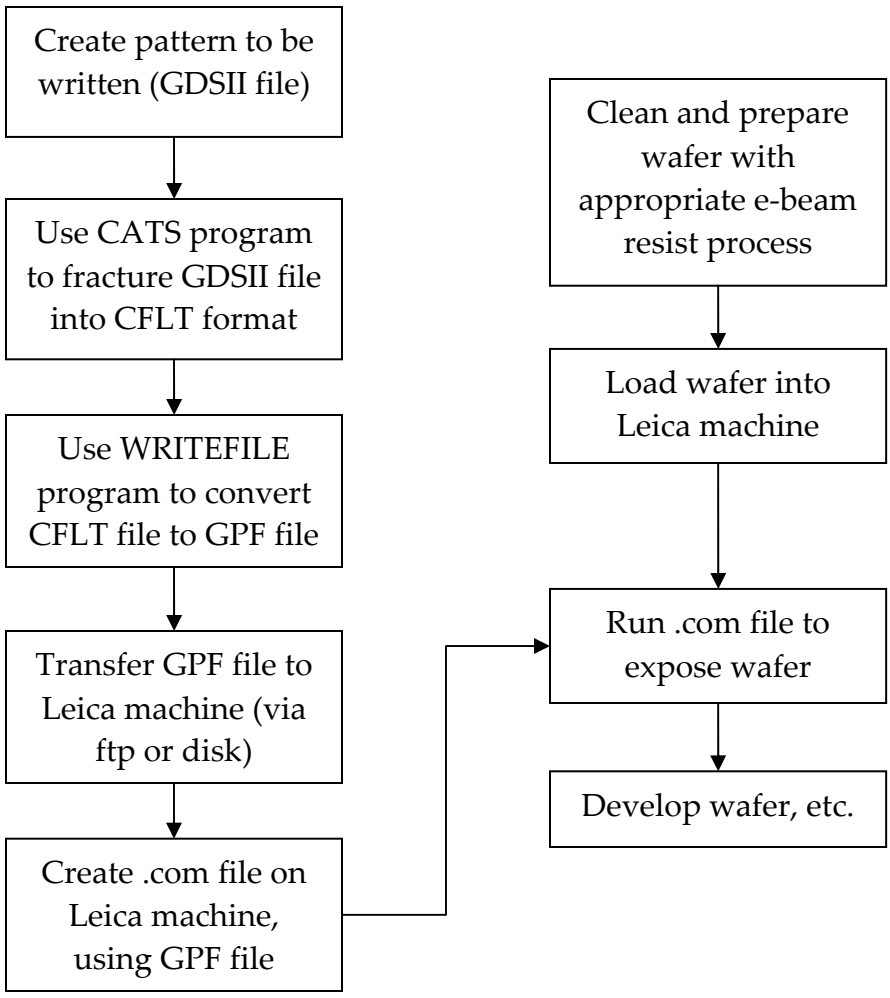

Figure 2-1: Flow chart for e-beam process file preparation, wafer preparation, and exposure

For example, negative alignment markers can be made out of gold and used effectively in successive steps. But positive markers made of Ti or Ni will not be visible to the e-beam. Other metals might be possible, especially those with higher atomic numbers (Ag or Pt, for example), depending on the contrast range of the e-beam system. Alignment markers should be placed at least 100 μm away from any other feature in the pattern, since the alignment process exposes the area around the marker. There is no constraint on field size, i.e. the alignment markers are not required to fit inside one write field.

For a successful alignment job, one must specify three positions: the center of the pattern relative to the center of the lower left alignment marker; the distance from the center of the lower left alignment marker to the edge of the pattern, and the position of the center of the lower left alignment marker relative to the Faraday cup on the e-beam machine sample holder. Note that if the command "extent all" is used during file fracturing, the pattern center includes the entire pattern file, not just the layers that were fractured for a particular step.

Important parameters that must be considered during file preparation are the critical dimensions of the pattern, the corresponding beam current and beam step

size to realize those dimensions, and the e-beam accelerating voltage and exposure dose for the resist that will be used. The e-beam system will operate at a frequency that depends on these parameters; a higher frequency means a faster write time, but the system cannot operate at frequencies about 40 MHz. The frequency can be calculated by:

$$f = \frac{0.1 I_{beam}}{Dose\ BSS^2} \qquad \textbf{2.1}$$

Here I_{beam} is the beam current (in nano-amps), *Dose* is the exposure dose (in μC/cm^2), and *BSS* is the beam step size (in μm); the frequency is given in MHz. The choice of beam current depends in part on the critical dimensions of the pattern: a lower current corresponds to a smaller beam spot size, which is capable of writing smaller features. At 50 kV accelerating voltage (and using a 400 μm aperture), a beam current of 10 nA corresponds to a beam diameter of about 25 nm; a beam current of 100 nA corresponds roughly to a 95 nm beam diameter. Beam step size should be less than or equal to the beam diameter in order to have continuous lines. Exposure dose depends on the properties of the resist being used, as well as the electron mobility of the substrate. Most of my

work was done using a beam step size of 25 nm and a beam current of 25 nA. For ZEP resist (dose = 120 $\mu C/cm^2$), this led to a frequency of 33 MHz.

2.1.3 Process Parameters for Electron-beam Resists

2.1.3.1 Wafer Preparation Procedure

This section contains the process parameters used for five different resist configurations, including spin speeds and corresponding thicknesses, baking times and temperatures, exposure doses, development chemistry and times, and resist removal processes following metal deposition or etching. These parameters apply to 3" silicon wafers. Exposure doses will vary for other substrates. To prepare a wafer for resist deposition, the following procedure was used:

1. Clean wafer as needed (use plasma ash or solvent bath to remove old resist, use acid to remove oxide, etc).

2. Place wafer on spinner; while spinning wafer for 60 seconds at 4000 rpm, use spray bottles to rinse wafer with acetone, then methanol, and then IPA. Do not allow the wafer to dry when changing between solvents.
3. Bake wafer on hot plate for at least 3 minutes at 120°C or greater. This will help dehydrate the wafer and promote resist adhesion. While the wafer is baking, coat the inside of the spinner with aluminum foil to help keep it clean.
4. Blow the wafer with nitrogen for about 10 seconds to help remove any particles or any remaining water or solvent molecules from the surface. Also blow the pipettes with nitrogen before putting them in the resist bottles, in order to keep contaminants from entering the bottles.

After these steps, the wafer is ready for resist deposition. When applying the process parameters below, note that resist thickness may vary for a given spin speed as the resist ages and solvent evaporates. Also, depending on the viscosity of the resist it may be advisable to dynamically dispense the resist, i.e. dispense it on the wafer as the wafer is spinning at a relatively slow speed. This is often necessary to obtain a uniform coat of resists with higher viscosity, such as PMGI. In a typical process, one would spin the wafer at 300 rpm for 10 seconds and

dispense the resist onto the wafer during this time, then spin the wafer at 700 rpm for 5 seconds to spread the resist across the wafer, and then spin the wafer at the desired speed for the time given in the corresponding process.

2.1.3.2 PMMA

PMMA (polymethyl methacrylate) is a commonly-used polymer for positive-resist e-beam lithography. It is dissolved in anisole, and available in several viscosities and molecular weights [18]. In this work 950 PMMA A4 was used, which has a molecular weight of 950,000 and 4% solids in anisole, yielding thicknesses between 200 and 400 nm for spin speeds between 1000 and 4000 rpm. It is sensitive to x-rays and deep ultraviolet radiation as well as electrons. It can be removed with methylene chloride or acetone. The following steps are used for an e-beam process using a single layer of PMMA, after implementing the wafer preparation steps listed in section 2.1.3.1:

1. Dispense 950 PMMA A4 onto wafer; spin at 3000 rpm for 80 seconds.

2. Bake wafer on hotplate at 180°C for 10 minutes.
3. Expose wafer to e-beam, using dose of 350 μC/cm^2 with 25 nA beam, 25 nm resolution, and 25 nm step size.
4. Develop wafer for 2 minutes in 3:1 IPA:MIBK bath; move wafer to IPA bath, then rinse with IPA and dry with nitrogen.
5. Following metal deposition or etching, remove PMMA by soaking wafer in bath of methylene chloride or acetone for 10 minutes. Ultrasonic agitation can speed this up.

2.1.3.3 PMMA/Copolymer Bi-layer

The bi-layer process is useful in liftoff processes because the under-cut of the bottom layer promotes discontinuity of the deposited metal film (see section 2.1.4). The copolymer used here, EL9 MMA-copolymer, is closely related to PMMA, which explains the similarities in development and removal chemistry. It contains 9% solids in the solvent ethyl lactate, and spins on with a thickness of 400 nm at 3000 rpm. The following steps are used for an e-beam process using a

bi-layer of PMMA and copolymer, after implementing the wafer preparation steps listed in section 2.1.3.1:

1. Dispense EL9 MMA-copolymer onto wafer; spin at 2000 rpm for 60 seconds.
2. Bake wafer on hotplate at 180°C for 10 minutes.
3. Dispense 950 PMMA A4 onto wafer; spin at 3000 rpm for 60 seconds.
4. Bake wafer on hotplate at 180°C for 10 minutes.
5. Expose wafer to e-beam, using dose of 350 $\mu C/cm^2$ with 25 nA beam, 25 nm resolution, and 25 nm step size.
6. Develop wafer for 2 minutes in 3:1 IPA:MIBK bath; move wafer to IPA bath, then rinse with IPA and dry with nitrogen.
7. Following metal deposition or etching, remove PMMA/copolymer bi-layer by soaking wafer in bath of methylene chloride or acetone for 10 minutes. Ultrasonic agitation can speed this up.

2.1.3.4 ZEP 520A-7

ZEP 520A is a positive e-beam resist with high sensitivity and resistance to dry etching [19]. It provides higher resolution than PMMA. It is dissolved in anisole, and may be thinned with anisole to achieve desired film thickness. ZEP 520A-7 contains more solvent than ZEP 520A, and therefore has a lower viscosity (7 mPa-sec compared to 11 mPa-sec for ZEP 520A). Its thickness after spinning at 3000 rpm is about 280 nm. The developer used in this work was xylene, but amyl acetate can also be used (it provides slightly better resolution but requires a slightly higher exposure dose). The following steps are used for an e-beam process using a single layer of ZEP 520A-7, after implementing the wafer preparation steps listed in section 2.1.3.1:

1. Dispense ZEP 520A-7 onto wafer; spin at 3000 rpm for 80 seconds.
2. Bake wafer on hotplate at 180°C for 4 minutes.
3. Expose wafer to e-beam, using dose of 120 $\mu C/cm^2$ with 25 nA beam, 25 nm resolution, and 25 nm step size.

4. Develop wafer for 90 seconds in ZEP RD developer bath (xylenes); move wafer to IPA bath, then rinse with IPA and dry with nitrogen. Amyl acetate can also be used as developer; it requires a slightly larger dose but gives better resolution.
5. Following metal deposition or etching, remove ZEP 520A-7 by soaking wafer in bath of methylene chloride for 5 minutes. Ultrasonic agitation can speed this up.

If the resist layer is to be used as an etch mask, the use of an adhesion promoter and a longer bake time (or post-exposure bake) will help the resist withstand the etching conditions. Specifically, apply HMDS to the wafer before step 1 in the procedure above by dispensing it onto the wafer with a pipette and spinning the wafer at 3000 rpm for 80 seconds. It is not necessary to bake the wafer before proceeding to step 1. In step 2, the bake time can be increased to 10 minutes. Following step 4, an additional 10-minute bake can also be added.

2.1.3.5 ZEP 520A-7/PMGI Bi-layer

PMGI (polydimethylglutarimide) is a positive e-beam resist that is essentially insoluble in most common resist solvents [20]. This makes it ideal for bi-layer applications; with a different developer used for the top and bottom layers, the under-cut can be carefully controlled. PMGI is also useful as a sacrificial layer for air-bridge processes (see chapter 5). While its solvent is proprietary, Michrochem sells the solvent for thinning. PMGI SF7 yields a film thickness of 450 nm when spun on at 3000 rpm. The following steps are used for an e-beam process using a bi-layer of ZEP 520A-7/PMGI SF7, after implementing the wafer preparation steps listed in section 2.1.3.1:

1. Dispense PMGI SF7 onto wafer; spin at 3000 rpm for 80 seconds.
2. Bake wafer on hotplate at 180°C for 3 minutes.
3. Dispense ZEP 520A-7 onto wafer; spin at 3000 rpm for 80 seconds.
4. Bake wafer on hotplate at 180°C for 4 minutes.
5. Expose wafer to e-beam, using dose of 120 $\mu C/cm^2$ with 25 nA beam, 25 nm resolution, and 25 nm step size.

6. Develop wafer for 90 seconds in ZEP RD developer bath (xylenes); move wafer to IPA bath, then rinse with IPA and dry with nitrogen.
7. Develop wafer for 20 seconds in MF 701 developer bath (TMAH); move wafer to DI water bath, then rinse with DI water and dry with nitrogen. TEAH-based developer can also be used, especially if greater selectivity is needed (TMAH develops some other kinds of resist, including photo-resist).
8. Following metal deposition or etching, remove ZEP 520A-7 by soaking wafer in bath of methylene chloride for 5 minutes. Ultrasonic agitation can speed this up.
9. Remove PMGI SF7 by soaking wafer in bath of EBR-PG for 10 minutes. Ultrasonic agitation can speed this up.

Variable-angle spectroscopic ellipsometry was used to characterize the optical properties of PMGI from 2 - 40 μm. By measuring the change in phase and magnitude of polarization as light is reflected from the PMGI film, and then applying a generalized oscillator model to fit the data, I obtained the real and imaginary refractive index for this material, as shown in Figure 2-2. The mean squared error (MSE) for the curve fit was 0.8098 over the entire data range.

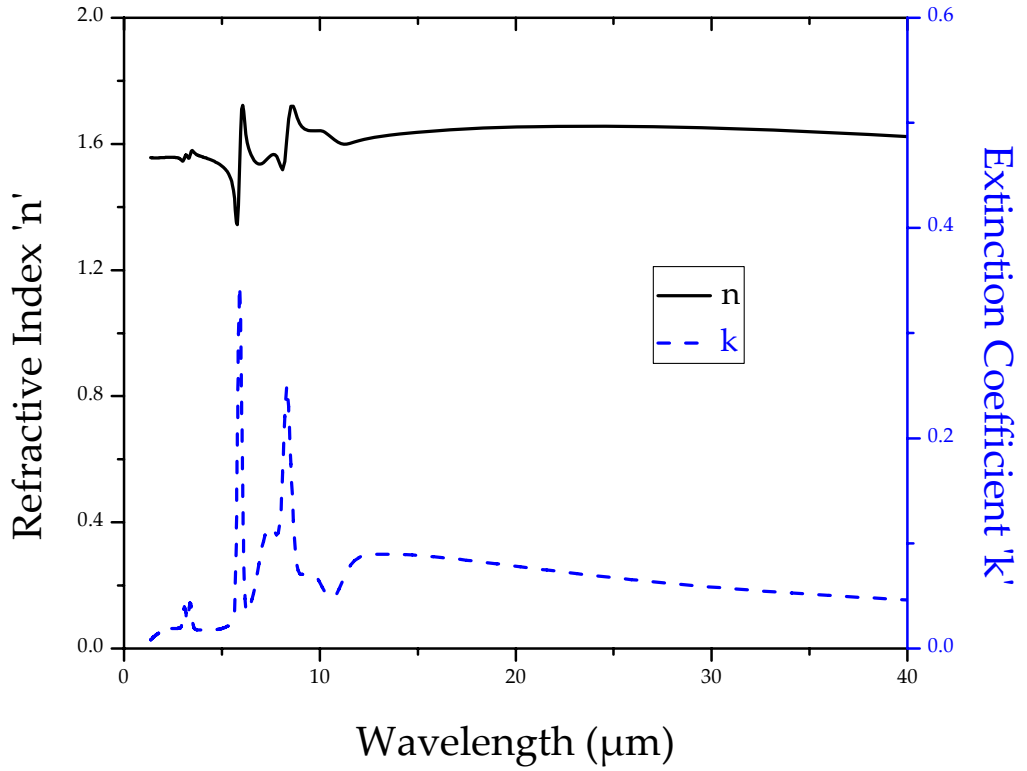

Figure 2-2: Optical constants for PMGI resist measured with ellipsometer from 2 - 40 μm

2.1.3.6 ZEP 520A-7/PMMA Bi-layer

PMMA was used as the bottom layer of a bi-layer process during air-bridge fabrication, since PMGI was being used as a sacrificial layer. The following steps are used for an e-beam process using a bi-layer of ZEP 520A-7/PMMA, after implementing the wafer preparation steps listed in section 2.1.3.1:

1. Dispense 950 PMMA A4 onto wafer; spin at 3000 rpm for 80 seconds.
2. Bake wafer on hotplate at 180°C for 10 minutes.
3. Dispense ZEP 520A-7 onto wafer; spin at 3000 rpm for 80 seconds.
4. Bake wafer on hotplate at 180°C for 4 minutes.
5. Expose wafer to e-beam, using dose of 160 $\mu C/cm^2$ with 25 nA beam, 25 nm resolution, and 25 nm step size.
6. Develop wafer for 90 seconds in ZEP RD developer bath (xylenes); move wafer to IPA bath, then rinse with IPA and dry with nitrogen.
7. Following metal deposition or etching, remove ZEP 520A-7/PMMA bi-layer by soaking wafer in bath of methylene chloride for 5 minutes. Ultrasonic agitation can speed this up.

2.1.3.7 Cyclotene (BCB)

Cyclotene is a commercially available thermosetting polymer material based on benzocyclobutene (referred to hereafter as BCB); it is useful as a spin-on dielectric material [21]. Because of its low dielectric loss and ease of processing, BCB is used as a standoff layer for antenna-coupled detectors over a ground plane (see chapter 6). The following steps are used to coat a wafer with BCB, after implementing the wafer preparation steps listed in section 2.1.3.1:

1. Descum wafer for 2 minutes in an O_2 plasma, with 400 mTorr O_2 and 200 W RF power.
2. Rinse wafer with de-ionized water while spinning at 4000 rpm for 60 seconds.
3. Bake wafer on hot plate at 180 °C for 5 minutes to dehydrate the surface.
4. Dynamically apply BCB adhesion promoter (AP 3000) by spinning wafer at 200 rpm for 5 seconds while dispensing adhesion promoter, and then spinning at 2500 rpm for 20 seconds.
5. Dynamically apply BCB by spinning wafer at 200 rpm for 5 seconds while dispensing BCB, spinning wafer at 500 rpm for 5 seconds to spread the resin, and then spinning at the required speed for the desired film thickness. For

Cyclotene 3022-35, 3000 rpm yields a film thickness of 1.4 μm. Thinner BCB films can be obtained by diluting Cyclotene 3022-35 with its solvent, mesitylene.

6. Bake wafer on hot plate at 120 °C for 3 minutes.
7. If a soft cure is required (e.g. if another layer of BCB will be added), bake wafer on hot plate at 180 °C for 3 minutes in a nitrogen atmosphere. Curing the film in the presence of oxygen can cause oxidation of the film and affect its optical properties. A nitrogen atmosphere is obtained by flowing nitrogen into a stainless steel cover that rests on the hot plate.
8. For a hard cure, bake wafer on hot plate at 250 °C for 5 minutes in a nitrogen atmosphere.

BCB is etched in a CF_4/O_2 plasma, usually with ZEP 520A e-beam resist as an etch mask. The etch process is described in section 2.4.2 of this work. BCB is difficult to remove. After baking or soft-curing, solvents can be used to remove the film; after a hard cure, the film can only be removed by plasma etching or an aggressive wet etch such as fuming nitric acid or H_2O_2/H_2SO_4 baths [22].

As with PMGI, ellipsometry was used to determine the optical properties of BCB. The ellipsometric data for BCB proved difficult to model. A generalized oscillator was developed to fit the data and provide the optical constants. Figure 2-3 and Figure 2-4 show the model fit to the data for 1.4 μm of BCB on a Si wafer, which resulted in an MSE of 2.407 with the range limited to 25 μm. Figure 2-5 shows the resulting optical constants.

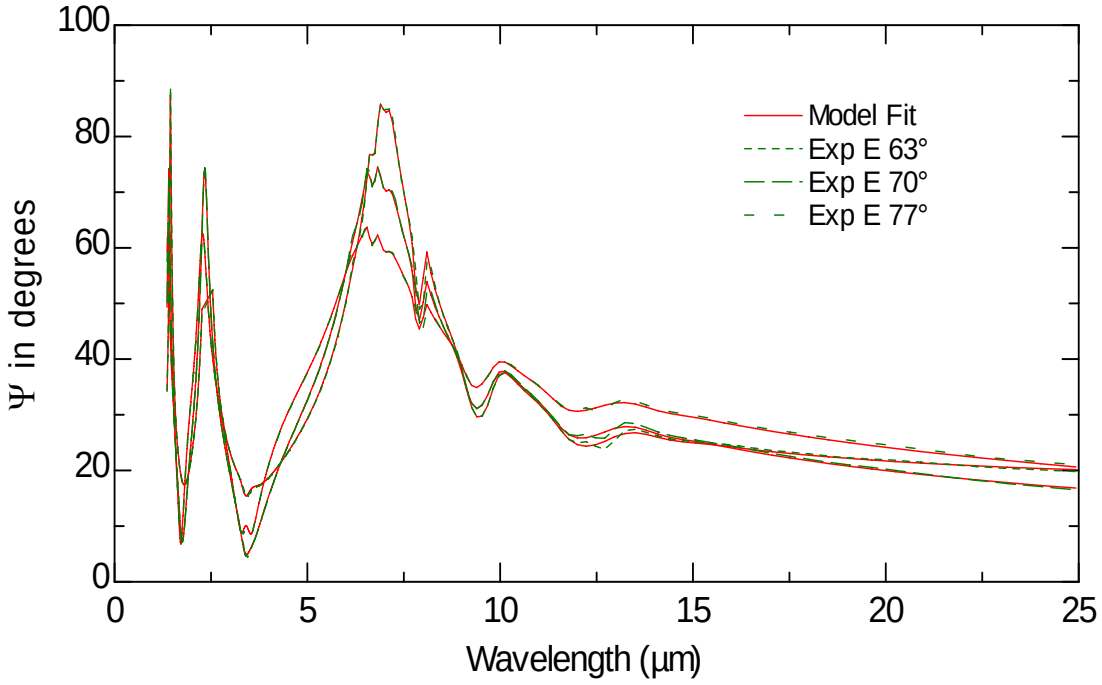

Figure 2-3: Ellipsometric data for BCB with generalized oscillator model fitting psi for 2 - 25 μm range

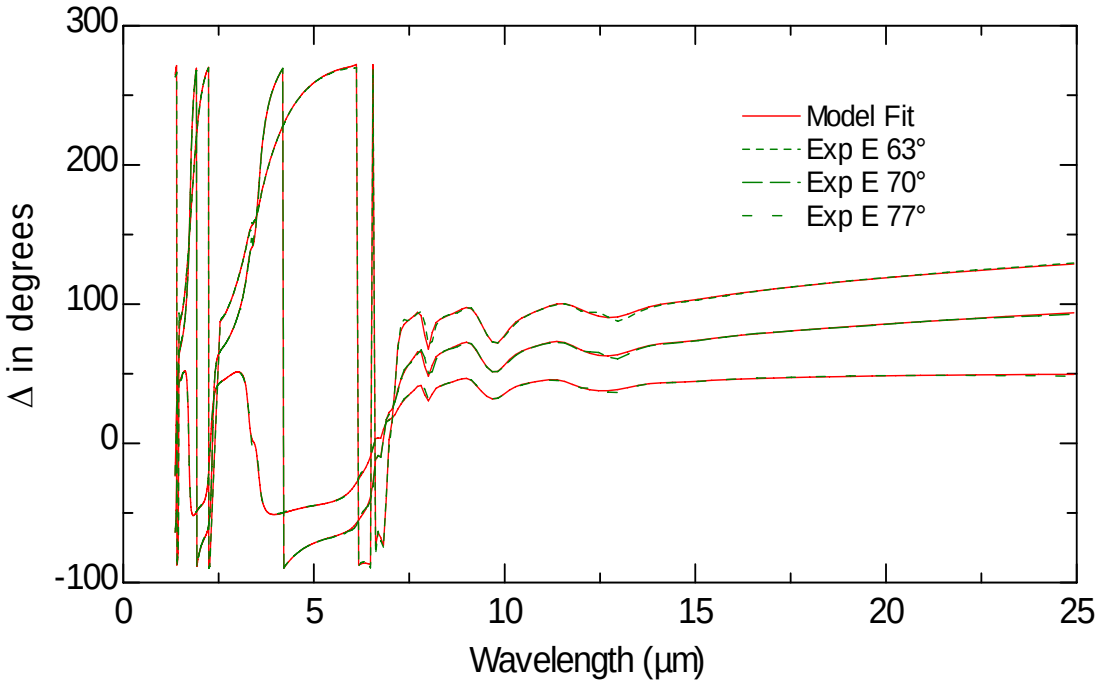

Figure 2-4: Ellipsometric data for BCB with generalized oscillator model fitting delta for 2 - 25 μm range

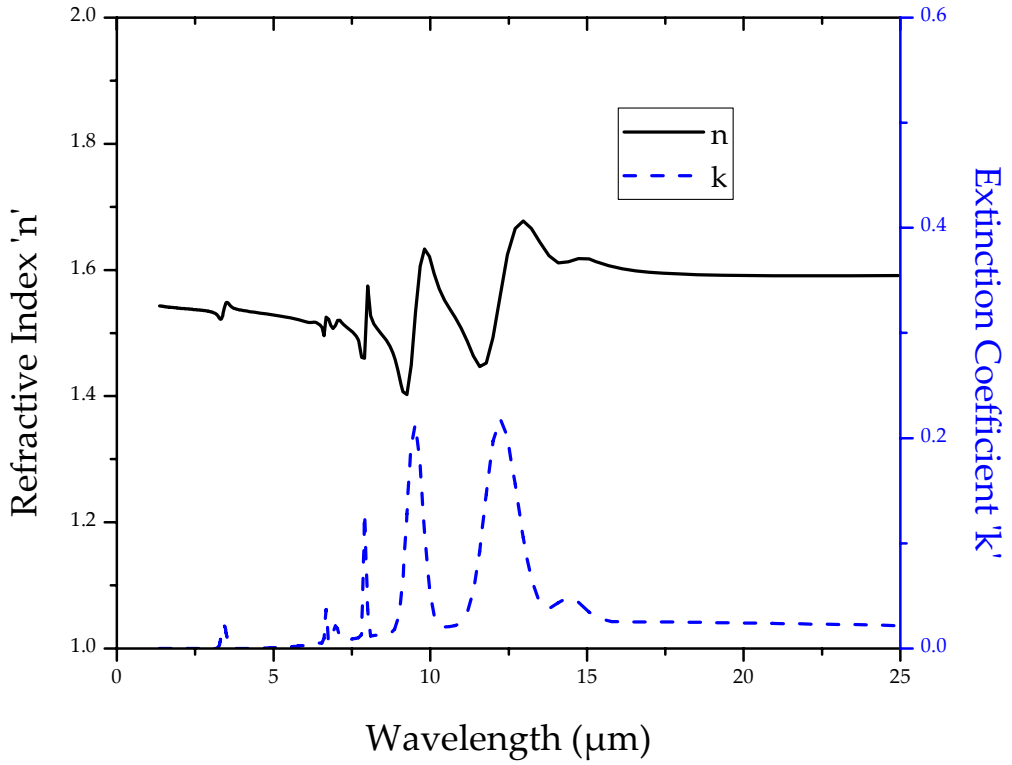

Figure 2-5: Optical constants for BCB measured with ellipsometer for 2 - 25 μm

2.1.3.8 Resist Descum Process

After resist has been exposed and developed, it is often necessary to descum the substrate before metal deposition. This is done by placing the developed wafer in an O_2 plasma and essentially etching the resist layer slightly. This isotropic etching of 5 - 10 nm of the resist should then completely remove any residue from the substrate which may otherwise hinder metal adhesion to the substrate. The residue seems to be caused generally by insufficient exposure or development. Therefore the descum process may not be necessary if the correct exposure dose and development time were used. But the removal of a few nanometers of resist shouldn't adversely affect the lift off process.

The descum process can be accomplished by sputter etching the resist with an O_2 plasma in the sputterer, but it is most commonly done in a barrel etcher. With 400 mTorr O_2 pressure in the chamber and 200 W RF power, the etch rates shown in Table 2-1 were measured for several resists.

Table 2-1: Etch rates for four kinds of e-beam resist for descum process in 400 mTorr O_2 plasma with 200 W RF power

Material	Etch Rate (nm/sec)
950 PMMA A4	10.8
MMA(8.5):MAA EL9 (copolymer)	8.3
PMGI	4.8
ZEP 520A	3.9

2.1.4 Lift-off Process

Most of the lithography done in this work used an additive process known as liftoff. In this process, a pattern is defined in a resist layer through exposure and development, and a thin film of metal is deposited over the entire substrate. In the portions of the substrate where the resist has been removed through development, the metal adheres to the substrate; elsewhere the metal rests on top of the resist layer. When solvent is used to remove the resist layer, the metal on top of it is removed as well.

Often a bi-layer of resist is necessary to perform the liftoff process. In general, the total thickness of the resist layer should be three times the thickness of the deposited metal film. A bi-layer helps ensure discontinuity between the metal film resting on the resist layer and the metal deposited onto the substrate as demonstrated in Figure 2-6 [23], in which a PMMA/copolymer bi-layer is used (see section 2.1.3.3 for process details).

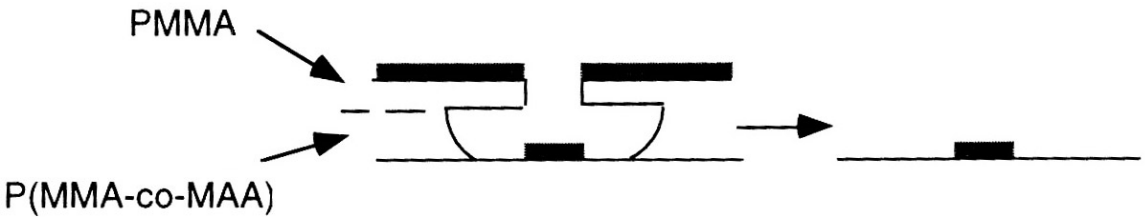

Figure 2-6: The effect of a resist bi-layer on the liftoff process, demonstrated with a PMMA/ copolymer resist bi-layer

The three different bi-layer processes presented in section 2.1.3 allow a varying degree of undercut for this process. In the final step of liftoff, when the metal film and resist layer are removed, the wafer is normally placed in a bath of the appropriate resist removal solvent. As the resist dissolves and the metal lifts off of the substrate, one must carefully avoid allowing the metal particles to settle

and dry onto the substrate, which makes them very difficult to remove (wet etching of the metal is generally the only way to remove these particles in this case, which will also remove the lithographically-defined structures). Usually this can be avoided by rinsing the wafer with acetone as it is being removed from the solvent bath. Placing the wafer upside-down in the solvent can also help.

For some resist layers, the metal adheres weakly to the resist and can be removed prior to resist removal by applying cellophane tape to the wafer. The metal on the resist layer is then easily removed, and the metal on the substrate remains. Removal of the resist layer is then a simpler matter. This technique is effective with ZEP 520A and PMMA resists, but the adhesion of the metal is generally too strong to photoresist and PMGI. For these resists, a solvent bath is the best method.

2.2 Optical Lithography

All of the optical lithography was performed on a Karl Suss MJB3 contact aligner. Here is a typical process using Shipley positive-tone photo resist:

1. Follow wafer cleaning procedure as outlined in section 2.1.3.1.
2. Dispense Shipley resist onto wafer, spin at 2000 rpm for 30 seconds.
3. Bake wafer on hotplate at 120°C for 10 minutes
4. Expose wafer using MJB3 contact aligner. For S1805 resist, an exposure time of 10 seconds to 275 W radiation works well. For S1818 resist, an exposure time of 30 seconds will do.
5. Develop wafer for 30 seconds in MF 701 developer bath (TMAH); rinse with DI water and dry with nitrogen.
6. Resist removal: acetone.

Most of the lithography done for this dissertation was performed using e-beam processes. Since line widths for most of the antennas were smaller than the best resolution possible with the contact aligner, and also since there was not an in-

house mask-writing tool, optical lithography was used in only a few cases. Examples of uses for optical lithography include arrays of 250 μm x 250 μm squares for thin film thickness characterization with a profilometer, bond pads and alignment marks for successive e-beam lithography steps for infrared devices, and some millimeter-wave antennas.

2.3 Thin Film Deposition

Several techniques have been used to deposit the thin films used in this dissertation: electron-beam and thermal evaporation, sputtering, and plasma-enhanced chemical vapor deposition. A significant amount of process development was required to arrive at repeatable thin film deposition processes. This section gives some practical details of these processes. More information can be found in [24-26].

2.3.1 Evaporation

2.3.1.1 Electron-beam Evaporation

Because of differences in atomic weight, melting point, and vapor pressure, each metal evaporates differently. Below are some comments on the evaporation of four metals: Au, Ni, Ti and Al.

Au is best evaporated in a thermodynamic W crucible, which allows the evaporant to heat up more quickly. The crucible is designed so that its base fits in the copper pocket of the evaporator, but its walls are not in contact with the water-cooled copper walls of the pocket. Metals with high melting temperatures are thus able to be melted more quickly. However, Au wets the W crucible when it melts, and therefore it may run over the side of the crucible and create a short to the hearth of the e-beam chamber. This can be avoided by keeping the e-beam current low. Usually a rate of 10 Å/second can be achieved with an e-beam current of 78 - 80 mA. Exceeding this current may also cause the substrate to over-heat, which may damage the e-beam resist and create problems with lift-off. Heating effects are mitigated by placing the substrate on a water-cooled copper

block at the top of the chamber. Also note that at higher currents, the evaporant may spit. After the evaporation is complete, the chamber should sit for at least 10 minutes to cool down before being vented.

For the evaporation of Ni, a vitreous carbon crucible is necessary. But due to reflections and the large amount of heating required to evaporate Ni, the crucible can be easily destroyed by reflected electrons drilling through it or by thermal shock as the evaporant cools. To avoid holes from reflected electrons, one can sweep the e-beam around the crucible at a low speed. Thermal shock damage can be avoided by allowing the crucible to cool slowly by gradually reducing the current after evaporation. For an e-beam current of 100 mA, Ni can be evaporated at 3 Å/second.

Ti is evaporated without a crucible liner. It is an important metal for the adhesion of Au, and is most commonly used in combination with Au. A typical adhesion layer of Ti is 5 - 8 nm thick. Ti is also known as a "getter:" as it evaporates, it absorbs or reacts with residual gases and can therefore be used to further decrease the chamber pressure. For an e-beam current of 120 mA, Ti can be evaporated at 3 Å/second.

Al is evaporated in a thermodynamic W crucible. As with Au, Al will quickly wet the W crucible and run over the edge if the current is too high. An e-beam current of 60 mA gives an evaporation rate of 10 Å/second.

2.3.1.2 Thermal Evaporation

Many of the materials that are evaporated by an e-beam source can also be evaporated thermally, where the material is heated by an electric current running through a resistive boat. The materials evaporated thermally in this dissertation were Cr, Bi and SiO.

Cr is commonly used as an adhesion layer with Au. During evaporation it does not melt, but sublimes. Subliming materials can potentially contaminate an evaporation chamber, since they may evaporate from the chamber walls when another material is being evaporated if the temperature of the walls rises enough. Cr is also a getter material, and is commonly used as an etch mask. For thermal

evaporation, Cr is evaporated from a W boat. It may also be coated on a W wire and evaporated as current passes through the wire.

Bi is a highly resistive metal and is often used as a bolometer. Like Cr, it sublimes. Evaporation of Bi is performed in a boat of Al_2O_3. SiO can be used as an electrical passivation layer. It is also evaporated thermally in an Al_2O_3 boat. Resistive currents vary for these three materials, depending on the condition of the boat and the amount of evaporant in the boat. It is best to adjust the current to achieve a constant deposition rate, generally not exceeding 10 Å/second.

2.3.2 Sputter Deposition

Sputter deposition was performed with a variety of targets, including Ni, Ti, Cr, V, and Au. RF and DC magnetron sources were used as needed. As targets are depleted, deposition rates and uniformity change. For most processes, platform rotation of the substrate was used to improve deposition uniformity. A chamber pressure of 4 - 6 mTorr was used, with 20 sccm Ar flowing into the chamber, and

a throttle valve allowing manual control of the pressure. Since sputter deposition lacks the directionality of evaporation, it was not the preferred method of deposition, and was used only when a material could not be evaporated, or when the evaporation system was unavailable.

2.3.3 Plasma-Enhanced Chemical Vapor Deposition

Plasma-enhanced chemical vapor deposition was used to deposit thin films of SiO_2 on Si wafers. This process was chosen over thermal oxide growth because of the relatively lower process temperature and the ability to deposit oxide on metal. A Unaxis deposition system was used for this process. The substrate was raised to a temperature of 250 °C, and the following parameters were applied: 1050 mTorr chamber pressure, 400 sccm SF_4, 827 sccm N_2O, 25 W RF, and a DC bias voltage of 0 - 2 V. These conditions yielded a deposition rate of 50 nm/min with excellent uniformity over a 3" wafer.

2.4 Etching

2.4.1 Dry Etching

Reactive ion etching was the only dry etch process used in this dissertation, with the exception of the plasma etching step used for the resist descum process as explained in section 2.1.3.8. Dry etching was performed in a Unaxis RIE/PECVD system. Etching processes were adapted for SiO_2 and BCB, using ZEP 520A e-beam resist as an etch mask (as in section 2.1.3.5). Table 2-2 gives the details for both etch processes, including gas flow rates, RF power levels, chamber pressure, and etch rates.

Due to contaminant by-products from etching, an additional process step is necessary to clean the chamber every time the chamber is used to etch BCB. This process consists of oxygen cleaning and silicon nitride etching. The oxygen clean requires a chamber pressure of 200 mTorr with 50 sccm O_2, 20 sccm He, 250 W RF, and 396 V DC bias for 15 minutes. The silicon nitride etch takes a 75 mTorr chamber pressure, 1.2 sccm O_2, 20 sccm CF_4, 200 W RF, and 375 V DC bias for 20 minutes. More information on BCB etching can be found in [27].

Table 2-2: Process parameters for RIE etching of SiO_2 and BCB with ZEP 520A e-beam resist as an etch mask

Etch Parameters	**SiO_2**	**BCB**
Chamber Pressure (mTorr)	75	50
O_2 flow rate (sccm)	5	10
CF_4 flow rate (sccm)	45	5
RF power (W)	175	100
DC Bias Voltage (V)	334	281
Material Etch Rate (nm/min)	50	130
ZEP 520A Etch Rate (nm/min)	80	140

2.4.2 Wet Etching

Several chemical etch processes were developed for materials that are difficult to dry etch, or for processes that depended on the isotropic nature of wet etching. Buffered oxide etch (BOE) was used to etch SiO_2. With a 9:1 concentration (9 parts ammonium fluoride to one part hydrofluoric acid), thermally-grown SiO_2 was etched at a rate of 550 Å/minute. S1818 photo-resist was used as an etch mask, and was virtually undamaged by the etchant.

InP was etched with HCl, either in combination with H_2O or $HP3O_4$. E-beam resist provided an excellent mask for either etchant. For [100] InP, 1:1 H_2O: HCl etched the substrate at a rate of 0.65 μm/minute, but the side walls were very rough and the [111] plane etched much faster (~ 0.9 μm/minute). The same wafer was etched by 3:1 HP_3O_4: HCl at a rate of 0.6 μm/minute, and had much smoother side walls and better etch uniformity. InGaAs was etched in 4:1 $C_6H_8O_7$: H_2O_2, with good uniformity and an etch rate of 120 Å/minute.

CHAPTER 3

DEVICE MEASUREMENT

3.1 Infrared Test Setup

3.1.1 Spectral Measurement Setup

Spectral measurements were obtained by focusing radiation from a tunable CO_2 laser onto an antenna-coupled device. Figure 3-1 shows a diagram of the spectral measurement setup. The laser source has a manually-tunable wavelength range of 9.3 - 11.2 μm. The wavelength is adjusted by changing the position of a grating inside the laser box, and it is monitored with a spectrometer. Most of the ~40 W laser beam is diverted by a beam splitter. Since the beam is linearly polarized, the remaining output power is controlled by a wire grid polarizer after the beam splitter. A half-wave plate is used to adjust the linear polarization to the desired state. The beam is then focused through a mechanical chopper for signal modulation. A collimating lens is followed by a focusing lens of desired F/#. The test setup is aligned for F/1 and F/8 lenses.

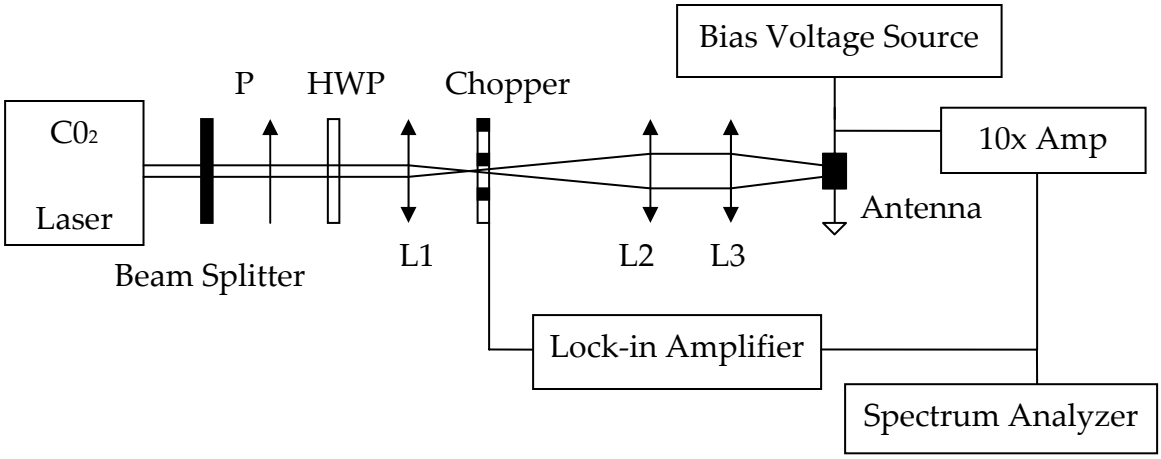

Figure 3-1: Test setup for spectral IR measurements using tunable CO_2 laser source

The device under test is placed on a three-axis translation stage with micrometer-precision translation control. Knife-edge scans are used to verify the focus and beam diameter of the laser at F/1 and F/8. Amplifiers, low- and high-pass filters, and a bias voltage source are applied externally to the device, and the signal is observed with a lock-in amplifier, spectrum analyzer, or oscilloscope.

The power incident on the detector is determined by measuring the incident laser power with a large-area thermal detector. The incident power on the detector is then the total laser power multiplied by ratio of the effective area of the device and the laser beam spot area, which was measured using knife edge

scans. The effective area of the device is obtained through 2D scanning and a deconvolution with the laser beam, as described in [12]. Depending on the laser line in use, the power of the laser was typically set at 5 - 10 mW. The F/8 spot diameter was measured to be 250 μm (not quite diffraction-limited, which would be 207 μm). For the square spiral antenna used in most of this work, the deconvolution showed an effective device area of ~ 12.5 μm^2. Thus the power incident on the device is 1.6% of the total power, typically 8 - 16 μW.

3.1.2 Blackbody Measurement Setup

The blackbody measurement setup is similar to the spectral measurement setup, without the focusing or polarizing optics. Figure 3-2 shows a diagram of the blackbody measurement setup. The blackbody source has a 2" aperture and temperature range from 25 - 1200 °C. A non-metallic chopper wheel with correspondingly large openings is placed ~1" from the blackbody aperture. A metal chopper wheel introduces noise. The device is positioned immediately behind the chopper wheel. No optical elements are necessary because the field

of view of the device is filled by the blackbody aperture if the device is close enough to the source. However, future measurements could benefit from focusing mirrors or other optical elements that would allow a larger distance from the source, since the chopper wheel deforms and starts to melt when the blackbody is operated at 1200 °C. Bias circuitry and amplification is used in the same manner as in the spectral measurement setup.

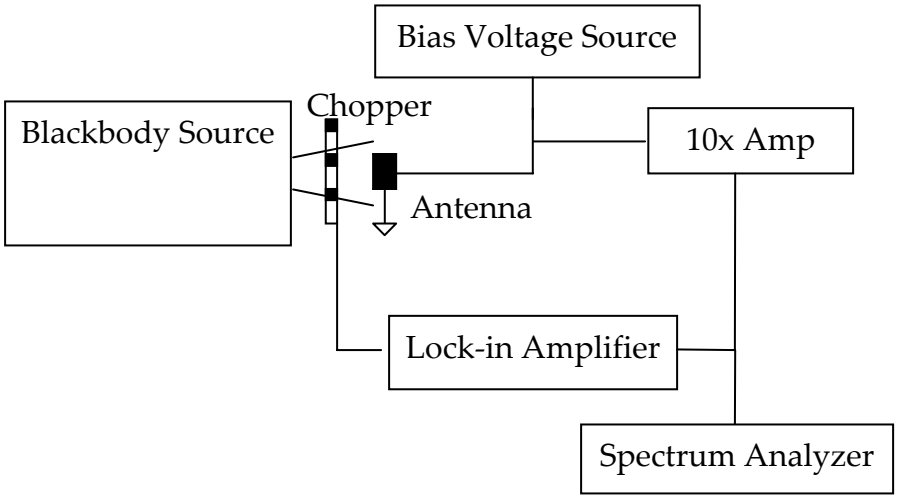

Figure 3-2: Test setup for blackbody measurements using 2" aperture 1200 °C blackbody source

3.2 Millimeter-wave Test Setup

Millimeter-wave measurements were performed with a setup shown in Figure 3-3. A Gunn diode is modulated by a voltage-controlled switch, controlled by a function generator. The modulated signal passes through an isolator to prevent reflected power from damaging the source. The components are connected with WR-10 waveguide. A horn antenna sends the modulated radiation to the device, mounted on a three-axis micropositioner stage. The same bias circuitry and amplifiers used for infrared measurements are also applied to the millimeter-wave devices, and the signal is read on a lock-in amplifier or spectrum analyzer.

The power incident on the detector is measured at the position of the detector with a calorimeter. This measurement is compared to the power output of the source immediately before the horn antenna as measured with a waveguide power meter. With the horn antenna dimensions, rough calculations for the propagation of the radiation showed that the calorimeter measurement corresponded closely to the waveguide measurement.

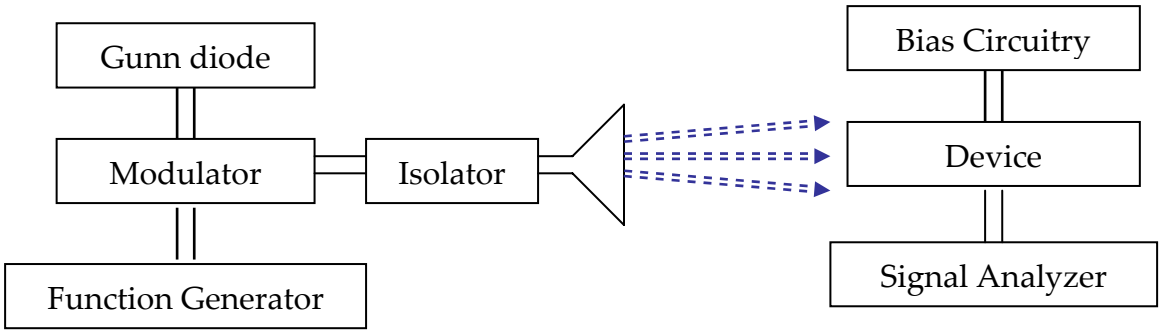

Figure 3-3: Diagram of millimeter-wave test setup

3.3 Noise Measurements

The main sources of noise for an antenna-coupled bolometer are Johnson noise, due to the resistance of the device; shot noise, which comes from the bias voltage; and 1/f noise, due also to the bias voltage and impurities in the device materials. Noise measurements are obtained with a dynamic signal analyzer. Device noise is determined by measuring the total noise of the system with the biased device, and then measuring the system noise with a resistor in place of the device. The Johnson noise of the resistor is calculated, and the system noise without the

resistor's Johnson noise is subtracted from the total noise, to obtain the device noise [13]. The Johnson voltage noise is given by

$$v_j = \sqrt{4kTR\Delta f} \tag{3.1}$$

Since noise terms add in quadrature, the actual system noise voltage, v_s, can be found from the measured system noise voltage, v_m:

$$v_s = \sqrt{v_m^{\,2} - v_j^{\,2}} \tag{3.2}$$

The device noise, v_{device}, is then determined from the total noise, v_{total} (system noise with device present) and the system noise, v_s:

$$v_{device} = \sqrt{v_{total} - v_s} \tag{3.3}$$

The noise figure from the dynamic signal analyzer is taken at the chopping frequency used for signal measurements. Figure 3-4 shows total noise spectra obtained for an antenna-coupled bolometer with a 62-mV bias, at two

temperatures: 300 K and 77 K. Both measurements were made with the device under vacuum (~ 1 x 10^{-6} Torr). The difference in noise level is due mainly to the temperature dependence of the Johnson noise term. Figure 3-5 demonstrates this by showing the same noise spectra, with the 77 K spectrum multiplied by the ratio of the two temperatures (300/77) to account for the Johnson noise term. Spikes in the two spectra are 60 Hz power line harmonics. The measured noise figure for antenna-coupled bolometers at room temperature was typically in the range of 5 - 10 nV/√Hz. The system bandwidth for the dynamic signal analyzer was 10 Hz.

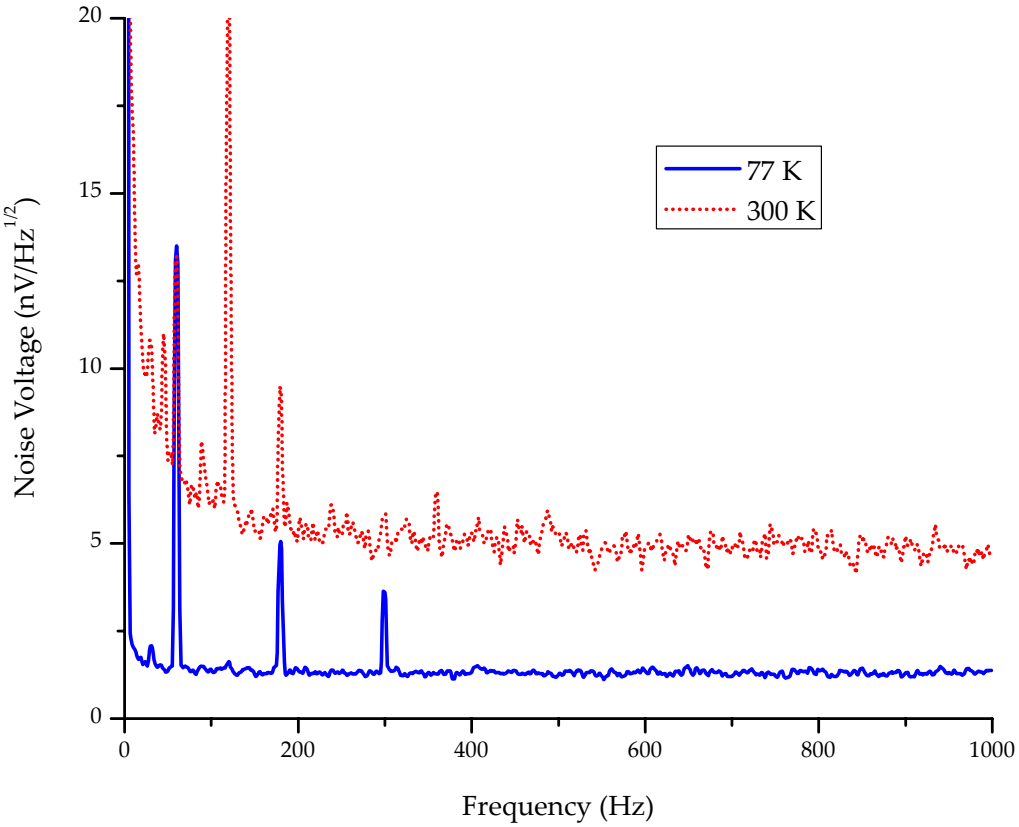

Figure 3-4: Noise voltage spectra for an antenna-coupled bolometer measured at 300 K and 77 K, both at 1 μTorr pressure.

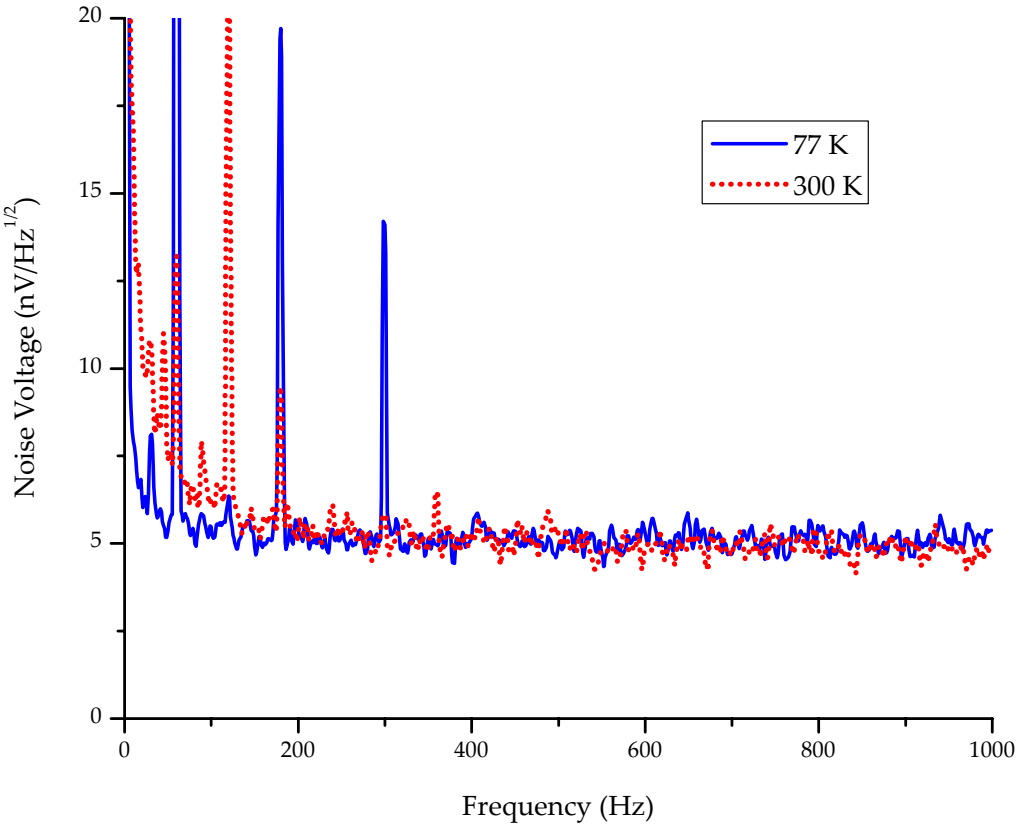

Figure 3-5: Noise voltage spectra for an antenna-coupled bolometer at 300 K and 77 K, with the 77 K spectrum multiplied by 300/77 to account for the temperature dependence of the Johnson noise term.

CHAPTER 4

MILLIMETER-WAVE DEVICES

In this chapter I describe the fabrication and measurement of two millimeter-wave devices: an array of Ni bolometers coupled to slot antennas, and a Schottky diode built on laser-doped SiC and coupled to a patch antenna. Some modeling efforts are described, with simulations developed to improve antenna performance. These projects led to further work on Schottky diodes, with the goal of extending the diode cutoff frequency to the infrared. I will conclude the chapter with some considerations in the development of an infrared antenna-coupled Schottky diode.

4.1 Slot Antenna-coupled Bolometer Array

An 8-by-8 millimeter-wave focal plane array was fabricated and tested, using antenna-coupled micro-bolometers as sensors [28]. The array consisted of slot

antennas coupled to nickel bolometers and was fabricated using optical and e-beam lithography on high-resistivity silicon wafers.

4.1.1 Device Design and Fabrication

The array consisted of 64 Ni micro-bolometers coupled to slot antennas (Figure 4-1). Each array element was designed for operation at 94 GHz, with an RF bandwidth of 20 GHz, based on a simulation using IE3D. The array elements were spaced $\lambda/2$ (1.5 mm) apart. The ground plane of each slot antenna was divided into two electrically isolated sections in order to bias the bolometers.

I used optical lithography to create the array pattern on a high-resistivity (> 8000 Ω cm) 3" double-side polished Si wafer, and deposited 15 nm of electron-beam-evaporated Cr and 70 nm of thermally-evaporated Au, using the lift-off process described in chapter 2. The slot antenna was 15 μm wide and 574 μm long, and the lines separating the positive and negative sides of the ground plane were 15 μm wide.

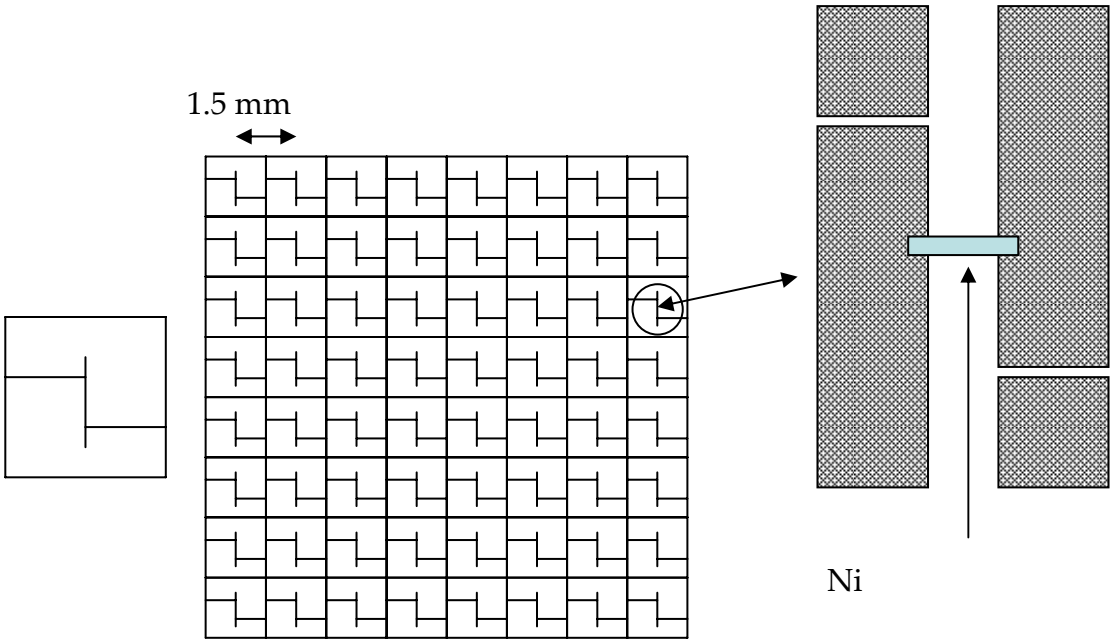

Figure 4-1: 8 x 8 array of slot antennas coupled to Ni micro-bolometers for 94 GHz detection.

The bolometers were written with an electron-beam lithography system and deposited by dc sputtering Ni. Nickel was chosen as the bolometric material because it has a slightly higher TCR than most other metals, 0.6%/°C. Although I used electron-beam lithography to create the bolometers, the dimensions of the bolometers (2 x 30 μm) would allow the use of optical lithography as well.

Figure 4-2 shows one of the array elements; Figure 4-3 shows a closer view of the bolometer.

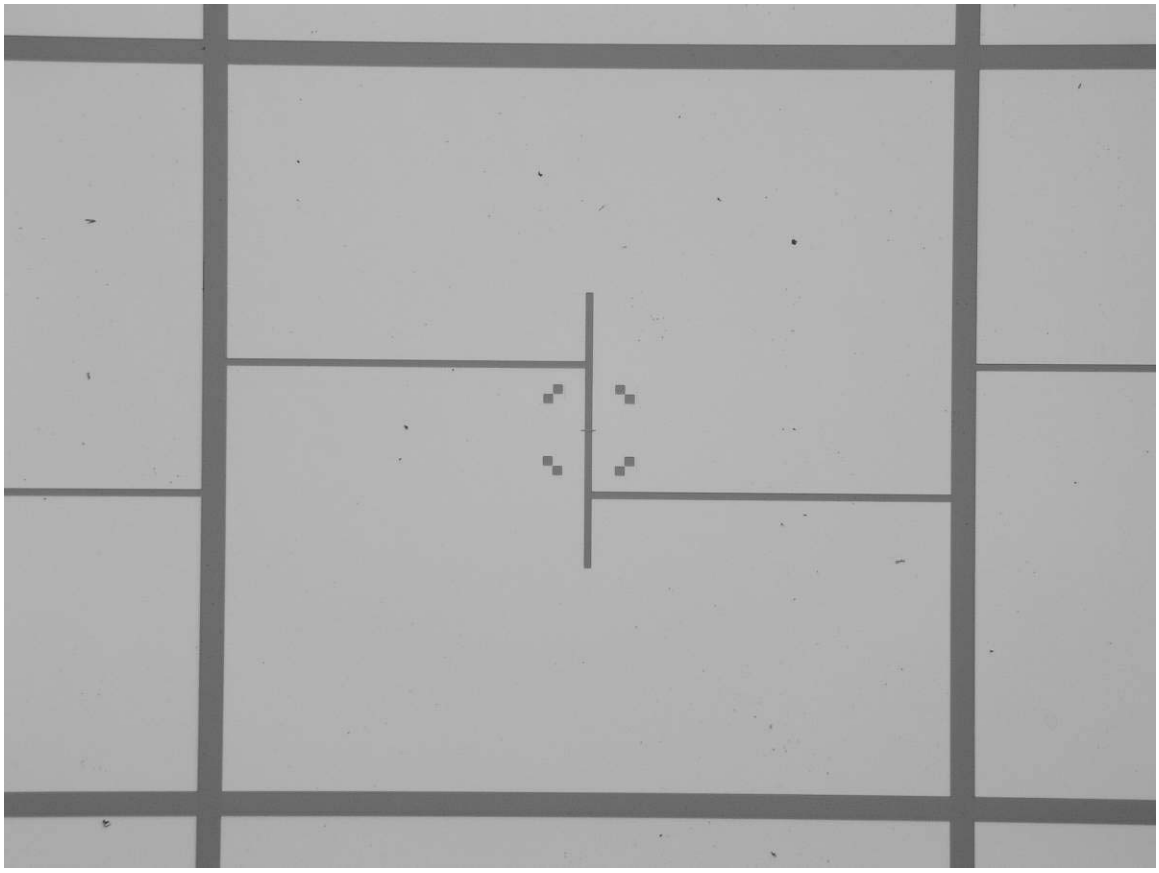

Figure 4-2: Image of a single element in the 8x8 slot antenna array

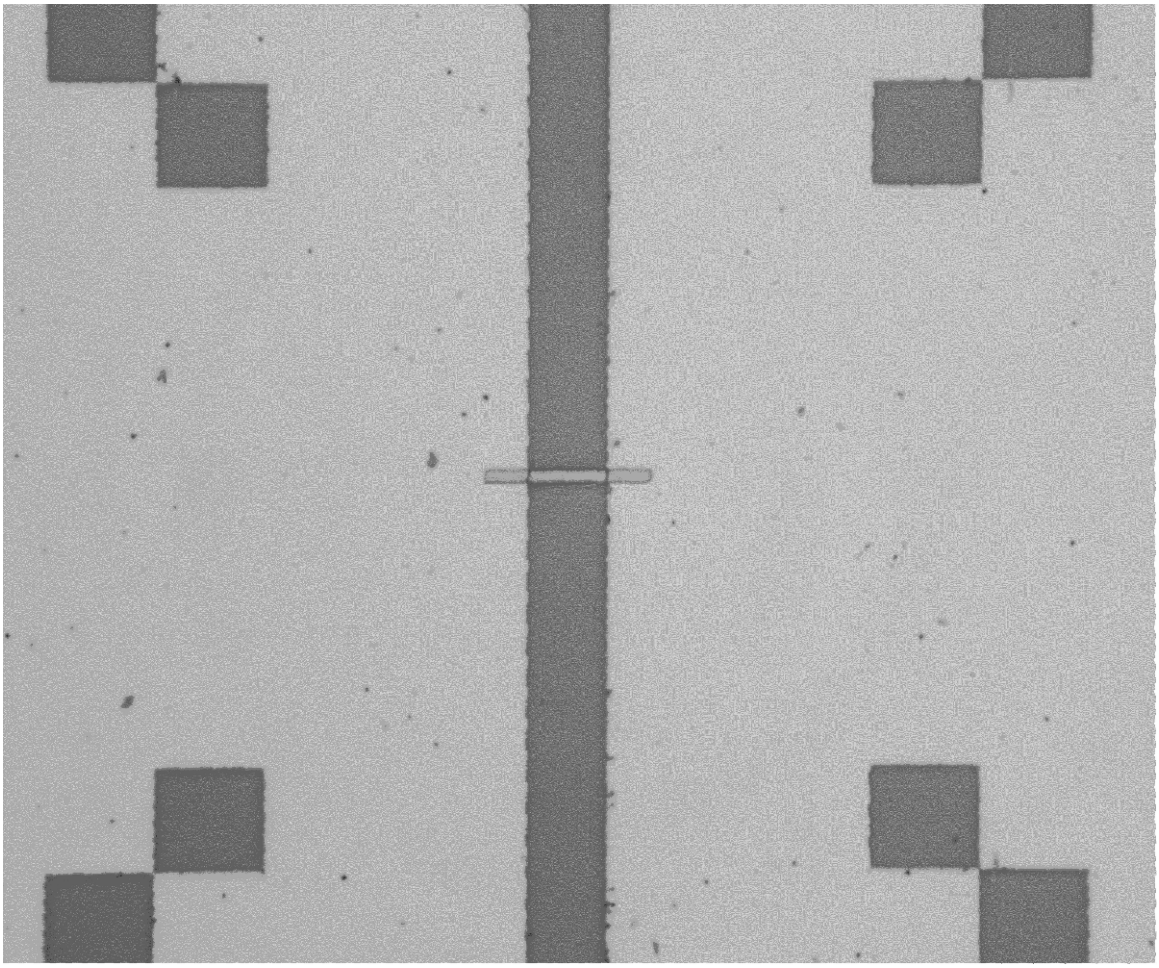

Figure 4-3: Image of a Ni bolometer coupled to a mm-wave slot antenna

4.1.2 Device Measurement Results

I measured the response of individual array elements to 94 GHz radiation from a Gunn oscillator. The test setup is shown in Figure 3-3. Radiation from the Gunn diode was modulated at the video frequency and launched into free space through a horn antenna. The array element was illuminated through the Si substrate and connected to an aluminum oxide chip carrier by aluminum bond wires. The bolometer was given a DC bias of 100 mV, and the signal was sent through a series of filters and amplifiers. By modulating the 94 GHz signal at a lower frequency I observed the signal in the frequency domain on a signal analyzer.

This measurement setup gave me the ability to easily measure the attenuation of different materials at 94 GHz. I placed each sample in the path between the horn antenna and my array element and compared the measured signal to the unobstructed signal. The results are summarized in Table 4-1.

Table 4-1: Attenuation of various materials measured at 94 GHz with a single element of the mm-wave antenna-coupled bolometer array

Material	Attenuation (dB)
Cotton fabric	2.4
5/8″ dry wall	3.2
Padded cardboard shipping envelope	5.2
320-grain sandpaper	5.3
Anti-static cardboard shipping envelope	10.1
Leather	12
120-grain sandpaper	20
Lead-lined x-ray-proof film pouch	20.9
Proceedings of SPIE, Volume 4719 (412 pages)	37.7
Aluminum foil	68
Noise floor	70.4

The measured response of a single array element was 1.18 μV at 30 Hz, with 68 nW of flux onto the device and a noise level of 330 pV/√Hz. The noise equivalent power (NEP) and noise equivalent temperature difference (NETD) of the sensors are calculated according to equations 1.1 and 1.4, where ϕ_e is the radiant flux (in

Watts), v_{sig} is the detected signal voltage (in Volts), v_n is the noise voltage (in Volts/√Hz), b is the video bandwidth (in Hz), k is Boltzmann's constant, and B is the RF bandwidth of the antenna. From these measurements I calculated a noise equivalent power (NEP) of 14.5 pW/√Hz and a noise equivalent temperature difference (NETD) of 206 K.

4.2 Antenna-Coupled Schottky Diode on Laser-Doped Silicon Carbide

4.2.1 Device Design and Fabrication

Silicon carbide is a useful material for high-temperature and high-power applications because of its wide bandgap. However, it presents some processing challenges, as the cleaning, doping, fracturing, and metal adhesion characteristics are different from most commonly-used semiconductors such as Si and GaAs. After dicing a lightly-doped single-crystal n-type wafer of 4H-SiC, I prepared the pieces for processing by following a standard cleaning process using H_2SO_4, H_2O_2, and HF [29].

Ohmic contacts were formed with a laser direct metallization process. In this metallization process a pulsed, frequency-doubled Nd:YAG laser (λ = 532 nm) is used to alter the stoichiometry of the substrate by changing regions of the SiC into either Si-rich or C-rich phases through coupling of photonic and thermal energy from the beam to the substrate. For a given set of processing conditions, these phases can be tuned to create conductive, semi-conductive, and insulating phases. Ohmic contacts were formed on SiC using a scanning speed of 30 mm/s, focused beam diameter of 300 μm, pulse energy of 2.5 mJ/pulse, and pulse width of 100 ns.

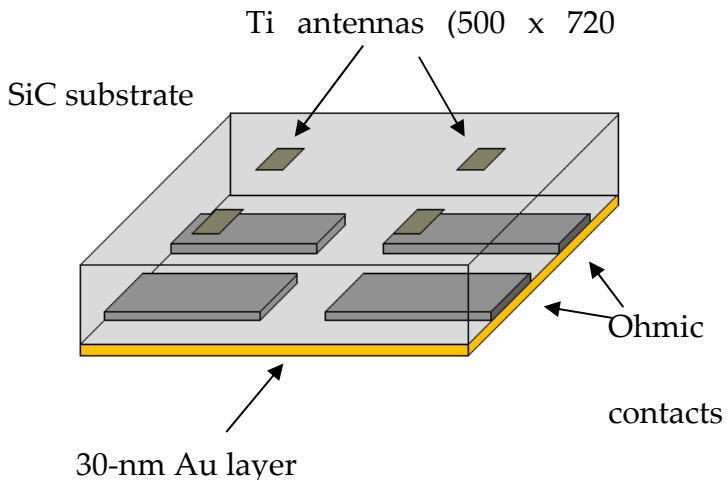

Figure 4-4: Three-dimensional view of SiC Schottky diodes and mm-wave patch antennas

To form a Schottky contact I used DC-magnetron sputter-deposited titanium on the non-metallized side of the wafer (see cross section, Figure 4-4). The Schottky contact also acted as a patch antenna whose dimensions were chosen for operation at 92.5 GHz. I used the following design equations [30] to determine the width and length of the patch antenna:

$$\frac{W}{h} > 1 \tag{4.1}$$

$$L = \frac{\lambda}{2\sqrt{\varepsilon_{reff}}} \tag{4.2}$$

$$\varepsilon_{reff} = \frac{1}{2}(\varepsilon_r + 1) + \frac{\varepsilon_r - 1}{2\sqrt{1 + \frac{12h}{W}}} \tag{4.3}$$

For a substrate thickness h of 300 μm, relative permittivity ε_r of 6.78 for SiC, and choosing W = 500 μm, the length L becomes 720 μm.

To create the patch antenna I spin-coated the wafer with a 450-nm bi-layer of copolymer/PMMA and used electron-beam lithography to assign the desired antenna dimensions to the Schottky contact. After developing the resist bi-layer, I sputter-deposited 60 nm of Ti and used a liftoff process to remove the unwanted portions of the Ti film. I then coated the laser-metallized Ohmic contacts with a 30-nm layer of gold to facilitate wire bonding. Finally the wafer was attached to an Al_2O_3 chip carrier with conductive epoxy to electrically connect the Ohmic contacts to the chip carrier, and gold wires were ultrasonically bonded to the Schottky contacts.

4.2.2 Device Measurement Results

To confirm the success of the Schottky contact deposition, I measured I-V curves for the diodes. Since the rectified signal amplitude is proportional to the second derivative of the I-V curve [31], it is important to have a strongly nonlinear curve. Figure 4-5 shows a typical I-V curve for the diodes.

I measured the detection capability of the device by illuminating it with a 92.5-GHz Gunn oscillator modulated at 3 kHz. Because the patch antenna favors certain linear polarization states and the output of the Gunn oscillator was linearly polarized, I measured the response of the device as a function of input polarization. The diode was biased at 820 mV and the rectified signal was observed on a lock-in amplifier. Figure 4-6 shows the measured polarization response of the antenna-coupled diode, which exhibits the cosine-squared behavior of a linearly polarized antenna (the trend line in Figure 4-6 is of the form $\cos^2 x$). This demonstrates the functionality of the patch antenna and the ability of the diode to rectify millimeter-wave radiation.

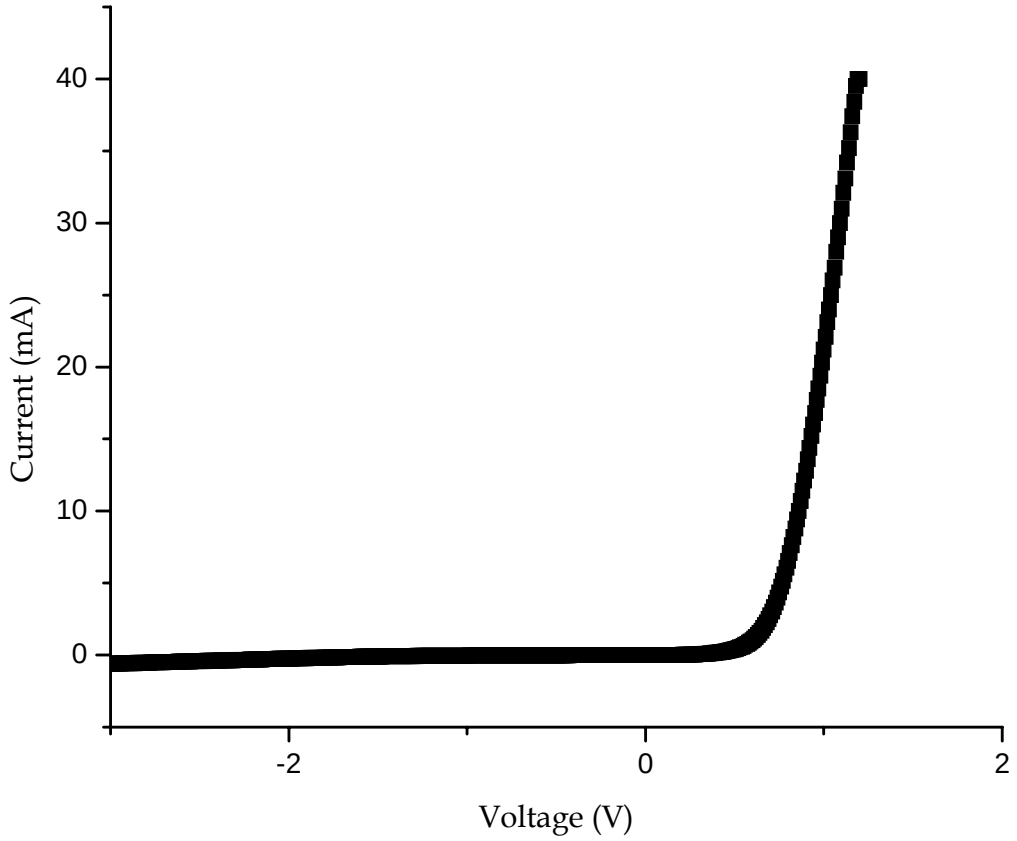

Figure 4-5: I-V curve for SiC Schottky diode

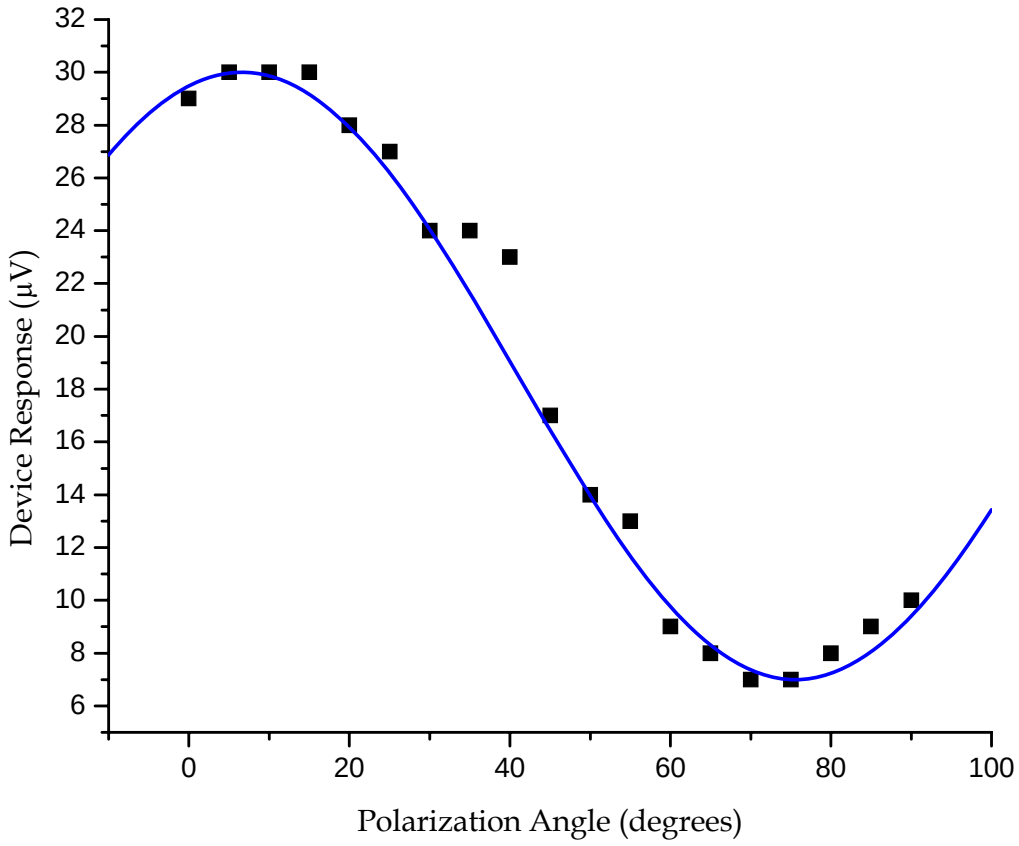

Figure 4-6: Polarization response of SiC Schottky diode at 94 GHz

The diode also acts as a frequency converter for millimeter waves. To show this, I illuminated the device with two 92.5-GHz Gunn oscillators, one a fixed frequency source and the other a mechanically tunable source. The diode was biased at 420 mV and placed inside a copper box to shield the antenna from other

sources of radiation. A small hole in the copper box allowed the radiation from the two sources to illuminate the device.

With the frequencies of the two sources slightly offset, the diode generated a frequency equal to the difference between the frequencies of both sources. I observed this difference frequency on a spectrum analyzer. Figure 4-7 shows a difference frequency of 240 MHz.

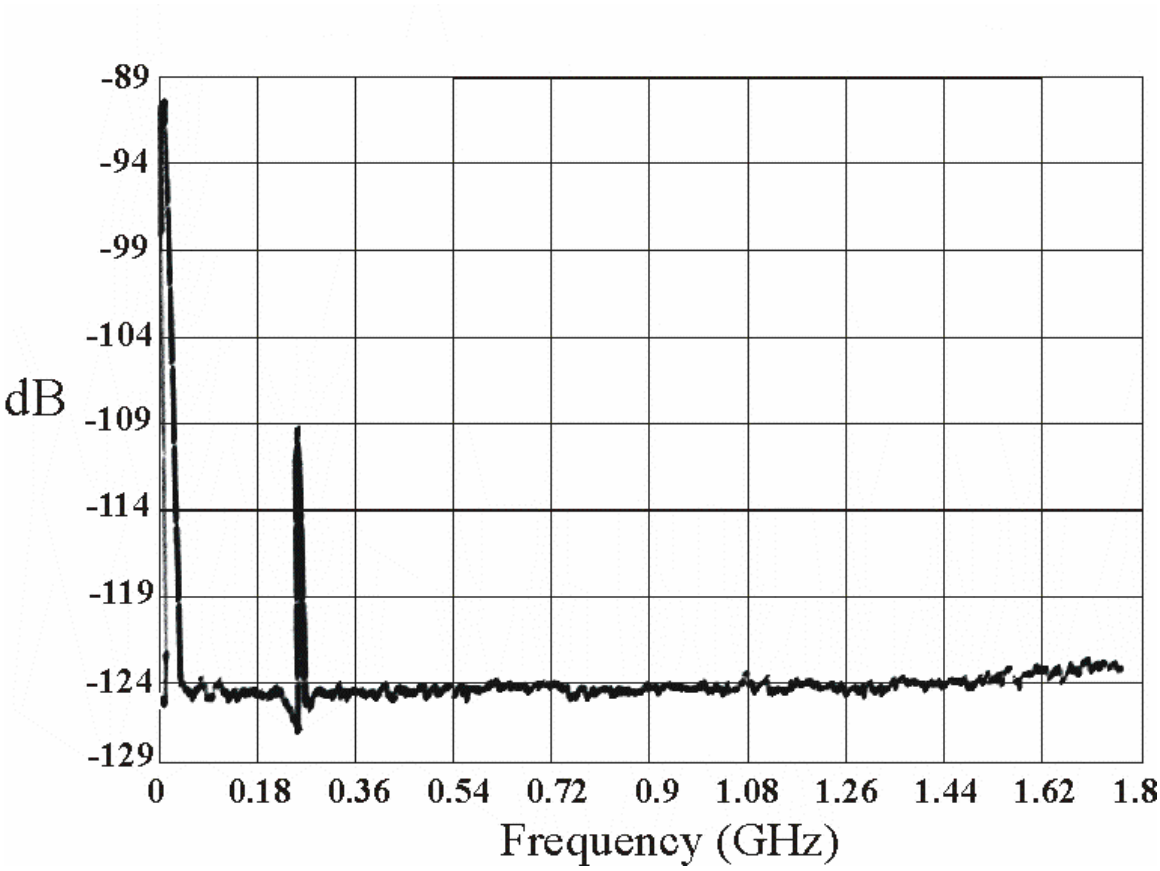

Figure 4-7: Frequency mixing response of SiC Schottky diode

4.3 Millimeter Wave Antenna Modeling

The antennas in this chapter were designed using antenna equations that are normally used for lower frequencies. To develop more useful antennas, simulations were performed using HFSS. Because of their large bandwidths, square spiral and bow tie antennas were investigated. To model these antennas, I drew them using rectangles and Boolean operations. The antennas were placed on Si substrates, and surrounded by an air box.

Figure 4-8 shows a millimeter-wave square spiral antenna on a Si substrate. The antenna line width was 100 μm, the substrate thickness was 1 mm, and the air box dimensions were 3.2 mm x 3.2 mm x 2 mm. A lumped port was assigned at the feed point of the antenna and given an impedance of 50 Ω. Figure 4-9 and Figure 4-10 show the results of a fast frequency sweep from 70 - 180 GHz: the real and imaginary impedance of the antenna and the VSWR.

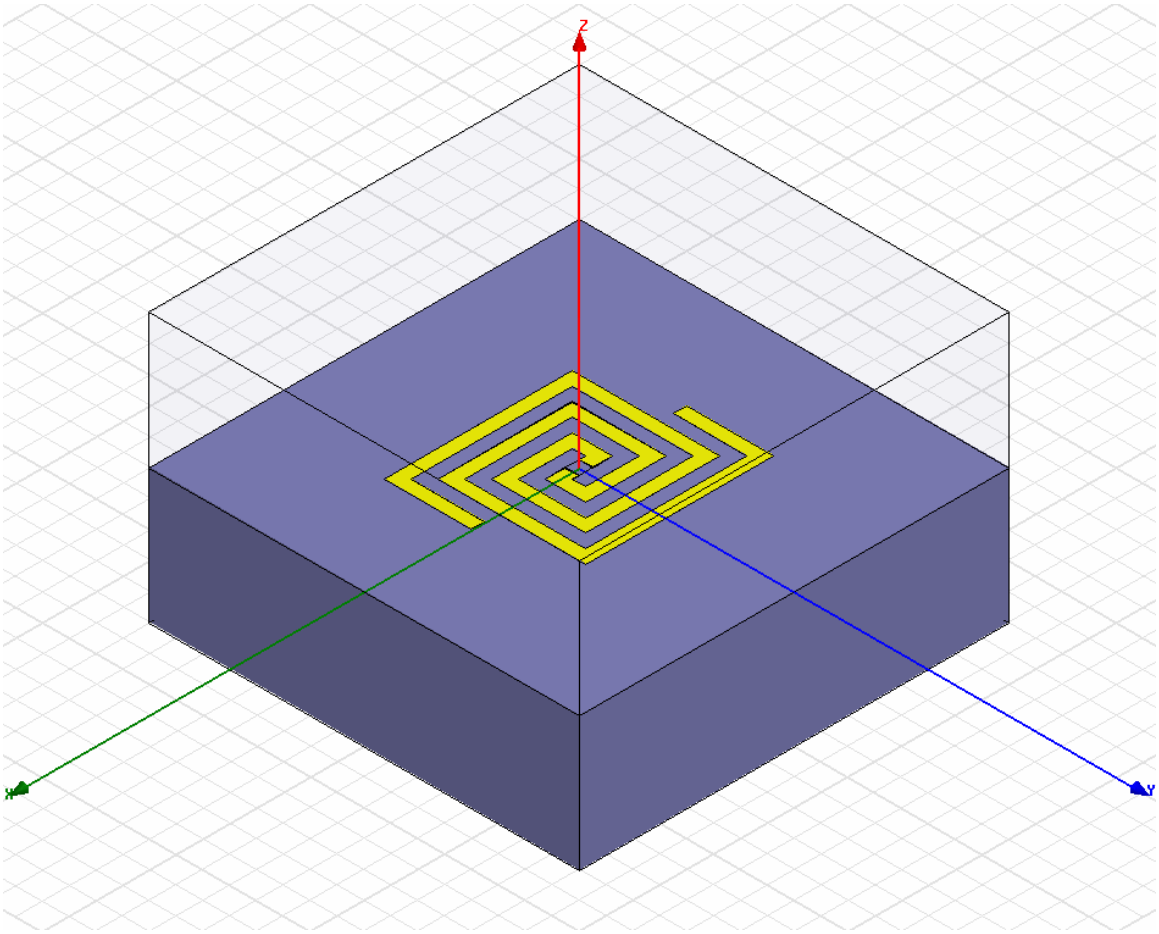

Figure 4-8: HFSS model drawing of a millimeter-wave square spiral antenna on a Si substrate

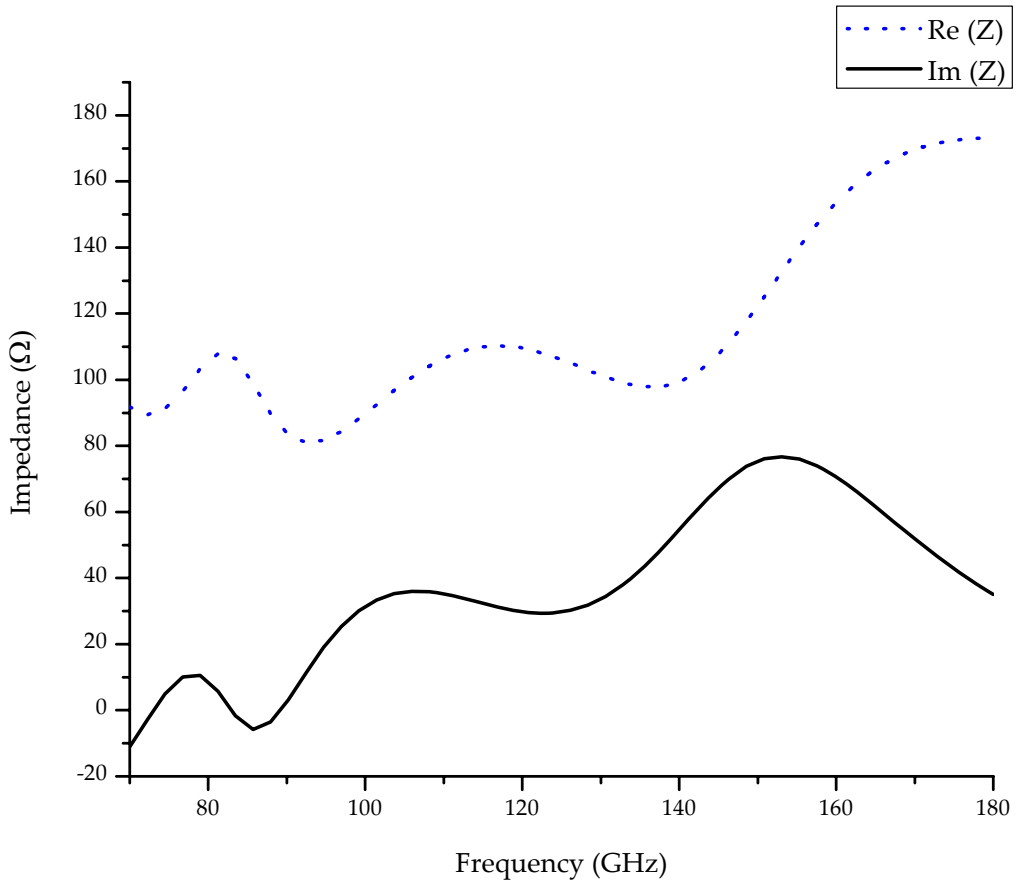

Figure 4-9: HFSS model results showing real and imaginary impedance for millimeter-wave square spiral antenna from 70 - 180 GHz

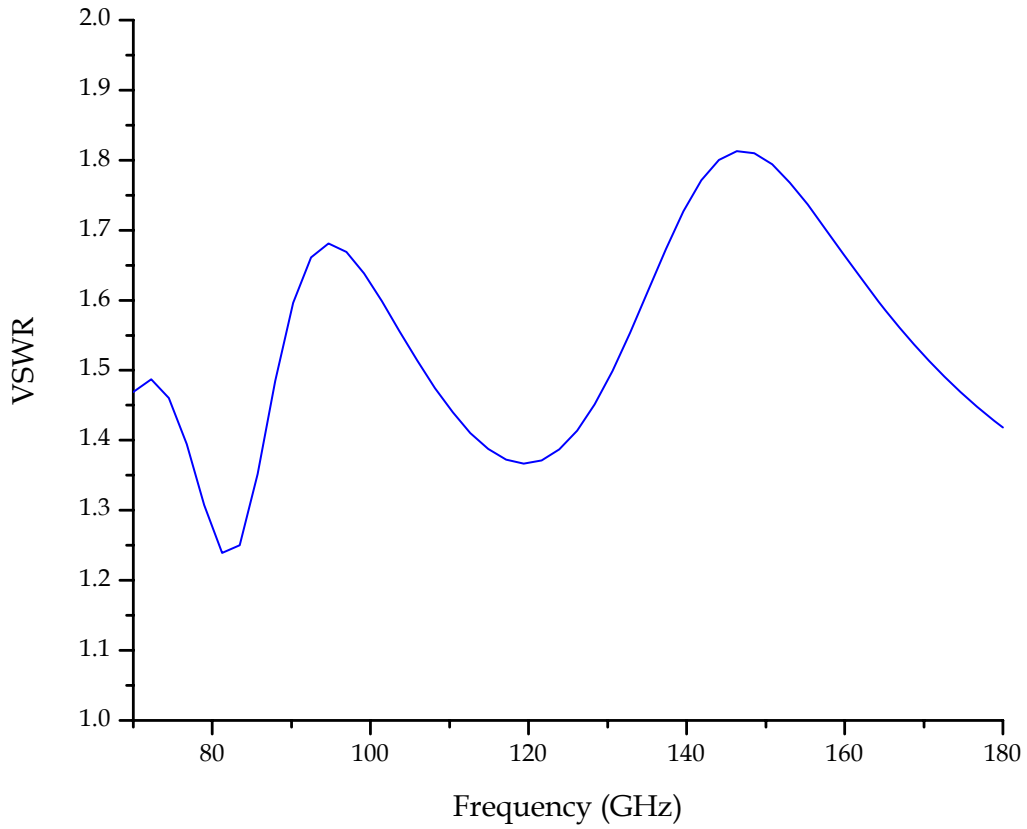

Figure 4-10: HFSS model results showing VSWR for millimeter-wave square spiral antenna from 70 - 180 GHz

Figure 4-11 shows a bow tie antenna designed for millimeter-wave operation. The flare angle was 30°, the length of the antenna was 2 mm, the substrate thickness was 1 mm, and the air box dimensions were 3 mm x 3 mm x 2 mm. As with the square spiral model, a lumped port was assigned at the feed point of the

antenna and given an impedance of 50 Ω. Figure 4-12 and Figure 4-13 show the results of a fast frequency sweep from 80 - 140 GHz.: the real and imaginary impedance and the VSWR, respectively.

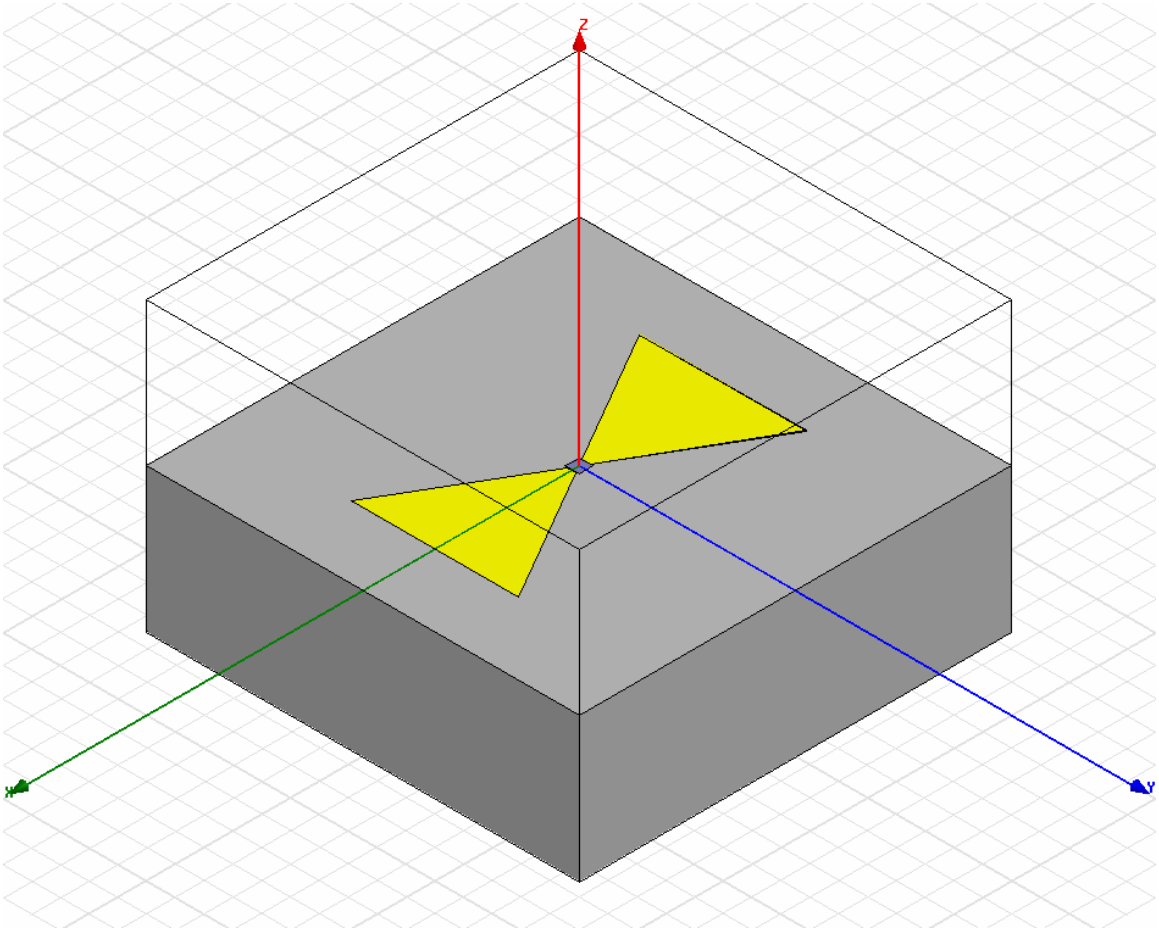

Figure 4-11: HFSS model drawing of a millimeter-wave bow tie antenna on a Si substrate

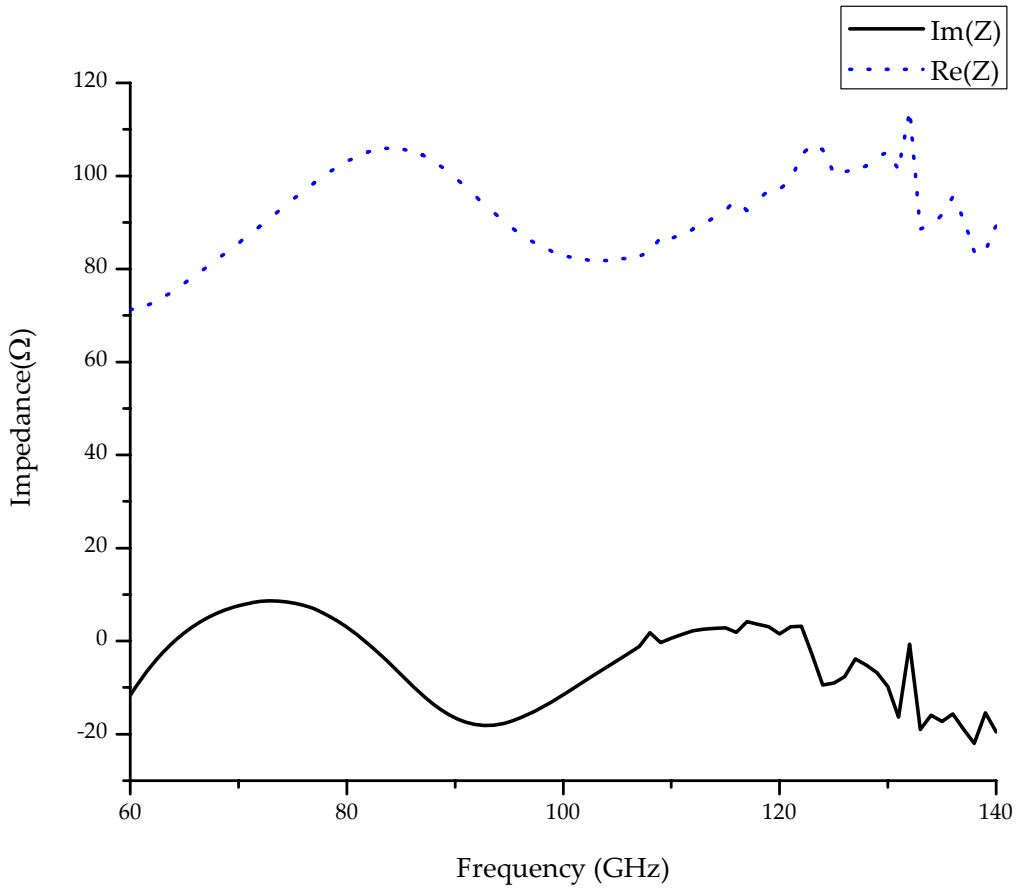

Figure 4-12: HFSS model results showing real and imaginary impedance for millimeter-wave bow tie antenna from 60 - 140 GHz

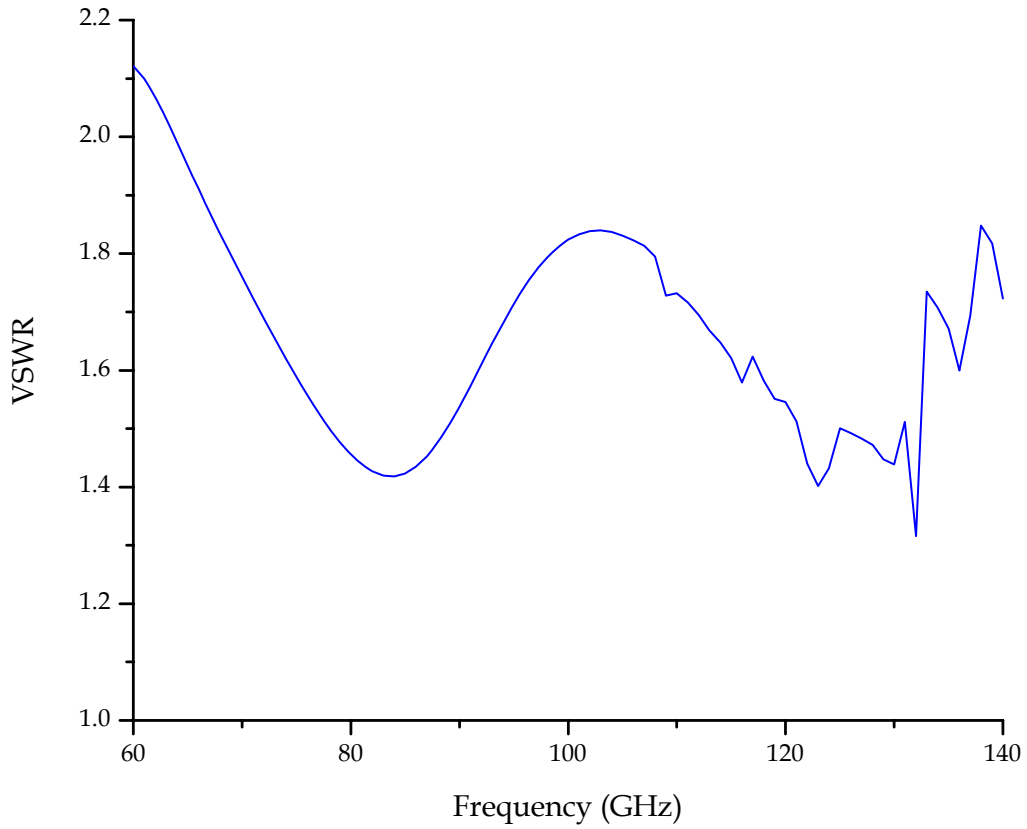

Figure 4-13: HFSS model results showing VSWR for millimeter-wave bow tie antenna from 60 - 140 GHz

Both of these designs show relatively good behavior in the frequency region of interest: the imaginary part of the impedance is close to zero and the VSWR is less than two (VSWR of two corresponds to a reflected power loss of about 10%, while VSWR of six corresponds to a reflected power loss of 50%). But one of the

important issues in coupling an antenna to a detector is the impedance matching. When the detector is a bolometer, the impedance will be very low, on the order of a few ohms. A diode, on the other hand, can have very high impedance, ranging from 1 kΩ to several orders of magnitude higher.

Given the impedance of an antenna, the following plots show the effect of a mismatched load. Figure 4-14 shows the VSWR for a millimeter-wave square spiral antenna versus the detector impedance, and Figure 4-15 shows the VSWR for a millimeter-wave bow tie antenna. In both cases, across the bandwidth of interest the impedance mismatch becomes a great obstacle to device performance. A detector with an impedance of 500 Ω will have a 50% reflected power loss at 94 GHz when coupled to the square spiral antenna. The same detector would do slightly better with a bow tie antenna, losing only 36% of the power. But an antenna designed to give a higher feed-point impedance would certainly improve these curves.

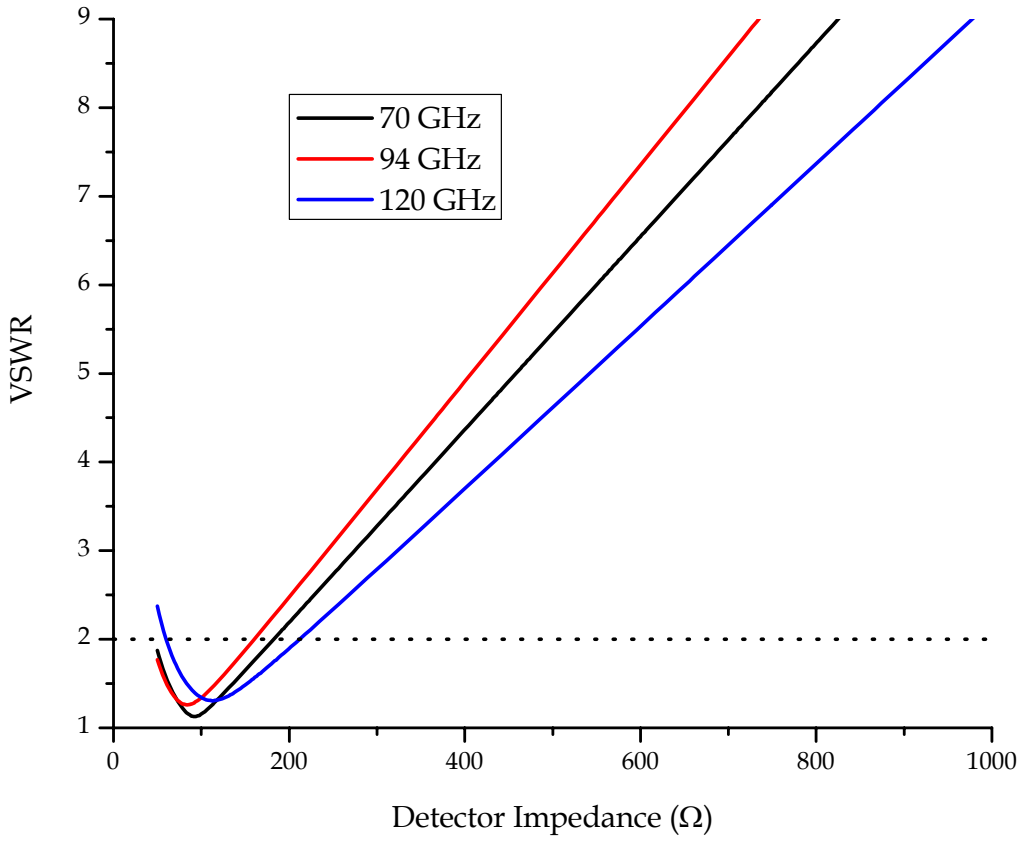

Figure 4-14: HFSS results showing the effect of detector impedance mismatch with a millimeter-wave square spiral antenna

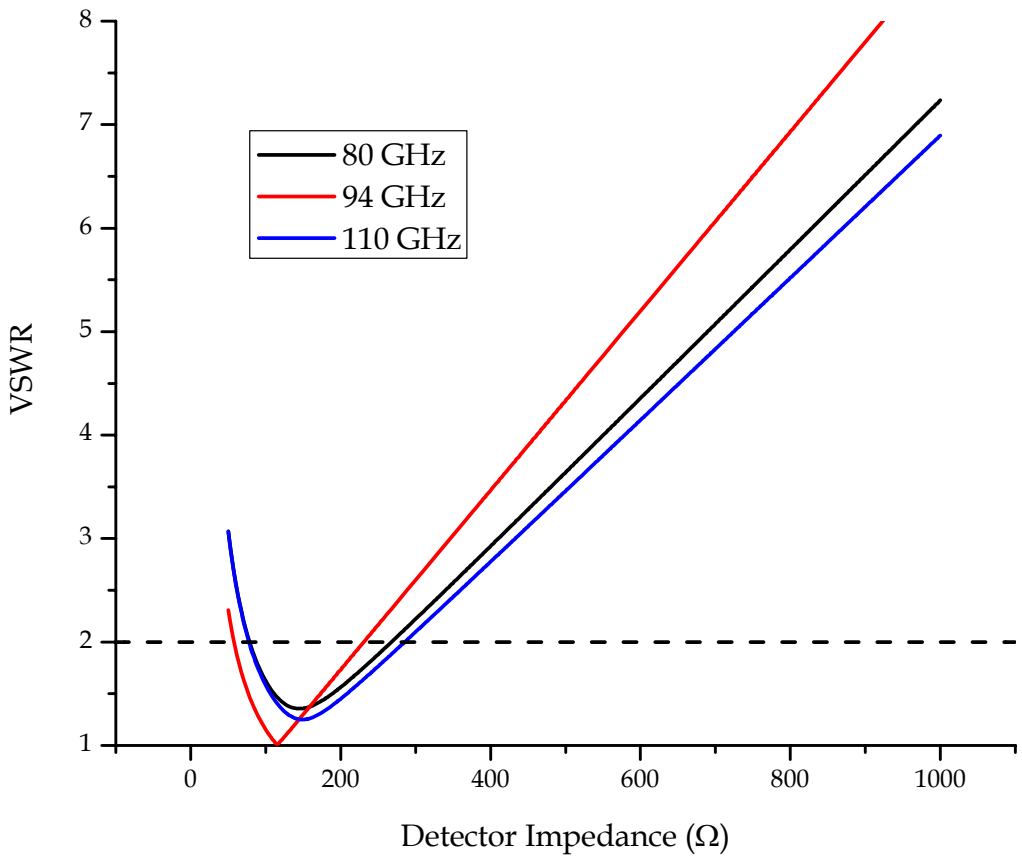

Figure 4-15: HFSS results showing the effect of detector impedance mismatch with a millimeter-wave bow tie antenna

4.4 Toward an Infrared Schottky Diode

The strong nonlinearity of the Schottky diode's I-V curve indicates a large responsivity when the device is biased correctly. After successfully developing a Schottky diode for millimeter-wave rectification, I began to investigate the possibility of a Schottky diode for infrared frequency rectification. In this section I will discuss some of the issues related to the design and fabrication of an infrared Schottky diode.

The physical attributes of a diode determine its cutoff frequency, above which the device response begins to rapidly decrease. This cutoff frequency depends on the junction capacitance (C_j) and series resistance (R_s) of the diode:

$$f_c = \frac{1}{2\pi R_s C_j} \qquad 4.4$$

Reducing the series resistance or the junction capacitance will increase the diode cutoff frequency. The patch antenna used as the Schottky contact for the SiC Schottky diode in section 4.2 would have had a higher cutoff frequency and

hence a better response if a smaller area of the patch metal had formed the Schottky contact, i.e. if the Schottky contact had been formed through a small opening in a passivation layer on the SiC surface. This could have greatly reduced the junction capacitance, which could be roughly calculated from the expression for a parallel plate capacitance:

$$C_j = \varepsilon_0 \, \varepsilon_r \frac{W \, L}{h} \tag{4.5}$$

Given the dimensions of the device, this was about 100 x 10^{-15} Farads. Of course, by decreasing the physical size of the Schottky contact, one would also increase the series resistance of the diode by limiting the current path. Doping levels and material properties also affect the cutoff frequency. More detailed equations are thus necessary to accurately predict cutoff frequency.

The following equations were used to describe diode cutoff frequency [32]:

$$C_j = A \sqrt{\frac{q \, \varepsilon \, N_{d1}}{2 V_{bi}}} \tag{4.6}$$

$$R_s = \frac{x_1 - w_0}{A}\rho_1 + \frac{\rho_2}{A}\left(x_2 + \frac{\sqrt{A}}{2}\right) \tag{4.7}$$

$$w_0 = \sqrt{\frac{2\varepsilon V_{bi}}{q N_{d1}}} \tag{4.8}$$

$$\rho_1 = \frac{1}{q\mu_e N_{d1}} \tag{4.9}$$

$$\rho_2 = \frac{1}{q\mu_e N_{d2}} \tag{4.10}$$

$$V_{bi} = \phi_B - \frac{kT}{q}\log_e\left(\frac{N_c}{N_{d1}}\right) \tag{4.11}$$

where A is the area of the Schottky contact, q is the charge of an electron, ε is the dielectric constant of the material, x_1 is the thickness of the heavily-doped epilayer region, N_{d1} is the dopant concentration of the epilayer region, x_2 is the thickness of the substrate, N_{d2} is the dopant concentration of the n-type substrate, μ_e is the electron mobility of the material, ϕ_B is the Schottky barrier height, ρ_1 and

ρ_2 are the epilayer and substrate resistivities, w_0 is the depletion width at zero bias, V_{bi} is the built-in potential for the metal-semiconductor system, k is Boltzmann's constant, T is the operating temperature of the device, and N_c is the effective density of states for electrons in the conduction band.

Of these 16 variable parameters, three are constants (q, k, and T), four are dependent on other parameters (V_{bi}, w_0, ρ_1 and ρ_2), and the remaining nine are based on the choice and structure of the semiconductor material and Schottky contact (N_c, N_{d1}, N_{d2}, ϕ_B, μ_e, ε, x_1, x_2, and A). Device performance is limited by the available materials, their possible doping concentrations and other intrinsic properties, and the dimensions of the Schottky contact.

The following series of plots demonstrate the effect of these parameters on cutoff frequency. A GaAs substrate is chosen over Si because of its higher electron mobility. Figure 4-16 shows the cutoff frequency of a device as a function of Schottky contact width for several different Schottky barrier heights. From these equations, it is necessary to choose a Schottky contact metal with a barrier height greater than 0.45 V and use a contact width smaller than 10 μm in order to realize a device cutoff frequency greater than 30 THz (roughly the center of the 8 - 12

μm LWIR band). In this plot, the epilayer thickness was fixed at 880 nm, the substrate thickness was 500 nm, the epilayer doping concentration was 10^{15} cm^{-3}, and the substrate doping concentration was 10^{19} cm^{-3}.

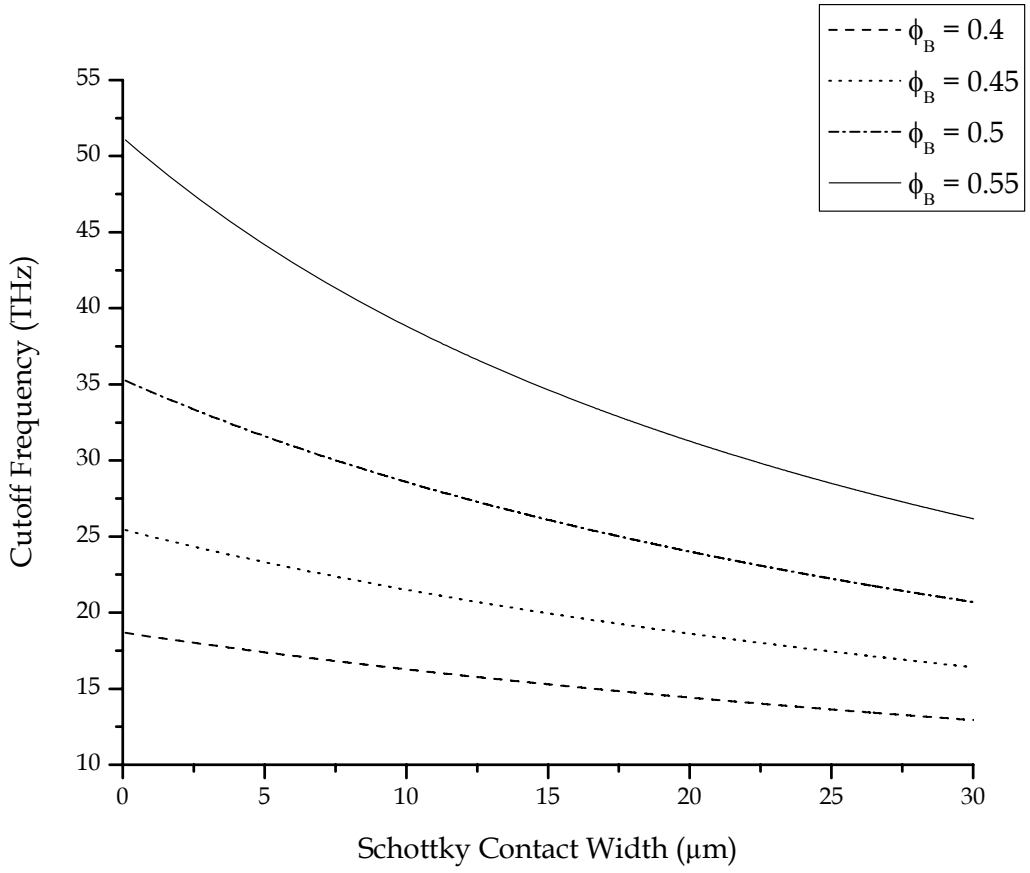

Figure 4-16: Schottky diode cutoff frequency vs. Schottky contact area for several barrier heights

Figure 4-17 and Figure 4-18 show the cutoff frequency as a function of substrate and epilayer doping concentrations, assuming a Schottky barrier height of 0.5 V, substrate thickness of 500 nm, epilayer thickness of 880 nm, and using contact widths of 1, 2, 5 and 10 μm. The doping level should be greater than 10^{19} cm^{-3} in the substrate and as low as possible in the epilayer, but less than 10^{15} cm^{-3}. Note that epilayer doping concentration doesn't depend as strongly on Schottky contact area as substrate doping concentration does.

In Figure 4-19 and Figure 4-20 the cutoff frequency is shown as a function of substrate and epilayer thickness. Both thicknesses should be less than 1 μm for a cutoff frequency above 30 THz. In these plots the epilayer doping concentration was 10^{15} cm^{-3}, the substrate doping concentration was 10^{19} cm^{-3}, the Schottky barrier height was 0.5 V, and Schottky contact widths were 1, 2, 5, and 10 μm.

These plots help in designing a device for infrared operation, but the validity of the equations at higher frequencies is questionable. The model doesn't account for carrier inertia, skin effect, or displacement current.

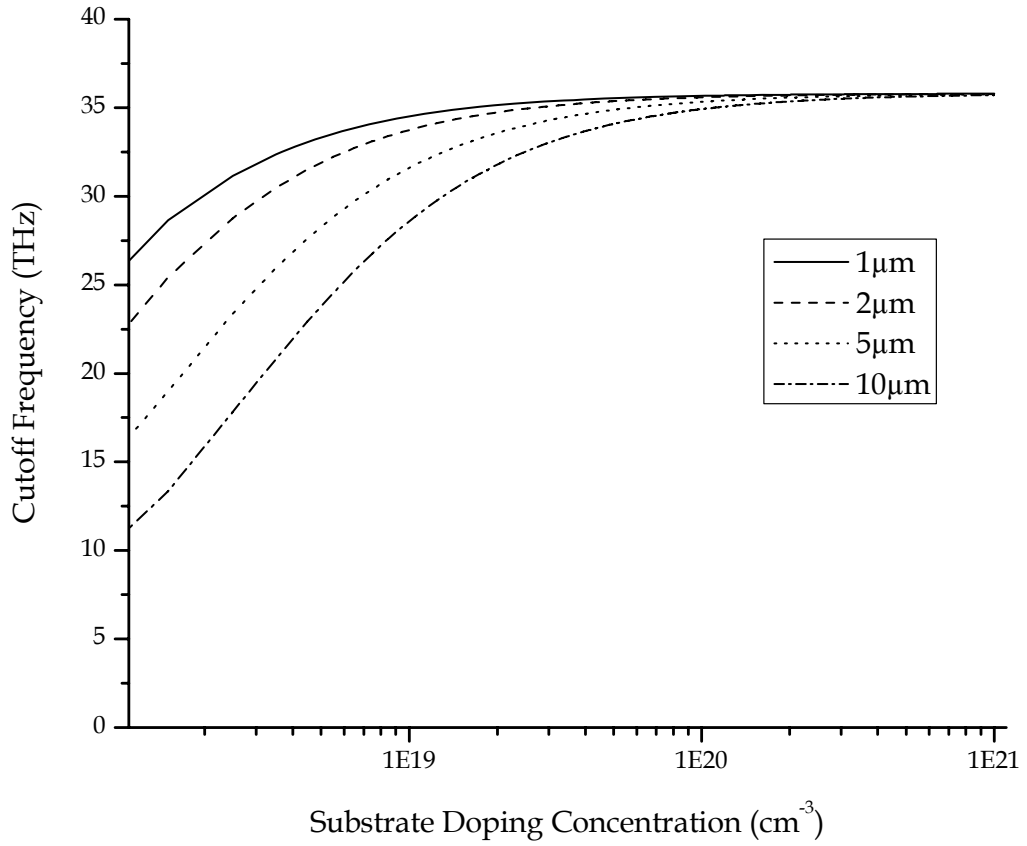

Figure 4-17: Schottky diode cutoff frequency vs. substrate doping concentration for several Schottky contact widths

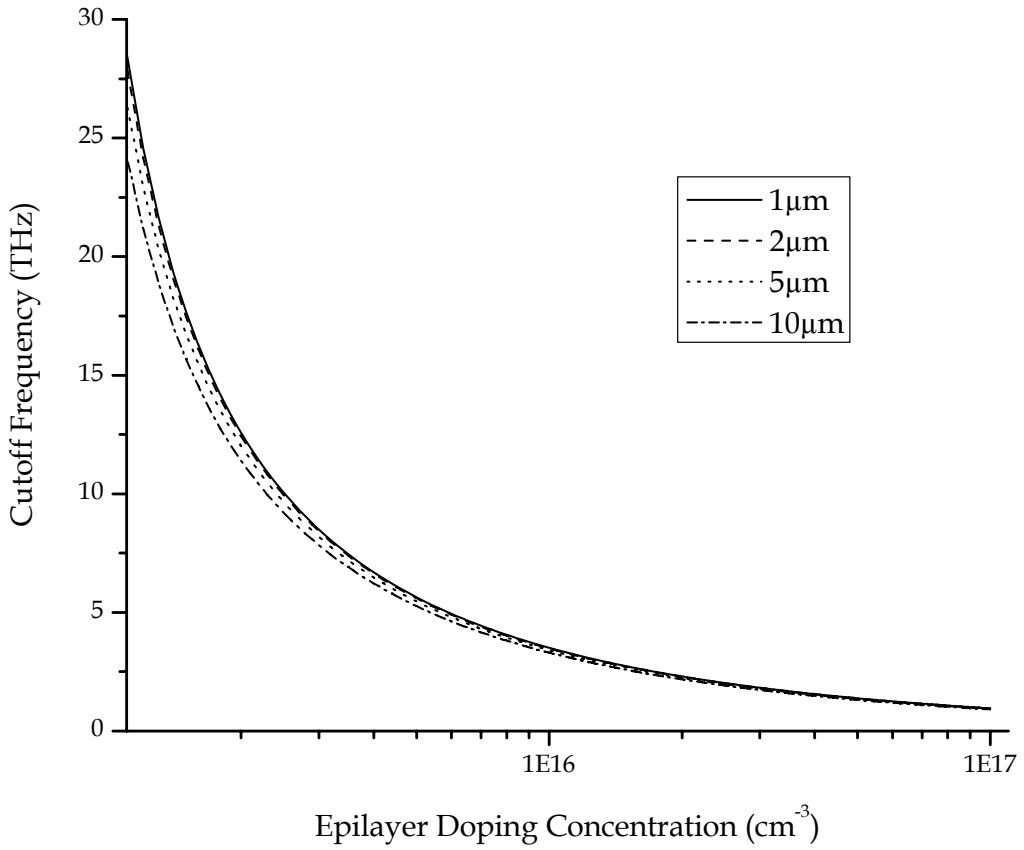

Figure 4-18: Schottky diode cutoff frequency vs. epilayer doping concentration for several Schottky contact widths

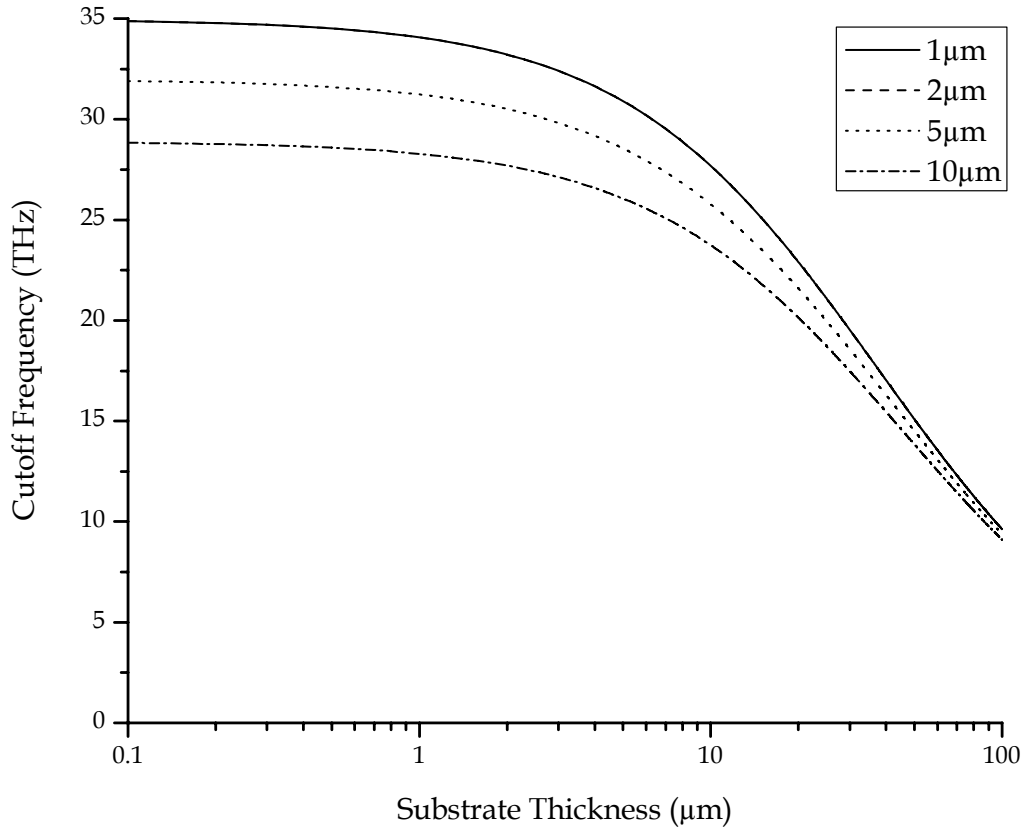

Figure 4-19: Schottky diode cutoff frequency vs. substrate thickness for several Schottky contact widths

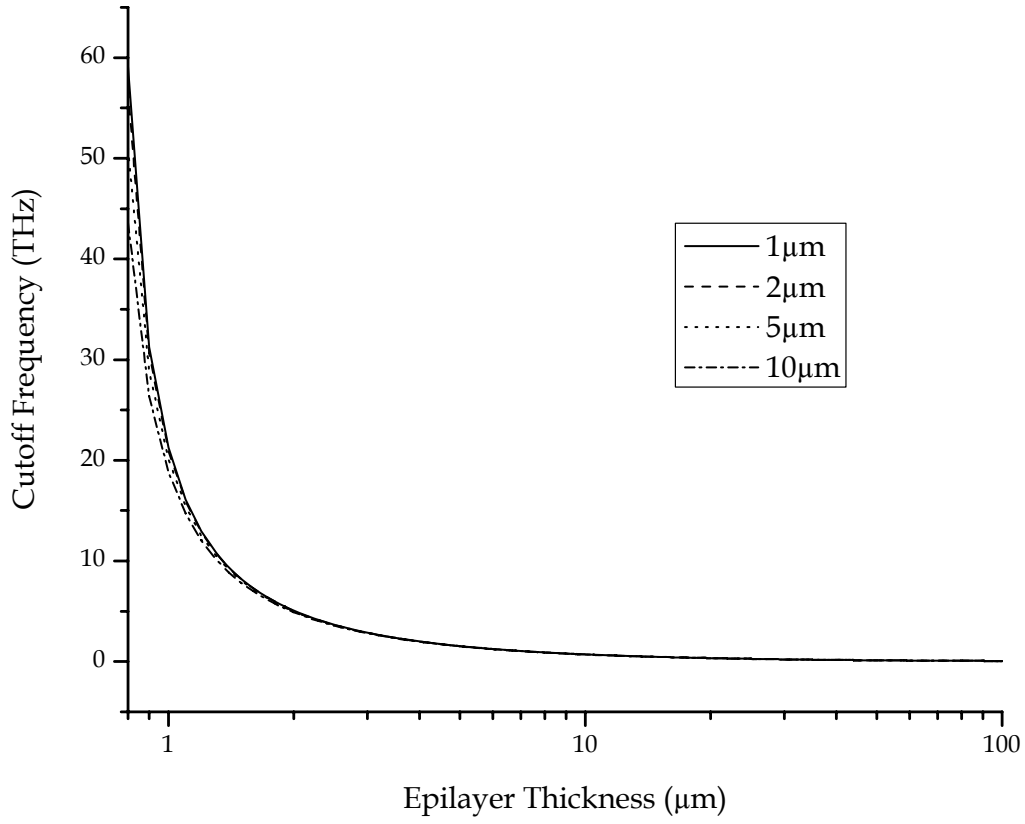

Figure 4-20: Schottky diode cutoff frequency vs. epilayer thickness for several Schottky contact widths

CHAPTER 5

IMPROVING THERMAL ISOLATION

5.1 The Importance of Thermal Isolation for Bolometric Devices

The voltage responsivity of a bolometer is usually expressed as

$$\Re_v = \frac{i_{bias} R \alpha \eta}{G\sqrt{1+\omega^2 \tau^2}} \qquad 5.1$$

where i_{bias} is the bias current applied through the bolometer, R is the device resistance, α is its temperature coefficient of resistance (TCR), G is its thermal conductance, ω is the angular frequency, and τ is the thermal constant ($\tau = C/G$; C is the heat capacity of the bolometer) [33].

Because responsivity is directly proportional to TCR, the choice of bolometric material is important. But since this number varies by only a few percent in most

readily available materials, the inverse proportionality of thermal conductivity, *G*, has a greater effect on responsivity.

A faster time constant allows the device to be used in a wider range of applications. The time constant depends on the physical size of the bolometer: a smaller bolometer has a faster time constant. But as the bolometer gets smaller, its collection area also gets smaller, making it less effective as a sensor. To increase the collection area of the bolometer without increasing its physical size, one can couple the bolometer to an antenna. If the antenna is designed to resonate at the desired frequency, radiation can be directed into the bolometer and responsivity will increase. The choice of antenna determines the resonant frequency, bandwidth, and polarization of the device. Ground planes and arrays of antennas can also be used to increase the response of a bolometer.

Antenna-coupled micro-bolometers are generally monolithic structures that can be fabricated using standard integrated circuit manufacturing techniques, such as optical lithography and thin film deposition. The devices are operated at room temperature and have low power requirements. The antenna design used in this chapter is a square spiral, which has a large bandwidth and no

polarization dependence. The antenna structure is written using electron beam lithography, with minimum feature size of 450 nm.

Section 5.2 describes my efforts to increase thermal isolation of the bolometer (decreasing the thermal conductance of the device and thereby increasing responsivity). I developed a process to fabricate antenna-coupled Ni bolometers on silicon nitride membranes, and measured their response under vacuum. This response was compared to identical devices on Si substrates. Since the membrane itself has a thermal conductance associated with it, a thinner the membrane should yield a better device. I developed a process to eliminate the membrane entirely by suspending the device in air. This process is discussed in section 5.3.

5.2 Antenna-Coupled Bolometers on Si_3N_4 Membranes

5.2.1 Device Fabrication

Antenna-coupled devices were fabricated on a 400-nm LPCVD Si_3N_4 layer, which was deposited on a 3-μm thermally-grown SiO_2 layer on a Si substrate [34]. Square spiral antennas were written in positive-tone electron-beam resist bi-layer (ZEP 520A-7 on PMGI SF-7) with a Leica EBPG 5000+ electron-beam lithography system. The use of PMGI (polydimethylglutarimide) as a lift-off resist layer underneath the ZEP imaging resist layer allowed control of undercut dimensions. Both resist layers were spun onto the substrate at 3000 rpm for 80 seconds, corresponding to thicknesses of 450 nm for PMGI and 300 nm for ZEP. Each layer was baked on a hot plate at 180°C for 3 minutes (PMGI), and 4 minutes (ZEP). No adhesion promoter was necessary.

I exposed the resist bi-layer with a dose of 120 $\mu C/cm^2$, with the e-beam operating at 50 kV. The ZEP layer was then developed for 90 seconds in xylene, and the PMGI layer was developed for 20 seconds in tetramethyl ammonium hydroxide (TMAH) developer (2.3%). The PMGI developer was perhaps too

aggressive, and could be diluted in de-ionized water to give longer, more repeatable development times, but I had adequate device uniformity with this method. It was not necessary to descum the wafer before metal deposition.

Ni was deposited in a thickness of 150 nm, via DC magnetron-sputtering onto the substrate. To lift off the metal and remove the resist bi-layer, I placed the wafer first in methylene chloride for 30 minutes. This removed the layer of ZEP resist, as well as any Ni that sat on the resist layer. Then I placed the wafer for 30 minutes in EBR-PG, the edge-bead remover sold by MicroChem, which consists mainly of 1,3-dioxolane and propylene glycol monomethyl ether, and removes the PMGI resist layer, leaving only the Ni antenna-coupled micro-bolometers.

Membranes were created underneath the antenna-coupled devices by coating the wafer with positive-tone photo-resist (Shipley S1818) and exposing two rectangles on either side of the antenna. Figure 5-1 shows a schematic drawing of a device on a membrane. Exposure was accomplished with a Karl Suss MJB3 contact aligner. With the photo-resist as a mask, the Si_3N_4 was RIE-etched in CHF_3 plasma. This etch was performed with 50 mTorr CHF_3 at 1000 W RF power

for 2 minutes. Slight over-etching into the SiO_2 layer occurred, but this only helped with the next step.

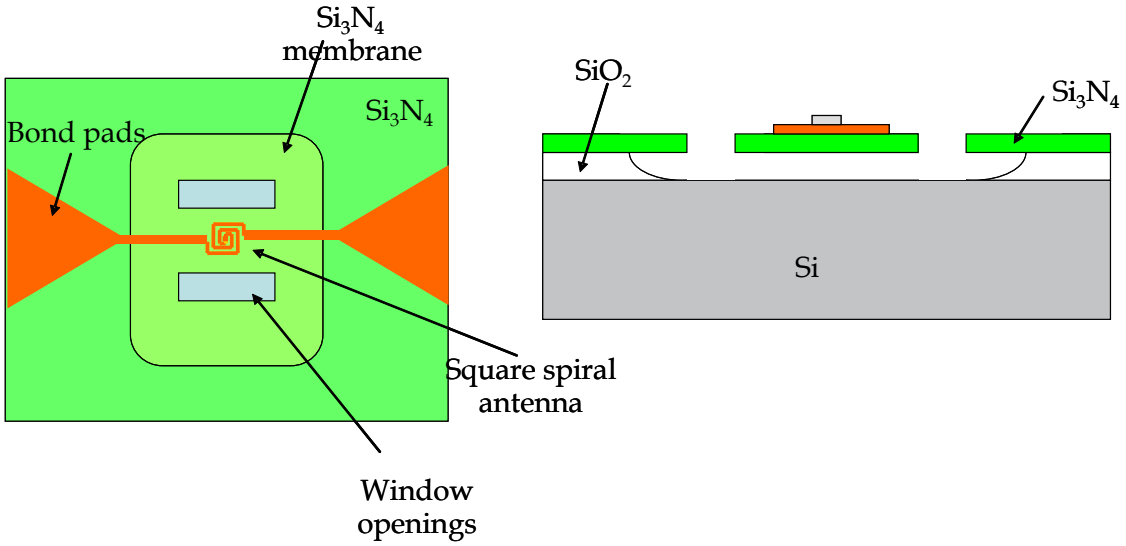

Figure 5-1: Schematic top view and cross section drawings of an antenna-coupled bolometer on a Si_3N_4 membrane

The wet etchant 9:1 BOE (ammonium fluoride: hydrofluoric acid) was then used to etch the SiO_2 underneath the Si_3N_4. The photo-resist provided a sufficient mask for the antenna metal, which would otherwise have been removed by the etchant during the three-hour etch. The isotropic nature of wet etching caused

the SiO_2 directly beneath the antenna-coupled devices to be removed, leaving the devices suspended on the 400-nm layer of Si_3N_4. In the final step, acetone was used to remove the photo-resist mask. This nitride layer was robust enough that critical point drying was not necessary in releasing the devices, due in part to the thickness of the nitride, and also to the deposition method: low pressure chemical vapor deposition (LPCVD) yields a lower-stress film than plasma-enhanced chemical vapor deposition (PECVD). Images of the devices are shown in Figure 5-2.

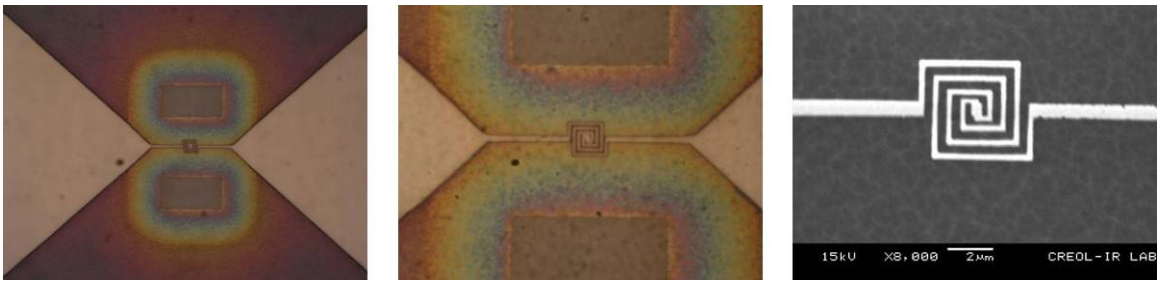

Figure 5-2: Optical and electron-beam microscope images of an antenna-coupled bolometer on a Si_3N_4 membrane

Initial attempts at membrane fabrication relied on e-beam resist for the RIE mask to etch Si_3N_4, and used no mask during the BOE etch [35]. For this reason, Au

and Cr were the only metals used, as they are not removed by hydrofluoric acid. To develop a fabrication process that would allow the use of arbitrary antenna and bolometer materials, I first tried to create the membranes by coating the antenna-coupled micro-bolometers with several hundred nanometers of thermally-evaporated Cr, then masking the Cr with photo-resist, wet-etching windows in the Cr, RIE etching those same windows in the Si_3N_4, wet-etching the SiO_2 in 49% HF, and finally etching away the remaining Cr. This process failed because the Cr was not an adequate mask for HF, and the Cr etchant also etched several candidate antenna metals, such as Ti.

The present approach, using photo-resist as a mask instead of Cr and using BOE instead of straight HF, is a much simpler and more effective process. Bolometer and antenna materials that would normally be removed by HF can now be included in the process. The choice of Ni in this work is due largely to the ease of deposition and Ni's slightly higher TCR (~0.6%, compared to 0.4% in most metals).

5.2.2 Device Measurements

The membrane device was mounted in an evacuated dewar with a ZnSe window, on a three-axis micro-positioner stage. A roughing pump was used to evacuate the dewar to a pressure of 20 mTorr. I applied a bias voltage of 150 mV and observed the signal on a spectrum analyzer and lock-in amplifier after it passed through a 10x amplifier. With the laser test setup described in chapter 3, using the 10.6-μm CO_2 laser line and illuminating the devices from the air side, I measured the response and noise figure of three types of device: Ni square spiral antenna coupled to a Ni bolometer on a substrate of Si_3N_4 (no membrane); the same device on a 400-nm Si_3N_4 membrane in air; and the same device on a 400-nm Si_3N_4 membrane under vacuum. Measured results are shown in Table 5-1.

Knowing the incident power of the laser, the beam spot size, and the effective area of the detector, I calculated responsivity in the following manner:

$$\Re_v = \frac{v_{signal}}{\phi_{\det}} \qquad 5.2$$

where v_{signal} is the output of the detector (in Volts) and $\phi_{\det}$ is the laser flux on the detector (in Watts). Laser flux was determined by measuring the beam power at the focus and multiplying it by the ratio of the device area to the beam spot size. The device area was determined by the 2D-scan deconvolution method discussed in chapter 3. In this case a device area of 1.25×10^{-11} m^2 was used. With the measured noise figure, v_n, I also calculated normalized detectivity (D*), a commonly used figure of merit for detectors. This is used to compare the sensitivity of detectors of different size and electrical bandwidth:

$$D^* = \frac{\Re_v}{v_n}\sqrt{A_{\det}\Delta f} \qquad 5.3$$

Here $A_{\det}$ is the area of the detector and Δf is the electrical bandwidth. The thermal isolation technique succeeded in increasing the responsivity and D* of the sensor by two orders of magnitude. Creating the membrane had a large effect on the responsivity, increasing it by a factor of 47.6; operating the membrane under vacuum further reduced thermal loss paths and increased responsivity by an additional factor of 3.44.

Table 5-1: Measured results for Ni antennas coupled to Ni bolometers at 10.6 μm, demonstrating increased responsivity with improved thermal isolation of the device from the substrate using a Si_3N_4 membrane

Device	Signal (mV)	Noise (nV/√Hz)	Power (μW)	ℜ (V/W)	D* (cm √Hz/W)
No membrane	0.3	6.12	30	10.1	5.69×10^5
Membrane, no vacuum	1.03	5.7	2.14	482	2.89×10^7
Membrane with vacuum	3.54	5.7	2.14	1656	1.03×10^8

5.3 Thermal Isolation Through Air Bridges

5.3.1 Fabrication Process Outline

To achieve greater thermal isolation of the antenna-coupled detectors, I developed a process to suspend the devices in air. The technique involves the use of reflowed PMGI as a sacrificial layer, and critical point drying to release the devices. The fabrication process is outlined here:

1. Write e-beam alignment marks using e-beam lithography process for resist bi-layer (ZEP 520A-7/PMGI SF7).
2. Deposit Ti-Au layer (10 nm - 150 nm) using e-beam evaporation; use lift off process to remove metal and both layers of resist.
3. Write air bridge sacrificial layer using e-beam lithography process for resist bi-layer (ZEP 520A-7/PMGI SF7) with alignment. For different air bridge height above substrate, use different thickness of PMGI resist layer. In this case, I used two coats of PMGI SF7 to reach a PMGI film thickness of 950 nm. The two coats were applied by spinning on the first coat (3000 rpm for 80 seconds), baking the substrate on a hotplate at 180 °C for 30 seconds, spinning on the second coat (3000 rpm for 80 seconds), and then baking the substrate on a hotplate at 180 °C for 5 minutes.
4. After developing both layers of resist, remove ZEP 520A-7 resist using methylene chloride. Reflow the PMGI layer by baking the substrate on a hotplate at 230 °C for 5 minutes. The reflow process gives the antenna lead lines a less-abrupt step from the substrate to the surface of the sacrificial layer.

5. Write antenna-coupled bolometers using e-beam lithography process for resist bi-layer (ZEP 520A-7/950 PMMA A4) with alignment. Development of this resist bi-layer will not affect the PMGI sacrificial layer.
6. Deposit antenna metal using e-beam evaporation. Use Scotch tape to remove antenna metal; use methylene chloride to remove ZEP 520A-7/950 PMMA A4 bi-layer; use EBR-PG to remove PMGI sacrificial layer.
7. Move substrate directly from EBR-PG to acetone bath without letting it dry. Load acetone-covered substrate into critical point dryer and release air-suspended devices.

5.3.2 Critical Point Drying

Critical point drying was used here to prevent damage to the air-suspended devices as they were removed from the solvent bath. Surface tension during the phase transition from liquid to gas can damage the devices, so I applied this technique to by-pass the phase transition. This method is commonly used in biological sample preparation and MEMS applications. The device is immersed

in acetone and placed inside a pressure vessel with an integral water jacket for cooling and heating. The acetone is then flushed out and replaced with liquid CO_2. By flowing hot water around the pressure vessel, one can raise the temperature and pressure beyond the critical point of CO_2 (see phase diagram in Figure 5-3). The pressure is decreased and the now-gaseous CO_2 is vented away while maintaining a constant temperature, and then the vessel is cooled back to room temperature and the device is ready to be removed from the vessel and measured.

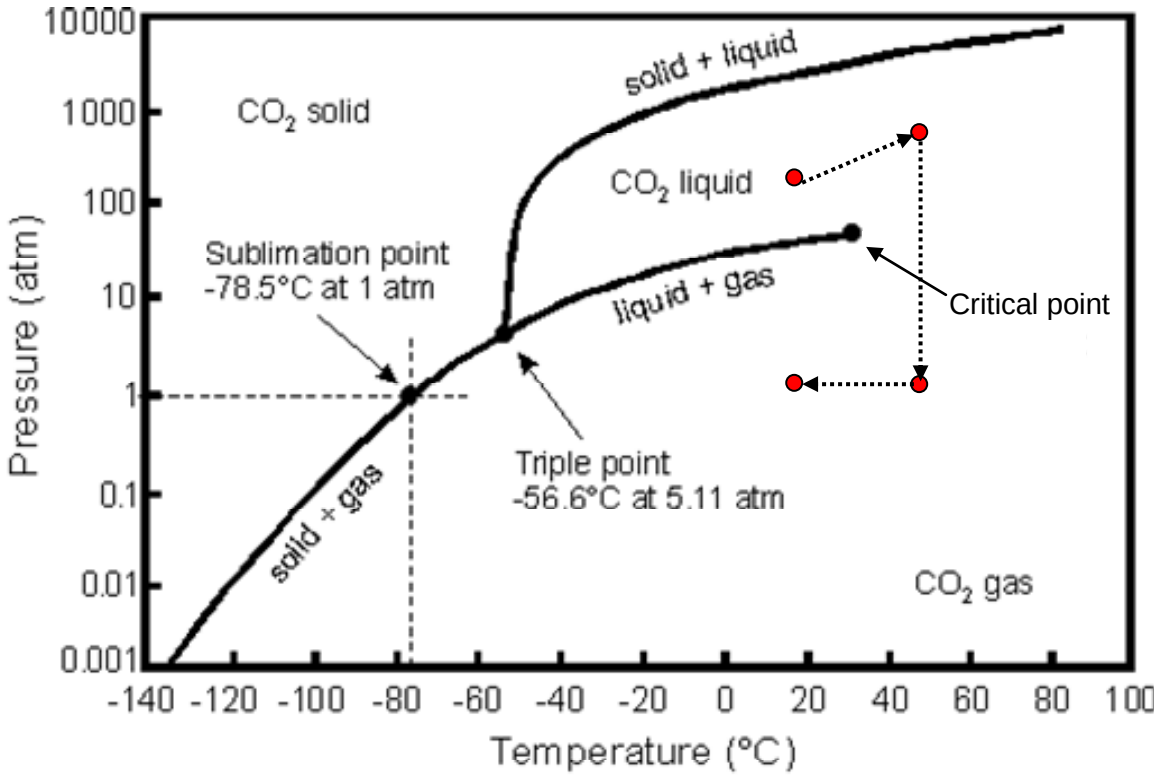

Figure 5-3: Phase diagram for CO_2, demonstrating critical point drying [36]

The following three figures show the effect of stress and tension on the air bridge devices. Figure 5-4 and Figure 5-5 are both examples of unsuccessful release of the device, in which the surface tension of the acetone destroys the device as it goes from liquid to vapor. Figure 5-6 shows a successfully released device, done with critical point drying.

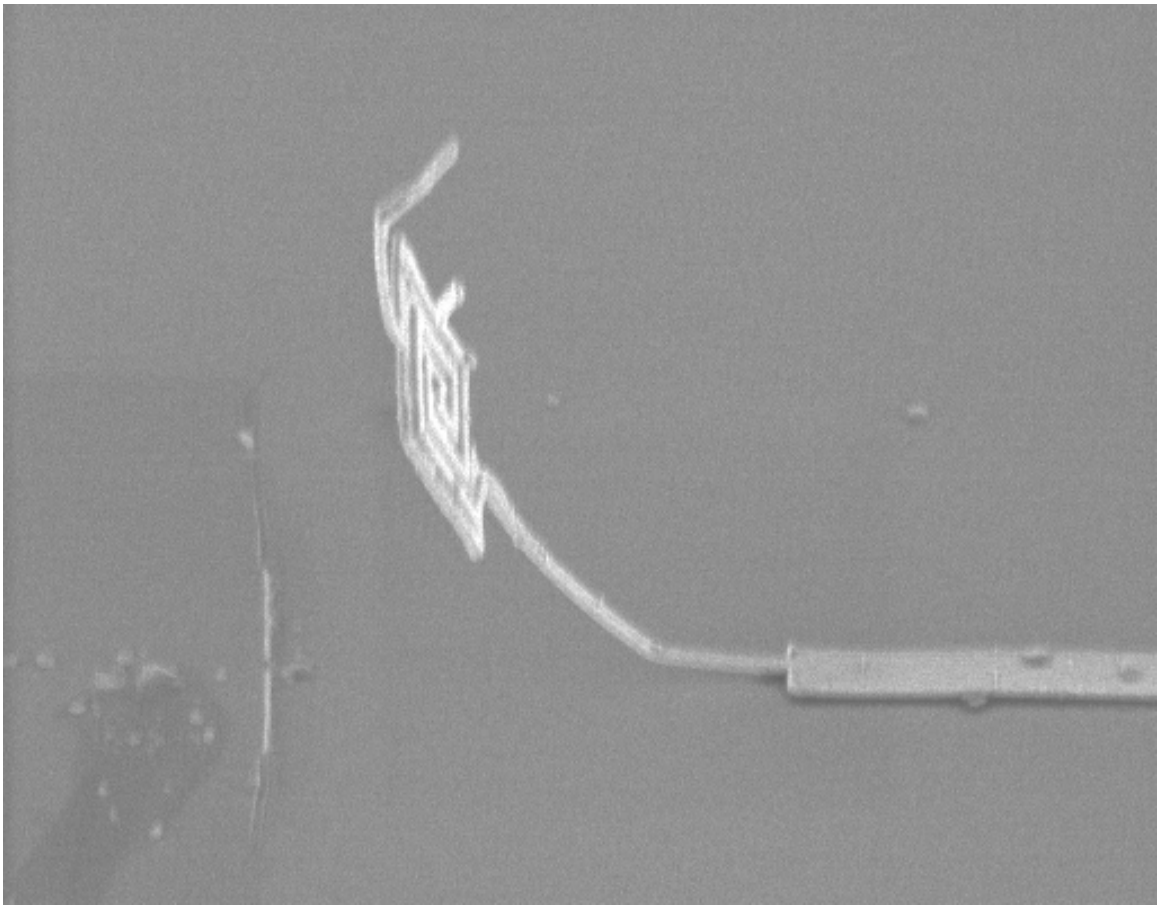

Figure 5-4: SEM image of air bridge square spiral antenna-coupled bolometer with unsuccessful device release

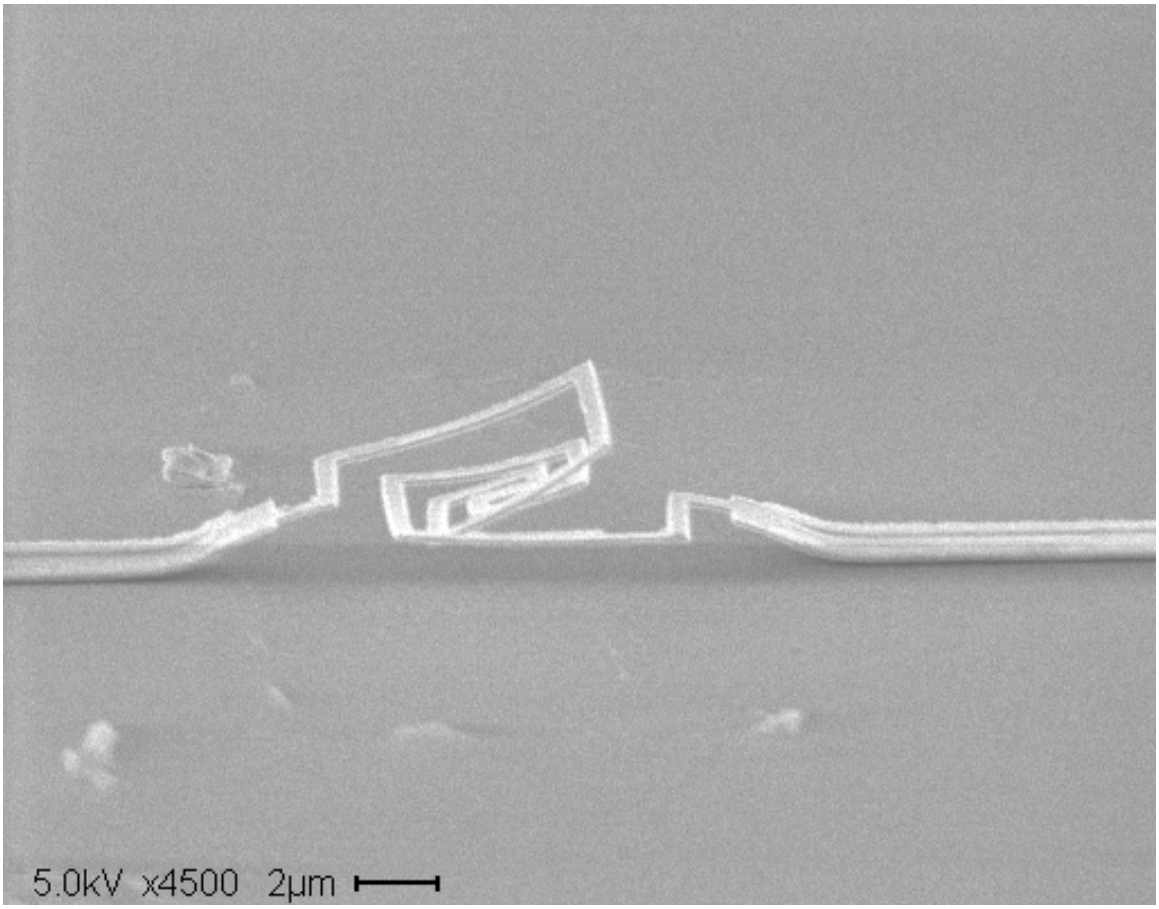

Figure 5-5: SEM image of air bridge square spiral antenna-coupled bolometer with unsuccessful device release

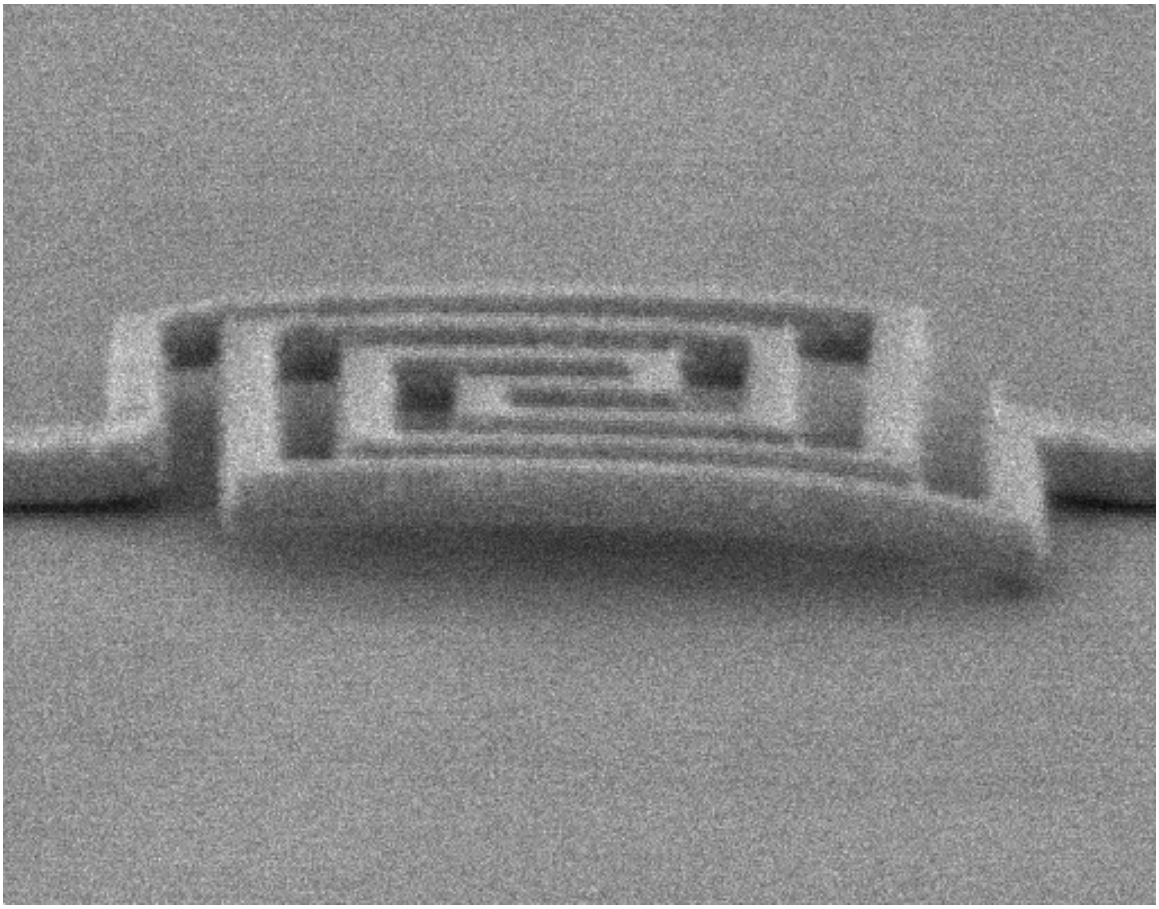

Figure 5-6: SEM image of air bridge square spiral antenna-coupled bolometer with successful device release

CHAPTER 6

OPTIMIZATION OF INFRARED DEVICES

6.1 Antenna Metal Study

6.1.1 Theoretical Issues Relating to Antenna Metal Choice

To choose the best metal for the antenna, one must consider the thermal, electrical and optical properties of the metal. The antenna metal should be a good electrical conductor at DC and infrared frequencies, and it should have low thermal conductivity to minimize thermal losses. From a practical standpoint, the deposition process of the metal should also be considered, as some metals are more difficult to deposit in a uniform, repeatable manner. In this study, four metals have been chosen: aluminum, gold, nickel, and titanium. These metals are all readily available and can be deposited reliably by e-beam evaporation. The technical details for deposition are described in chapter 2 of this dissertation.

Some of the published data on these metals is relevant to infrared detection, such as DC conductivity, thermal conductivity, and temperature coefficient of

resistance. Other information must be measured at the wavelength of interest, including the frequency-dependent values for electrical conductivity and skin depth. To obtain values for these properties, I measured samples of the metals on a variable-angle infrared spectroscopic ellipsometer. The resulting data from the ellipsometer was used to calculate the real and imaginary parts of the refractive index for the metals, using curve-fitting software. The complex refractive index is defined in terms of frequency-dependent material properties:

$$n - jk = \sqrt{\varepsilon_r(\omega) - j\frac{\sigma(\omega)}{\omega\varepsilon_0}} \qquad 6.1$$

where n and k are the real and imaginary parts of the refractive index, εr is the relative permittivity, and σ is the conductivity. By squaring both sides of the equation and equating the real and imaginary parts, one can solve for the conductivity:

$$\sigma(\lambda) = \frac{4\pi c n k \varepsilon_0}{\lambda} \qquad 6.2$$

.

Skin depth can also be calculated from ellipsometric data. Defined as how deep into the material an electromagnetic wave is attenuated to e^{-1} (or 36.79%) of it's intensity at the boundary, skin depth, δ, is given by

$$\delta = \frac{\lambda}{4\pi k} \tag{6.3}$$

.

Figure 6-1 and Figure 6-2 show the electrical conductivity and skin depth for each metal across the 8 - 12 μm wavelength band, based on ellipsometric measurements. Table 6-1 shows the relevant information gathered for each metal from ellipsometric measurements or published data. IR electrical conductivity and skin depth values are given for 10.6 μm wavelength in the table, since this is the wavelength used for laser measurements. As one would expect, the measured electrical conductivity values are less than those for the same metal at DC. The materials exhibit greater loss as wavelength decreases.

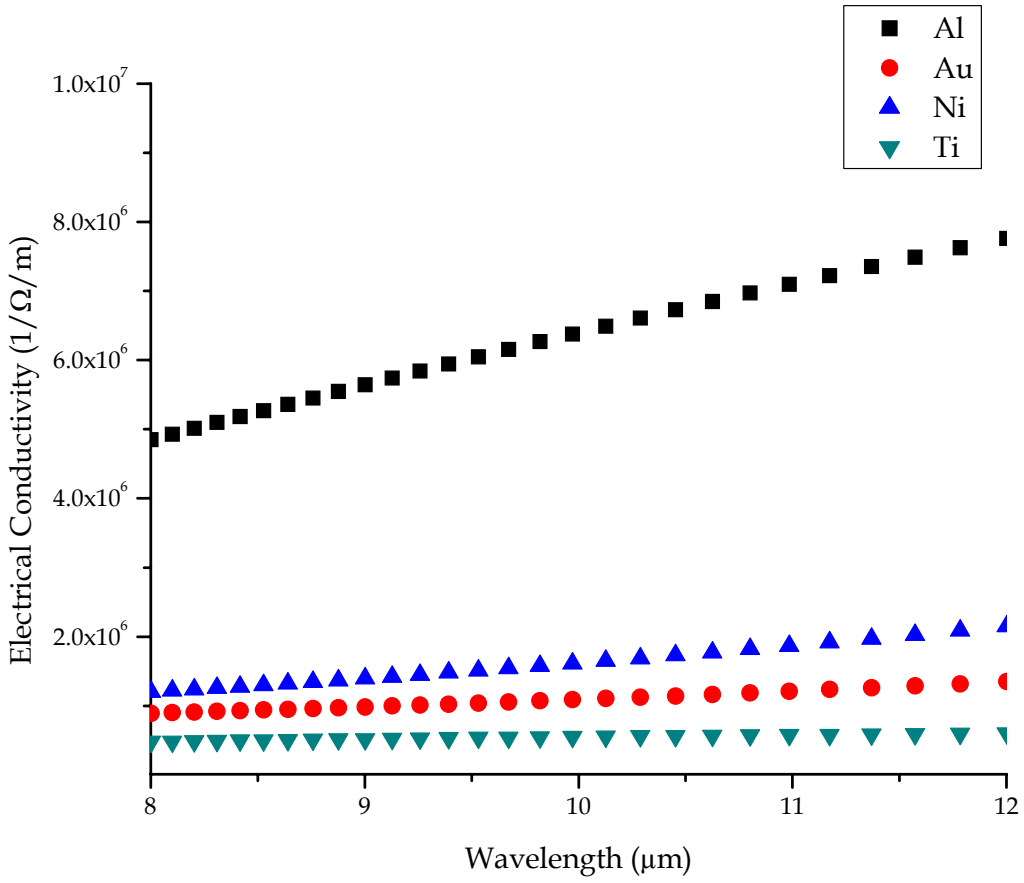

Figure 6-1: Electrical conductivity of antenna metals from 8 - 12 μm from ellipsometer measurements

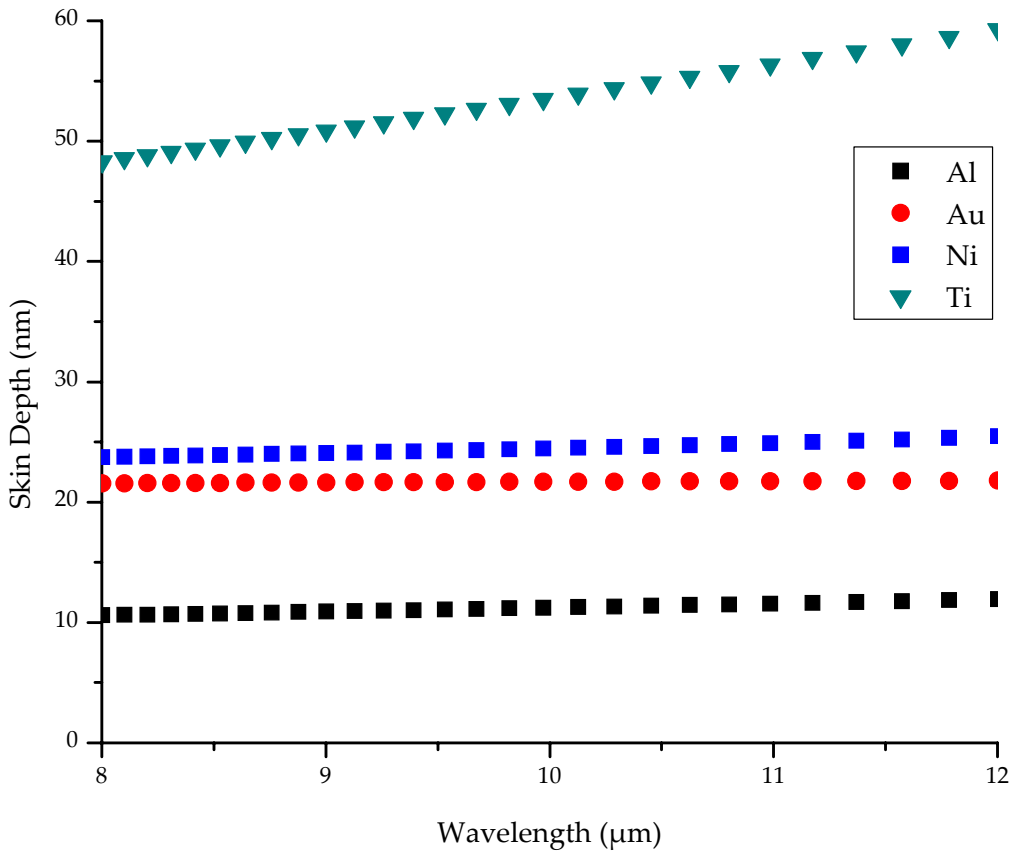

Figure 6-2: Skin depth of antenna metals from 8 - 12 μm from ellipsometer measurements

Table 6-1: Properties of metals for antenna metal study, including ellipsometrically measured conductivity and skin depth at 10.6 μm

Metal Property	Al	Au	Ni	Ti
Thermal conductivity (W/m/K)	235	320	91	22
TCR (10^{-3}/°C)	4	3.5	6	3.5
DC electrical conductivity (10^6/Ω/m)	37.7	45.5	14.3	2.3
IR electrical conductivity (10^6/Ω/m)	6.85	1.16	1.42	0.53
Skin Depth (nm)	11.5	21.7	24.1	51.6

6.1.2 Model Results

By applying the measured values of frequency-dependent conductivity to HFSS models of antennas, I was able to evaluate the metals with an electromagnetic model. To do this, I drew a 2-D square spiral antenna, placed it on a dielectric substrate (BCB, using measured optical constants in the model), and surrounded the substrate and antenna with an air box (see Figure 6-3). The antenna line width was 500 nm, the dielectric layer thickness was 1.72 μm, and the air box size

was 16 μm x 16 μm x 8 μm. At the feed of the antenna a 500 nm square was assigned as a 50 Ω lumped port. The top and sides of the air box were given a radiation boundary assignment, and the bottom of the air box was assigned the finite conductivity of gold, to simulate an actual gold ground plane.

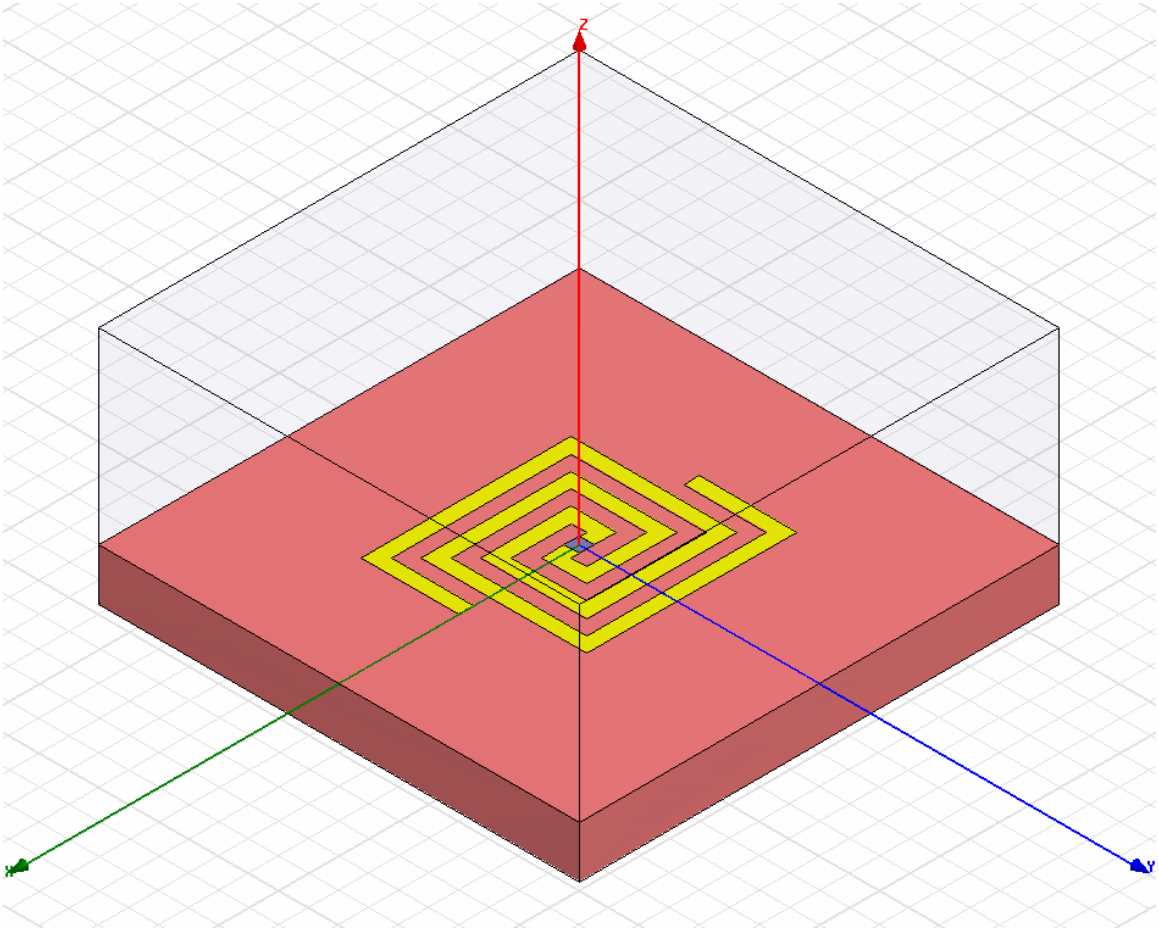

Figure 6-3: HFSS model drawing of a square spiral antenna on a dielectric substrate

For the analysis of the structure I set up a discrete frequency sweep from 8 - 12 μm (25 - 37.5 THz). After running sweeps for each metal, I plotted the antenna radiation efficiency as a function of frequency. The results are shown in Figure 6-4. It is important to keep in mind that the HFSS model doesn't account for thermal effects. The electromagnetic model shows that there is indeed a noticeable difference between the metals, but only experimental data can tell how much the response is affected by the thermal properties of the metals.

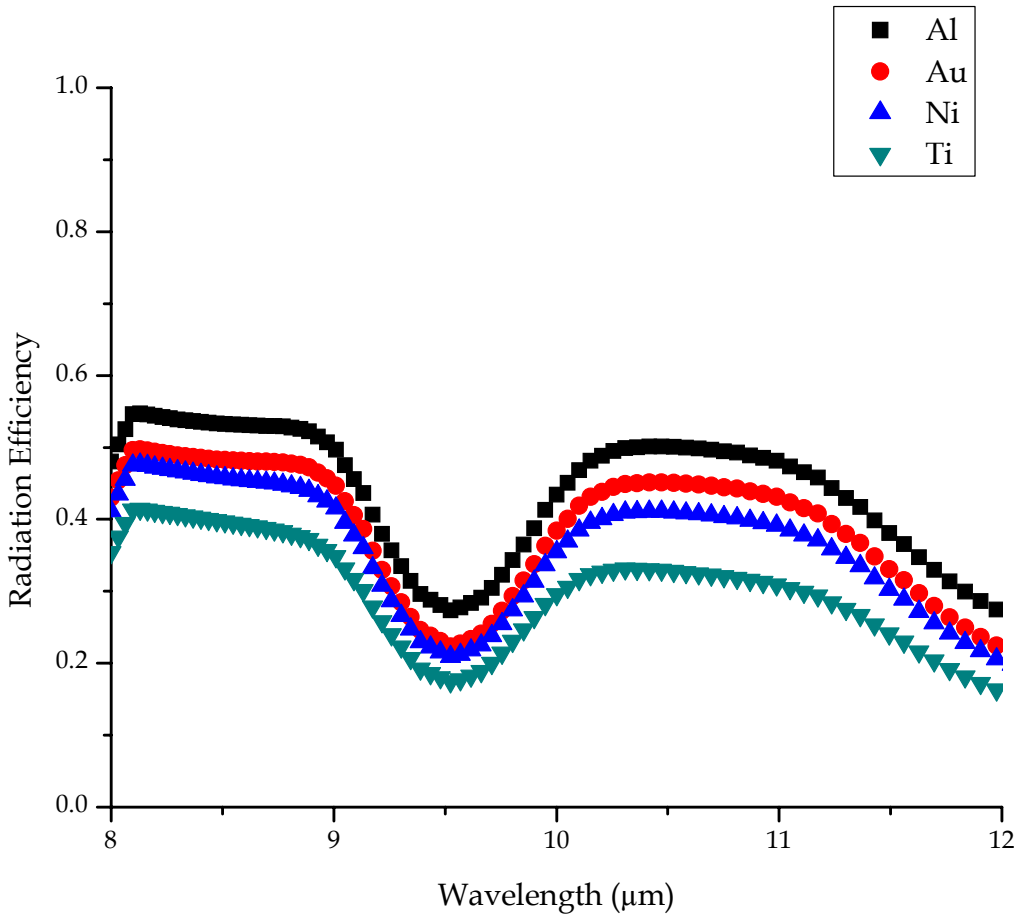

Figure 6-4: HFSS simulation results showing antenna radiation efficiency for different metals for a square spiral antenna on a BCB substrate with a gold ground plane

6.2 Ground Planes and Dielectric Standoff Layers

6.2.1 Dielectric Material for Standoff Layers

The addition of a ground plane beneath the detector increases device responsivity. The choice of dielectric material between the device and the ground plane affects the overall performance of the device. In previous experiments, devices were fabricated on SiO_2 because it was an easy material to work with. However it exhibits large absorption in the 8 - 12 μm wavelength region. Materials with lower loss could be used in place of SiO_2. Figure 6-5 shows the absorption coefficient of three dielectric materials as a function of wavelength: SiO_2, ZrO_2, and BCB. Ellipsometric measurements were used to obtain the optical constants of these dielectric materials, and the absorption coefficient was calculated using

$$\alpha = \frac{4\pi k}{\lambda} \qquad 6.4$$

ZrO_2 has much lower loss than SiO_2 in the 8 - 12 μm range, but it lacks the processing ease of SiO_2: deposition and etching present significant technical

challenges. BCB is a dry-etch resin commonly used as a low-loss spin-on dielectric layer in many electronic applications. It is comparable to ZrO_2 in terms of absorption loss, and is easy to deposit and etch, making it the best candidate material for this study.

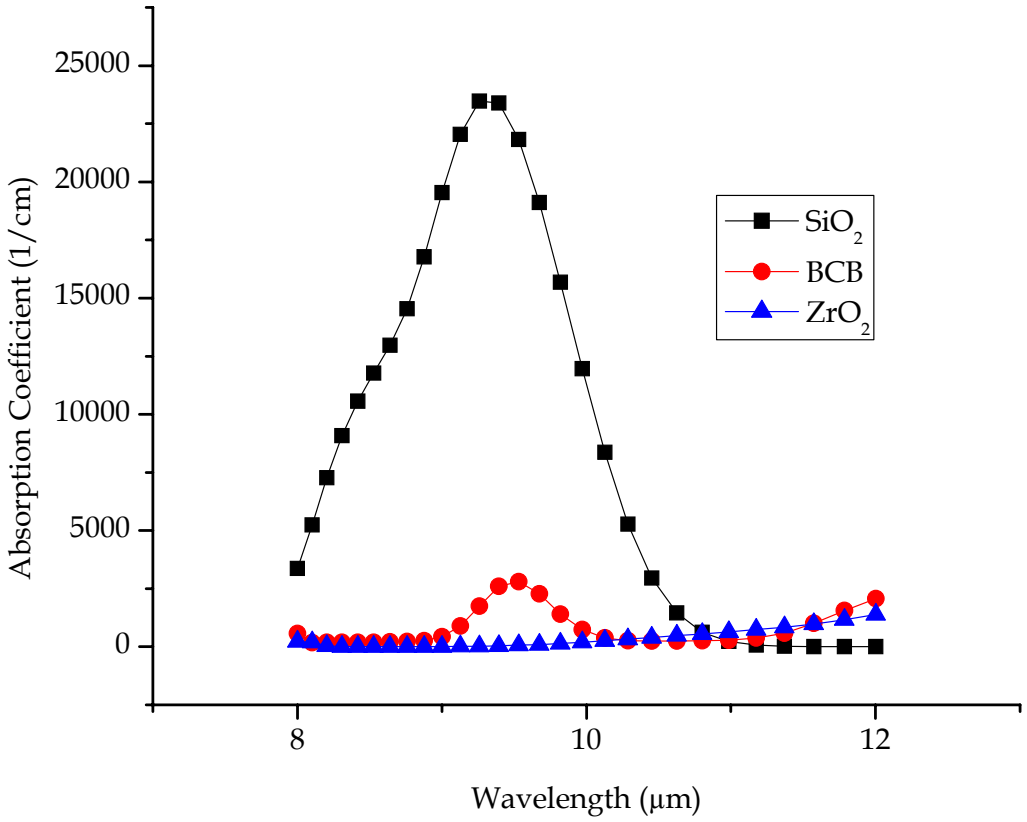

Figure 6-5: Absorption coefficient versus wavelength for SiO_2, BCB, and ZrO_2 from 8 - 12 μm

6.2.2 Dielectric Layer Thickness

6.2.2.1 Theoretical Considerations

The thickness of a dielectric layer over a ground plane should be chosen to enhance the effect of the ground plane and increase device response. The effect of a dielectric layer between a ground plane and an antenna has been investigated to determine the optimal length of a dipole antenna [37], and various numerical analyses have considered its influence on other antenna properties [6, 38-40]. From an optical perspective, consider a plane wave illuminating the device at normal incidence. As the wave propagates in the dielectric and is reflected by the ground plane, the incident and reflected waves interfere with each other. The condition for constructive interference is satisfied when the phase difference between the two waves is a multiple of 2 π. The effect of the dielectric layer on the phase (δ) of the reflected wave depends on the layer thickness:

$$\delta = \frac{2\pi}{\lambda}(OPD) \qquad 6.5$$

OPD is the optical path difference between the incident and reflected wave. The ground plane adds a phase shift of π to the reflected wave, and a dielectric layer thickness of $\frac{\lambda}{4n}$ would give a phase shift of $\pi/2$ each time the wave passes through the layer. The accumulated phase is then 2 π, which would result in constructive interference of the waves.

The dielectric layer thickness problem can also be considered by applying image theory. The combination of the antenna and its image preserve boundary conditions at the ground plane, and by the uniqueness theorem, form an equivalent system whose solution is valid in the half-space containing the original antenna. This is shown in Figure 6-6.

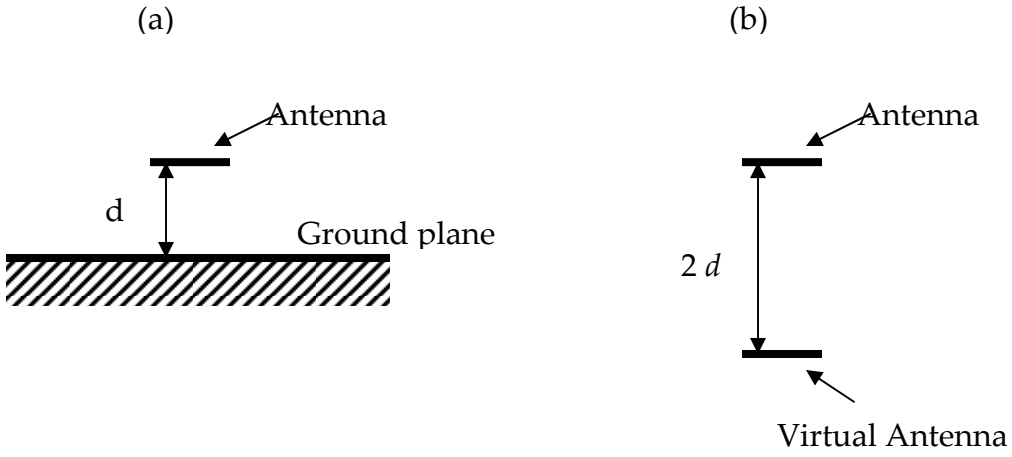

Figure 6-6: Image theory applied to an antenna above a ground plane. (a) An antenna a distance *d* away from a flat reflector can be represented as (b) two antennas with a spacing of 2 *d*.

Using this image approach, Balanis [30] developed an expression for the electric field of an infinitesimal dipole antenna positioned horizontally above a ground plane for far-field observations:

$$E_{\psi} = j\eta \frac{k I_0 l e^{-jkr}}{4\pi r} \sqrt{1-\sin^2\theta \sin^2\phi}\,\left[2j\sin(k d\cos\theta)\right] \qquad 6.6$$

Here k is the wave number, r is the distance from the antenna to the point of observation, I_0 is the antenna current (assumed constant for an infinitesimal dipole), l is the length of the dipole ($l \ll \lambda$ for an infinitesimal dipole), the angles θ and ϕ describe the direction of the point of observation (in this case it is directly above the antenna, so $\theta = 0$), and d is the dielectric layer thickness. The variation of the electric field with different standoff heights is then sinusoidal, and the normalized magnitude of the electric field is simply:

$$\overline{E}_{\psi} = \left| \sin\left(\frac{2\pi d}{\lambda} \right) \right| \qquad 6.7$$

The normalized magnitude of the electric field is plotted as a function of antenna standoff height over one wavelength in Figure 6-7. Again, one expects maxima to occur at standoff heights with are odd multiples of $\lambda/4$.

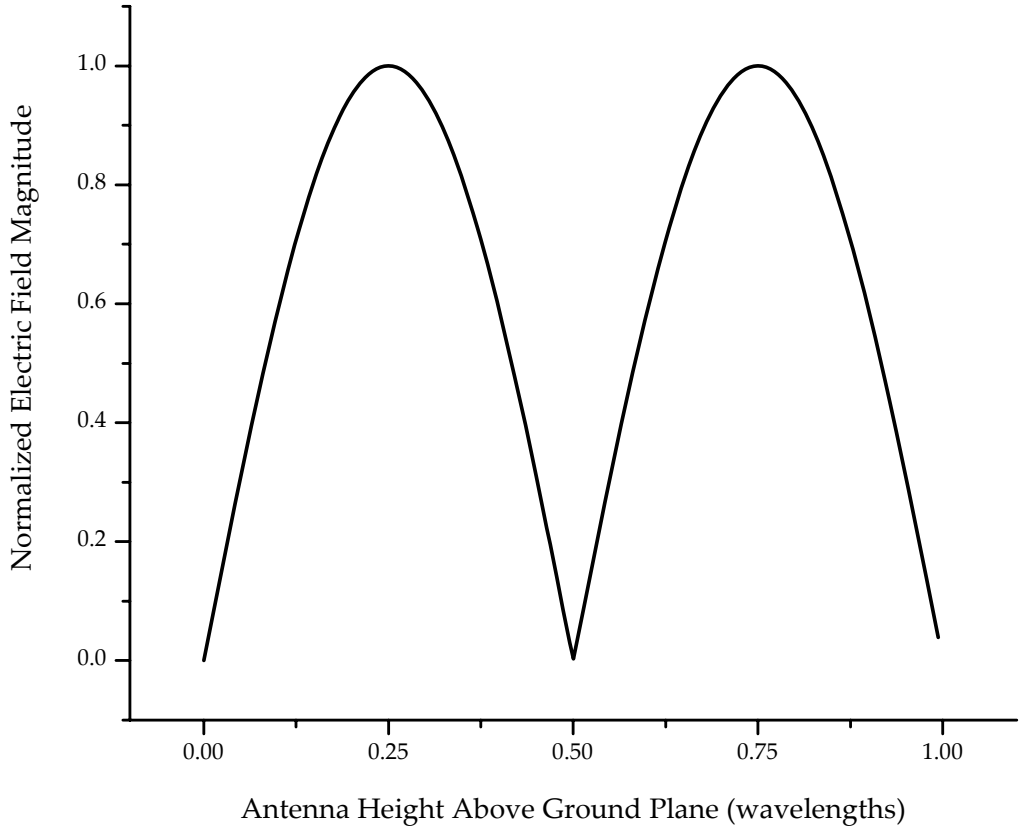

Figure 6-7: Normalized electric field magnitude vs. height above ground plane for an ideal dipole antenna above an infinite, lossless ground plane

Another important consideration in the evaluation of dielectric layer thickness is the propagation of surface waves. As surface wave modes are excited in the substrate, power is lost from the antenna and device responsivity decreases. The

number of surface-wave modes that will propagate on the dielectric layer depends on the permittivity and thickness of the dielectric, and is given by [41]:

$$f_c = \frac{c\,n}{4\,d\,\sqrt{\varepsilon_r - 1}} \qquad 6.8$$

Here the cutoff frequency for a given mode (n = 0, 2, 4, ... for TM modes; n = 1, 3, 5, ... for TE modes) is inversely proportional to the dielectric layer thickness, d, and to the square root of the dielectric layer relative permittivity, ε_r. The TM_0 mode is always present, as it has zero cutoff frequency. Figure 6-8 shows the surface-wave modes that are introduced above a given thickness for BCB at 10.6 μm. For a layer thickness less than 2.27 μm, only the TM_0 mode will propagate. A BCB layer thickness of $\lambda/4n$ (1.72 μm) would therefore allow only one surface wave mode to propagate, while a layer thickness of $3\lambda/4n$ (5.17 μm) would allow the TE_1 and TM_2 modes to propagate as well.

The amount of power coupled to surface modes depends on the number of modes propagating, and on the difference between the cutoff frequency and the actual frequency for a given mode. For example, if the TM_0 mode is the only

surface wave mode present, more power will be coupled to that mode if the layer is 2 μm thick than if it is 100 nm thick.

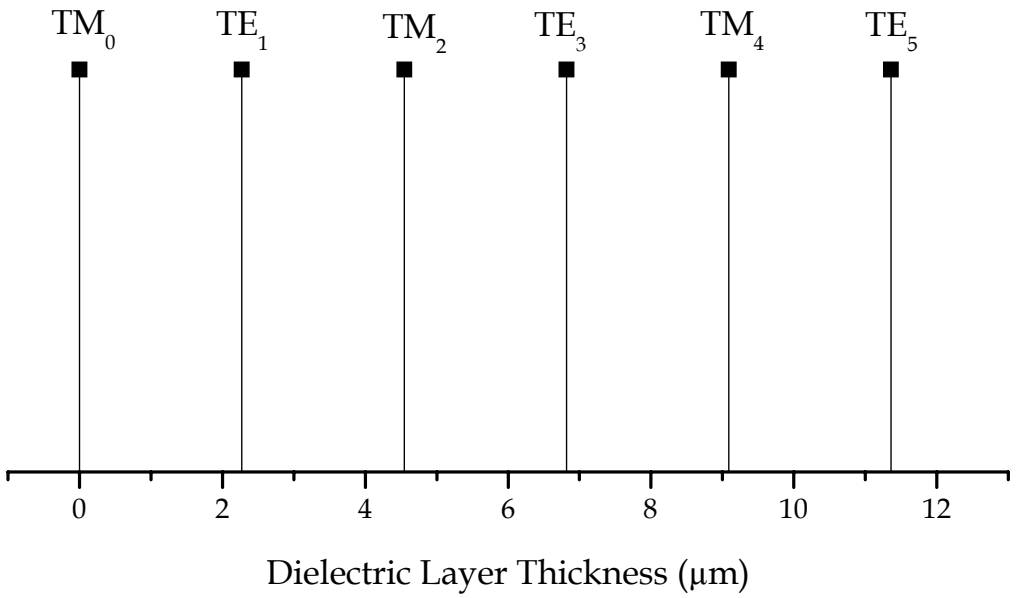

Figure 6-8: Surface-wave modes excited for a given dielectric layer thickness, using 10.6 μm for cutoff frequency and BCB for the dielectric material (ε_r = 2.36)

6.2.2.2 Model Results

By applying the measured values of optical constants for dielectric materials and metals to HFSS models of antennas on substrates, I was able to evaluate the effect of dielectric thickness on the antenna. To do this, I drew a 2-D square spiral antenna, placed it on the dielectric substrate and surrounded the substrate and antenna with an air box (as in Figure 6-3). The antenna line width was 500 nm, and the air box size was 16 μm x 16 μm x 16 μm. At the feed of the antenna, a 500 nm square was assigned as a 50 Ω lumped port. The top and sides of the air box were given a radiation boundary assignment, and the bottom of the air box was assigned the ellipsometrically-determined finite conductivity of gold, to simulate an actual gold ground plane.

HFSS was used to model the effect of dielectric material thickness on the electric field of the square spiral antenna by sweeping the dielectric layer thickness over one wavelength and keeping the frequency at 28.3 THz (~10.6 μm), as shown in Figure 6-9. For the simulations, both BCB and air were used for the dielectric material between the antenna and the ground plane. The calculated electric field

for an infinitesimal dipole, shown in Figure 6-7, is included in Figure 6-9 for comparison to the simulated square spiral antenna results.

The simulations follow the ideal case fairly well, and differences can be attributed to the finite conductivity of the antenna metal, the use of square spiral antennas instead of dipoles, and in the case of the BCB model, losses in the dielectric material. The BCB model also has a maximum at $3\lambda/4n$ that is greater than the maximum at $\lambda/4n$. Given the added loss due to a greater dielectric layer thickness and the addition of two surface wave modes, this seems incorrect; one would expect the field to be strongest at $\lambda/4n$. But since BCB was chosen because it has very low dielectric losses, the dielectric layer thickness may not cause the field to attenuate much from the added propagation distance in the material. Surface wave effects are included in the field solutions to the HFSS model. The trend in the curves of Figure 6-9 suggests that their effect on the antenna is perhaps significant.

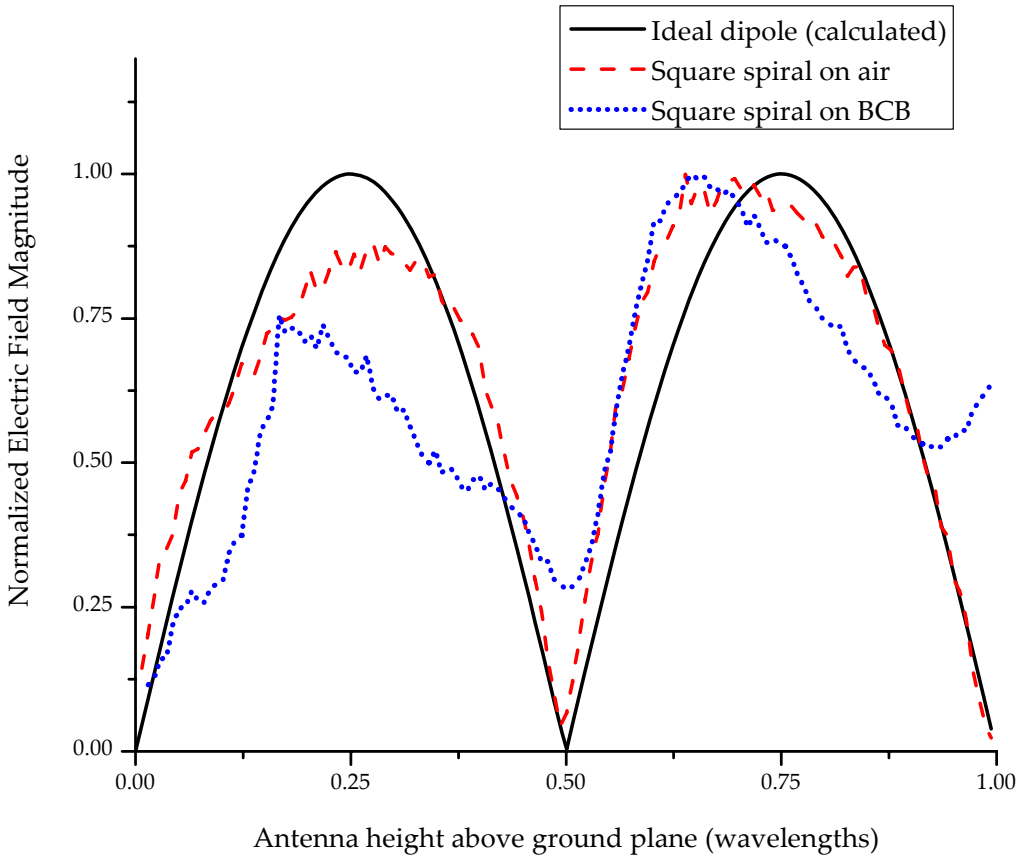

Figure 6-9: Simulation results from HFSS model of a square spiral antenna on a dielectric layer of BCB or air above a gold ground plane, varying the standoff height of the antenna. Normalized electric field magnitude is shown for each case, along with the calculated value for an infinitesimal dipole from Figure 6-7 for comparison.

6.3 Toward Via Connections

To further optimize the performance of antenna-coupled infrared detectors, via connections can be used to remove the effect of lead lines on antenna performance. Figure 6-10 shows a graphical representation of a micro-bolometer coupled to a dipole antenna on a dielectric standoff layer above a ground plane. Lead lines run from the bolometer to bond pads for signal read-out and biasing of the bolometer. These lead lines are in the same plane as the antenna-coupled device and will affect antenna performance.

Figure 6-11 shows a graphical representation of the same device using via connections instead of planar lead lines. Here the bias voltage and signal read-out runs from the bolometer straight down, through a small opening in the ground plane, and then underneath the ground plane and out to bond pads elsewhere on the wafer. This should eliminate the effect of the lead lines and allow better characterization of antenna properties.

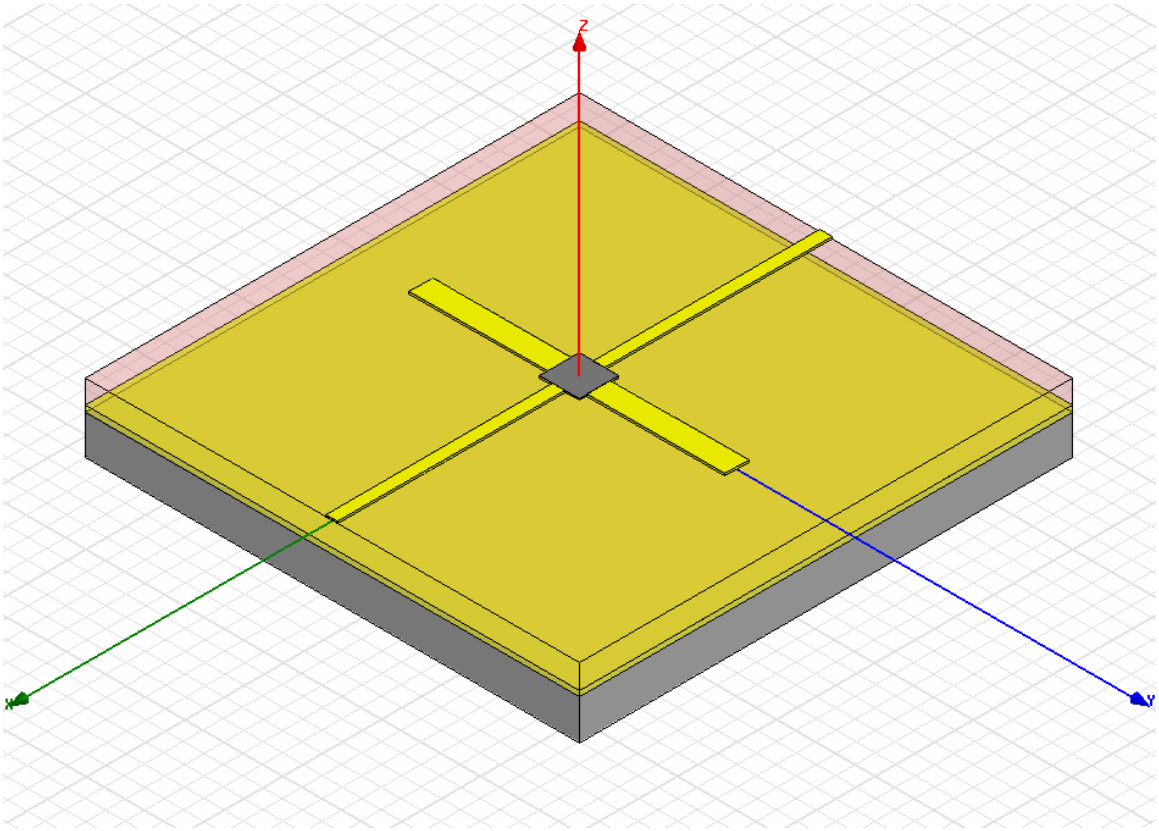

Figure 6-10: Graphical representation of antenna-coupled detector with lead lines in the same plane as the detector

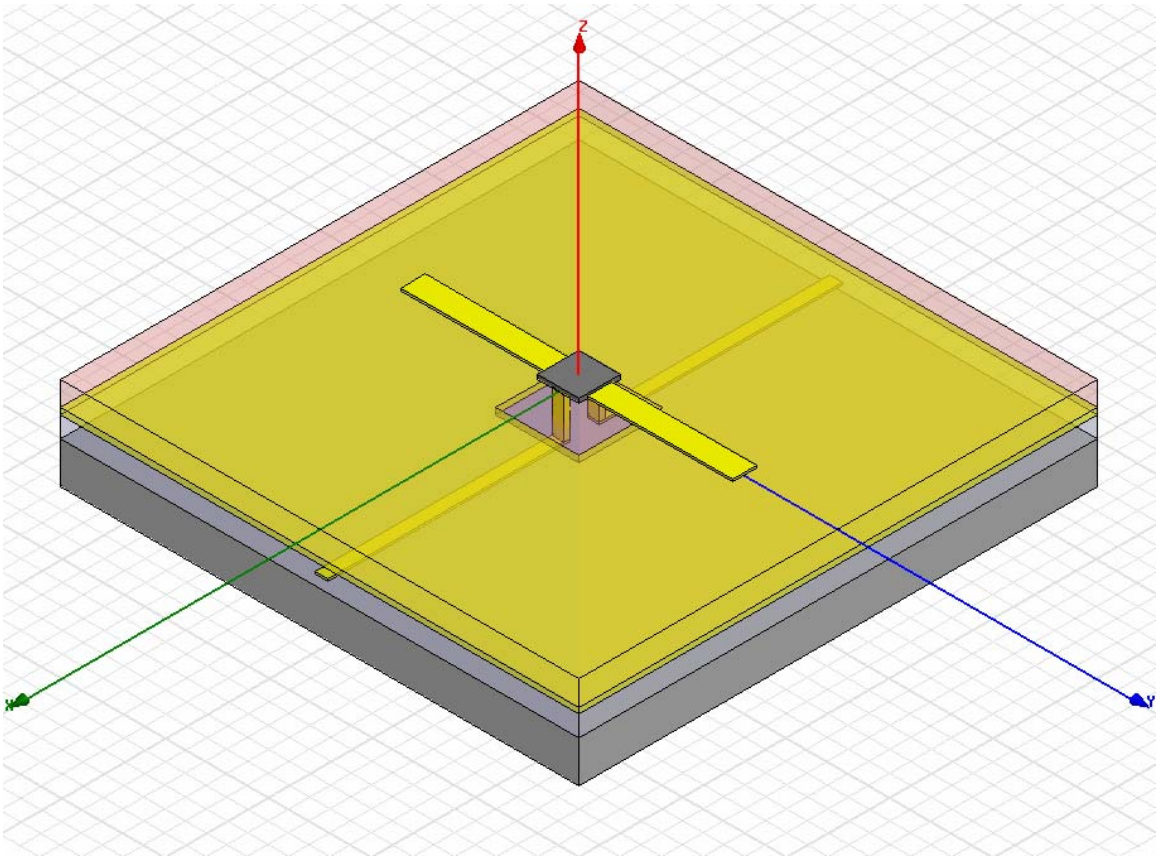

Figure 6-11: Graphical representation of an antenna-coupled detector with via connections instead of lead lines

Fabricating such a structure requires process techniques that are commonly used for other applications but have not been applied to infrared antenna-coupled detectors. The following fabrication process might be successfully developed with only a few steps that require characterization:

1. Coat Si wafer with an arbitrarily thick layer of BCB (for electrical insulation).
2. Lithographically define the bond pads and lead lines for the device, as well as one set of alignment marks for ground plane alignment. Use e-beam evaporated Ti-Au, 100 nm thick.
3. Coat wafer with a thin layer of BCB (~200 nm): thick enough to insulate the lead lines from the ground plane, but thin enough to keep the required etch depth as shallow as possible.
4. Lithographically define the ground plane, with a small opening for the via-connected lead lines and two sets of negative alignment marks. Use e-beam evaporated Ti-Au-Ti for ground plane metal, with the top layer of Ti for adhesion of the next BCB layer.
5. Coat wafer with a layer of BCB, using thickness chosen based on considerations in section 6.2 above.
6. Use e-beam lithography to define an etch mask in ZEP 520A resist for RIE etching of via connections in BCB. Ensure that via holes are smaller than the opening in the ground plane to avoid shorting the lead lines on the ground plane.
7. Apply RIE process to etch via holes in BCB.

8. Fill via holes through an electroplating process. This step requires characterization of a new process. It should be possible to electroplate Au in the holes etched in the preceding step. A possible alternative to electroplating is the use of Au nanoparticles to fill the holes. The ~10 nm-diameter particles may then be fused into a continuous connection by exposure to an electron beam, since the ratio of surface area to volume greatly reduces the melting point of the Au particles.
9. Lithographically define antenna-coupled device, using negative alignment marks in the ground plane to align the device to the via connections. Instead of using negative alignment marks, one could use a smaller ground plane and place positive alignment marks farther away from the device. The larger the ground plane, the more it will approximate an infinite ground plane; but a square millimeter would be sufficiently large for a typical infrared device.

Etching high aspect ratio holes in BCB may prove difficult and require thicker resist layers for etch masks. Etch diameters of 200 nm will be small enough that a standard bolometer size (~500 nm squares) will mask the via connections. The process step involving electroplating will present some initial technical challenges. Neither evaporation nor sputtering will work in this step if the via

aspect ratio is much greater than 2:1. Both of these processes are too directional, the opening would be closed off before it could be filled. For 200-nm diameter holes and a dielectric layer thickness of 1.7 μm, some kind of plating process will be the best solution.

CHAPTER 7

CONCLUSION

7.1 Development of Fabrication Processes

Fabrication processes relied heavily on e-beam lithography, e-beam evaporation, and lift-off. I have developed processes for a variety of e-beam resist combinations and have given details on each process, including directions for resist deposition, spin speeds and baking instructions; de-scum etch rates; BCB processing details for dielectric standoff layers; important details for thin film deposition of Au, Ti, Cr, Ni, Al, Bi, SiO, and SiO_2; and information on various wet and dry etch processes. The devices in this work were all fabricated according to these instructions.

A brief explanation of the measurement setups is also given. Infrared spectral and blackbody measurement and millimeter-wave measurement setups are shown, along with an explanation of the figures of merit for each type of measurement, and how to obtain this figure from the measured data.

7.2 Millimeter-Wave Detectors

Two kinds of detector were fabricated: a bolometer on a slot antenna, and a Schottky diode with a patch antenna. The slot antenna was used to measure the attenuation of 94-GHz radiation of several materials. Responsivity and noise were also measured, using the test setup in Figure 3-3. From these measurements, and with the bandwidth of the antenna as determined through HFSS simulations, NETD was calculated to be 206 K.

The SiC Schottky diode was fabricated and measured for polarization response and frequency mixing. I-V curve measurements were also made. The device was found to function as a mixer, and the patch antenna showed the appropriate polarization response.

Improvements to both devices were investigated first from an analysis of the antenna's behavior. HFSS simulations showed the advantages of other antenna designs, and the effect of impedance mismatches with the detector. The

performance of the Schottky diode was then investigated, with the goal of increasing the device cutoff frequency above 30 THz for infrared rectification.

7.3 Thermal Isolation of Infrared Devices

The inverse proportionality of thermal conductance to responsivity for infrared antenna-coupled bolometers led to efforts to thermally isolate the devices. Two methods were used: fabrication of a device on a membrane of Si_3N_4, and complete isolation of the device from the substrate through an air bridge. Fabrication processes for both devices are given. Measurements were made for the membrane devices, which were shown to have much greater sensitivity than devices on a substrate without a membrane. When operated under vacuum, the membrane devices had 163 times greater responsivity than the same device without a membrane.

7.4 Optimization of Infrared Devices

Ellipsometry was used to obtain the optical constants for several materials in the LWIR spectral region. From these constants, electrical conductivity was calculated for antenna metals, and optical absorption was found for dielectric materials. The performance of the device is influenced by these material properties, and HFSS simulations show their effect. Since the HFSS model doesn't include thermal effects, the choice of metal cannot be based entirely on the simulation results. Experimental data is needed. The dielectric material choice is simpler, and BCB was found to be the best choice, combining low absorption loss with ease of processing.

The optimal height of the antenna above a ground plane is considered. Calculated and simulated results are fairly consistent, showing that odd multiples of a quarter-wave thickness should have the best response, despite surface wave propagation.

A possible fabrication process is presented for the construction of via connections through a ground plane. With BCB as the dielectric layer, RIE etching and electroplating could be used to create vias of 300-nm diameter through several microns of material. This will remove the effect of bias lines and bond pads on the performance of the device, improving antenna polarization and radiation pattern measurements.

LIST OF REFERENCES

[1] P. L. Richards, "Bolometers for Infrared and Millimeter Waves," *Journal of Applied Physics*, vol. 76, pp. 1-24, 1994.

[2] S. P. Langley, "The Bolometer and Radiant Energy," in *Proceedings of the American Academy of Arts and Sciences*, vol. XVI, 1881, pp. 342.

[3] G. H. Rieke and K. Visnovsky, *Detection of light : from the ultraviolet to the submillimeter*. Cambridge ; New York: Cambridge University Press, 1994.

[4] M. Henini and M. Razeghi, *Handbook of infrared technologies*. Oxford ; New York: Elsevier, 2002.

[5] F. J. Gonzalez, "Antenna-coupled infrared focal plane array," in *College of Engineering*: University of Central Florida, 2003, pp. xii, 170 leaves, bound.

[6] J. D. Kraus and R. J. Marhefka, *Antennas for all applications*, 3rd ed. New York: McGraw-Hill, 2002.

[7] C. Fumeaux, W. Herrmann, F. K. Kneubuhl, and H. Rothuizen, "Nanometer thin-film Ni-NiO-Ni diodes for detection and mixing of 30 THz radiation," *Infrared Physics & Technology*, vol. 39, pp. 123-183, 1998.

[8] E. N. Grossman, J. E. Sauvageau, and D. G. Mcdonald, "Lithographic Spiral Antennas at Short Wavelengths," *Applied Physics Letters*, vol. 59, pp. 3225-3227, 1991.

[9] K. Mizuno, Y. Daiku, and S. Ono, "Design of Printed Resonant Antennas for Monolithic-Diode Detectors," *Ieee Transactions on Microwave Theory and Techniques*, vol. 25, pp. 470-472, 1977.

[10] G. M. Rebeiz, "Millimeter-Wave and Terahertz Integrated-Circuit Antennas," *Proceedings of the Ieee*, vol. 80, pp. 1748-1770, 1992.

[11] F. J. Gonzalez and G. D. Boreman, "Comparison of dipole, bowtie, spiral and log-periodic IR antennas," *Infrared Physics & Technology*, vol. 46, pp. 418-428, 2005.

[12] J. Alda, C. Fumeaux, I. Codreanu, J. A. Schaefer, and G. D. Boreman, "Deconvolution method for two-dimensional spatial-response mapping of lithographic infrared antennas," *Applied Optics*, vol. 38, pp. 3993-4000, 1999.

[13] E. L. Dereniak and G. D. Boreman, *Infrared detectors and systems*. New York: Wiley, 1996.

[14] R. A. Smith, F. E. Jones, and R. P. Chasmar, *The detection and measurement of infra-red radiation*, 2nd ed. Oxford,: Clarendon, 1968.

[15] G. R. Brewer and J. P. Ballantyne, *Electron-beam technology in microelectronic fabrication*. New York: Academic Press, 1980.

[16] Y. Nishi and R. Doering, *Handbook of semiconductor manufacturing technology*. New York: Marcel Dekker, 2000.

[17] K. A. Valiev, *The physics of submicron lithography*. New York: Plenum Press, 1992.

[18] Microchem, "Nano PMMA and Copolymer Resists," in *http://www.microchem.com/products/pdf/PMMA_Data_Sheet.pdf*. Newton, MA: Microchem Corp., 2001.

[19] Zeon Corporation, "ZEP520A Technical Report," in *http://www.zeon.co.jp/*: ZEON Corp. Specialty Materials Division, 2003.

[20] Microchem, "Nano PMGI Resists," in *http://www.microchem.com/products/pdf/pmgi_resist.pdf*. Newton, MA: Microchem Corp., 2002.

[21] M. E. Mills, P. Townsend, D. Castillo, S. Martin, and A. Achen, "Benzocyclobutene (DVS-BCB) polymer as an interlayer dielectric (ILD) material," *Microelectronic Engineering*, vol. 33, pp. 327-334, 1997.

[22] Dow Chemical, "CYCLOTENE™ 3000 Series Advanced Electronic Resins," in *http://www.dow.com/cyclotene/resource/prodlit.htm*: The Dow Chemical Company, 2005.

[23] M. R. Abdel Rahman, "Antenna-coupled tunnel diodes for dual-band millimeter-wave/infrared focal-plane arrays." Orlando, Fla.: University of Central Florida, 2004.

[24] D. A. Glocker and S. I. Shah, *Handbook of thin film process technology*. Bristol, UK ; Philadelphia: Institute of Physics, 1998.

[25] M. Ohring, *The materials science of thin films : deposition and structure*, 2nd ed. San Diego, CA: Academic Press, 2002.

[26] K. Seshan, *Handbook of thin-film deposition processes and techniques : principles, methods, equipment and applications*, 2nd ed. Norwich, N.Y.: Noyes Publications/William Andrew, 2002.

[27] M. R. Baklanov, S. Vanhaelemeersch, H. Bender, and K. Maex, "Effects of oxygen and fluorine on the dry etch characteristics of organic low-kappa dielectrics," *Journal of Vacuum Science & Technology B*, vol. 17, pp. 372-379, 1999.

[28] C. F. Middleton, G. Zummo, A. Weeks, A. Pergande, L. Mirth, and G. D. Boreman, "Passive millimeter-wave focal plane array," presented at Radar Sensor Technology and Passive Millimeter-wave Imaging Technology VII SPIE Defense and Security Symposium, Orlando, FL, 2004.

[29] I. A. Salama, "Laser doping and metallization of wide bandgap materials : SiC, GaN and AlN," in *College of Engineering.*, vol. PhD. Orlando: University of Central Florida. , 2003, pp. xxvi, 254 leaves, bound.

[30] C. A. Balanis, *Antenna theory : analysis and design*, 2nd ed. New York: Wiley, 1997.

[31] H. C. Torrey, C. A. Whitmer, and S. Goudsmit, *Crystal rectifiers*, 1st ed. New York,: McGraw-Hill Book, 1948.

[32] S. M. Sze, *Physics of semiconductor devices*, 2nd ed. New York: Wiley, 1981.

[33] P. W. Kruse and D. D. Skatrud, *Uncooled infrared imaging arrays and systems*. San Diego: Academic Press, 1997.

[34] C. F. Middleton and G. D. Boreman, "Technique for thermal isolation of antenna-coupled infrared micro-bolometers," *Journal of Vacuum Science & Technology B*, 2006.

[35] F. J. Gonzalez, B. Ilic, and G. D. Boreman, "Antenna-coupled microbolometers on a silicon-nitride membrane," *Microwave and Optical Technology Letters*, vol. 47, pp. 546-548, 2005.

[36] R. C. Reid, J. M. Prausnitz, and B. E. Poling, *The properties of gases and liquids*, 4th ed. New York: McGraw-Hill, 1987.

[37] L. Codreanu and G. D. Boreman, "Influence of dielectric substrate on the responsivity of microstrip dipole-antenna-coupled infrared microbolometers," *Applied Optics*, vol. 41, pp. 1835-1840, 2002.

[38] P. B. Katehi and N. G. Alexopoulos, "On the Effect of Substrate Thickness and Permittivity on Printed-Circuit Dipole Properties," *Ieee Transactions on Antennas and Propagation*, vol. 31, pp. 34-39, 1983.

[39] H. Nakano, M. Ikeda, K. Hitosugi, and J. Yamauchi, "A spiral antenna sandwiched by dielectric layers," *Ieee Transactions on Antennas and Propagation*, vol. 52, pp. 1417-1423, 2004.

[40] H. Nakano, K. Nogami, S. Arai, H. Mimaki, and J. Yamauchi, "A Spiral Antenna Backed by a Conducting Plane Reflector," *Ieee Transactions on Antennas and Propagation*, vol. 34, pp. 791-796, 1986.

[41] P. Bhartia, K. V. S. Rao, and R. S. Tomar, *Millimeter-wave microstrip and printed circuit antennas*. Boston, MA: Artech House, 1991.